THE SCATTERING OF ELECTRONS BY POLYCRYSTALLINE METAL FILMS, WITH SPECIAL REFERENCE TO THE USE OF HIGH ENERGY TRANSMISSION ELECTRON DIFFRACTION FOR PROPORTIONAL ANALYSIS.

Radhi Assad Ali AL-MAUSAWE

A thesis submitted for the degree of

DOCTOR OF PHILOSOPHY

in

The University of Aston in Birmingham

February 1983

Department of Physics.

"The University of Aston in Birmingham"

THE SCATTERING OF ELECTRONS BY POLYCRYSTALLINE METAL FILMS, WITH SPECIAL REFERENCE TO THE USE OF HIGH ENERGY TRANSMISSION ELECTRON DIFFRACTION FOR PROPORTIONAL ANALYSIS.

A thesis submitted for the degree of

DOCTOR OF PHILOSOPHY

by

Radhi Assad Ali AL-MAUSAWE

1983

SUMMARY

Experiments have been performed to study the variation of the relative integrated intensities of transmission electron diffraction patterns of polycrystalline specimens. The effect of film thickness, accelerating voltage, crystallite size, atomic number of the material and amorphous content are discussed.

Selected area electron diffraction patterns, from vacuum-evaporated thin films of α-iron, copper, aluminium and silver, on carbon-coated grids for single and composite specimens, were obtained by using an electron microscope with high accelerating voltages (100 to 1000kV). The variation of diffraction contrast with the ratio (t/λ_T) of aluminium, α-iron and silver have been measured and the results were compared with those obtained from unsupported aluminium specimens to confirm the effect of the proportion of amorphous content.

Experimental measurements of the relative integrated intensity ratios of selected pairs of maxima from single specimens showed that there is a transition from dynamical to kinematical intensities as the average Bragg angle $\bar{\theta}$ went higher and the results were in a good agreement with the theoretical estimation (see Equation 2.19) of the validity of the dynamic and kinematic theories.

For composite specimens, it was shown that the qualitative form of Equation 2.23 is correct. But little success was observed in deducing the thickness ratio of the two laminae from their relative integrated intensity ratio. It seems probable that, different scattering processes might be involved in the two laminae composite specimen.

The contrast of electron diffraction patterns from single specimens of aluminium and α-iron showed a decrease with the ratio of thickness (t) to total scattering mean free path (λ_T) for (t/λ_T) less than unity, which was shown to be due to the proportion of amorphous content to the scattering of the electrons. This effect is less pronounced for heavy materials, as shown by the constant contrast for values of (t/λ_T) less than unity for the silver specimens.

Key Words.
Electron, Scattering, Diffraction, Proportional Analysis.

DEDICATED TO MY WIFE, LAMIA

AND MY DAUGHTERS, ZENA AND REHAM.

CONTENTS

LIST OF SYMBOLS

SI units are used throughout, except where otherwise stated.

c speed of light.

C Electron diffraction contrast.

C' Peak contrast.

C_p Peak contrast in plural scattering conditions.

C_s Peak contrast in single scattering conditions.

d Interplanar spacing of the atomic planes.

e Electronic charge.

e^{-D} Debye-Waller factor.

$f_e(\theta)$ Atomic scattering factor for electron.

$F_e(\theta)$ Structure factor for electron.

F : $F = \dfrac{F_e(\theta)_1 . e^{-D}1 . v_2}{F_e(\theta)_2 . e^{-D}2 . v_1}$, where the subscripts 1 and 2 stand for the materials 1 and 2 of the composite specimen.

G : $G = \dfrac{I_1/I_2}{t_1/t_2} \cdot \dfrac{d_2^2 P_2}{d_1^2 P_1}$

h Plank's constant.

I_o Incident intensity.

I_{hkl} Diffracted intensity of the (hkl) diffraction ring.

I_T Transmitted intensity.

J : $J = \dfrac{I_{h_1k_1l_1}}{I_{hkl}} \cdot \dfrac{d_{hkl}^2 \cdot P_{hkl}}{d_{h_1k_1l_1}^2 \cdot P_{h_1k_1l_1}}$, where $(h_1k_1l_1)$ is the strongest diffraction ring in single lamina specimen.

$k(\theta)$ Fraction of electrons diffracted per unit specimen thickness per unit solid angle into the peak of the diffraction ring.

k' Proportion of amorphous material.

K Total number of electrons scattered through all angles by all processes.

ℓ Slit length.

L Camera length.

m Mass of the moving electron.

m_o Rest mass of the electron.

M_a Atomic mass of the material.

n : $n = \frac{\log J}{\log Q}$ in single specimen or $n = \frac{\log G}{\log F}$ in composite specimen.

n' Fringes order in the multiple beam interferometer.

P Multiplicity factor.

Q : $Q = \frac{[F_e(\theta).e^{-D}]_{h_1 k_1 l_1}}{[F_e(\theta).e^{-D}]_{hkl}}$ for single lamina specimen.

R Radius of the diffraction ring.

t Specimen thickness.

T Temperature.

u Electron velocity.

v Volume of the unit cell.

V Accelerating voltage.

w Width of the peak at the half peak point.

W Width of the background under the peak.

ϵ Crystallite size.

θ Bragg angle.

$\bar{\theta}$ Average Bragg angles.

Θ Characteristic temperature.

	Electron wavelength.
λ_e	Elastic mean free path for electron.
λ_i	Inelastic mean free path for electron.
λ_T	Total mean free path for electron.
λ_p	The smaller mean free path of elastic and inelastic.
ρ	Density of the material.
σ_e	Elastic cross section for electron.
σ_i	Inelastic cross section for electron.
$\mathcal{E}_p$	Exposure dose to the peak.
$\mathcal{E}_B$	Exposure dose to the background.

LIST OF FIGURES.

LIST OF TABLES.

ACKNOWLEDGEMENTS.

I wish to express my sincere gratitude to my supervisor, Dr.T.F.J.Quinn, for his advice and supervision throughout my research.

I am indebted to Professor T.Mulvey from the Physics Department, University of Aston, for his co-operation and guidance during my supervisor sabatical leave.

Many thanks to Mr.R.Keen for his considerable technical assistance to whom I will always be indebted.

Last but not least I would like to thank the Department of Material Science, Birmingham University, for the use of their High Voltage Electron Microscope.

CHAPTER ONE

INTRODUCTION.

1.1 Electron scattering.

If a beam of electrons is incident upon a solid target, the electrons are either undeviated or scattered. In the transmission electron microscope the specimen target is sufficiently thin, so that a significant fraction of the beam is transmitted. In this technique, information is obtained from, both the undeviated and the scattered, transmitted electrons. If the specimen is crystalline we find that several strong and well-defined beams of electrons are transmitted from the bombarded area. These beams of electrons are analogous to diffracted light rays or x-ray beams diffracted from crystals. If the electrons are regarded as particles, attempts to account for the strong diffracted beams results in complete failure. However, if one assumes the wave description of electrons, as proposed by de Broglie (1), one obtains a satisfactory explanation of the motion of electrons in solid crystalline bodies and the processes of electron diffraction. The wave fronts of an electron beam are normal to the direction of propagation and de Broglie (1) postulated that the wavelength of the associated wave is given by:-

$$\lambda = \frac{h}{mu} \qquad 1.1$$

where h is Plank's constant, m the mass of the moving

electron, and u its velocity.

The simple equation for the wavelength can be derived in terms of the potential field. If an electron beam is accelerated by a potential V, then the potential energy (Ve) is equal to the kinetic energy of the electrons, since energy is conserved.

$$\text{i.e.} \quad Ve = \frac{1}{2} mu^2 \qquad 1.2$$

where e is the electronic charge. Substituting for the value of u from de Broglie relation 1.1, we get

$$\lambda = \frac{h}{\sqrt{2mVe}} \qquad 1.3$$

By substituting in the values of h, m and e, Equation 1.3 becomes:-

$$\lambda = \sqrt{\frac{150}{V}} \qquad 1.4$$

where V is measured in volts and λ is measured in Å° units.

Since V is often very large, the electrons can reach velocities comparable with the speed of light C, and the relativistic increase in mass of the electron should be taken into account. This can be done by using the Einstein relativity equation and replacing V in Equation 1.3 by the relativistic potential Vr, given by:-

$$Vr = V \left[1 + Ve/2m_o C^2 \right] \qquad 1.5$$

where m_o is the electron rest mass which is related to the relativistic mass m by the following equation:-

$$m = \frac{m_o}{\sqrt{1 - u^2/c^2}} \qquad 1.6$$

Hence, the relativistic wavelength becomes:-

$$\lambda = \frac{h}{\sqrt{2m_o Ve\left(1+\frac{Ve}{2m_o c^2}\right)}} \qquad 1.7$$

Thus for the large accelerating voltages normally used in the electron microscope, we need to calculate wavelengths of electrons from Equation 1.7 since the correction factor $(1+Ve/2m_oc^2)$ becomes large. Figure 1.1 shows the relativistic dependence of wavelength λ on acc. voltage.

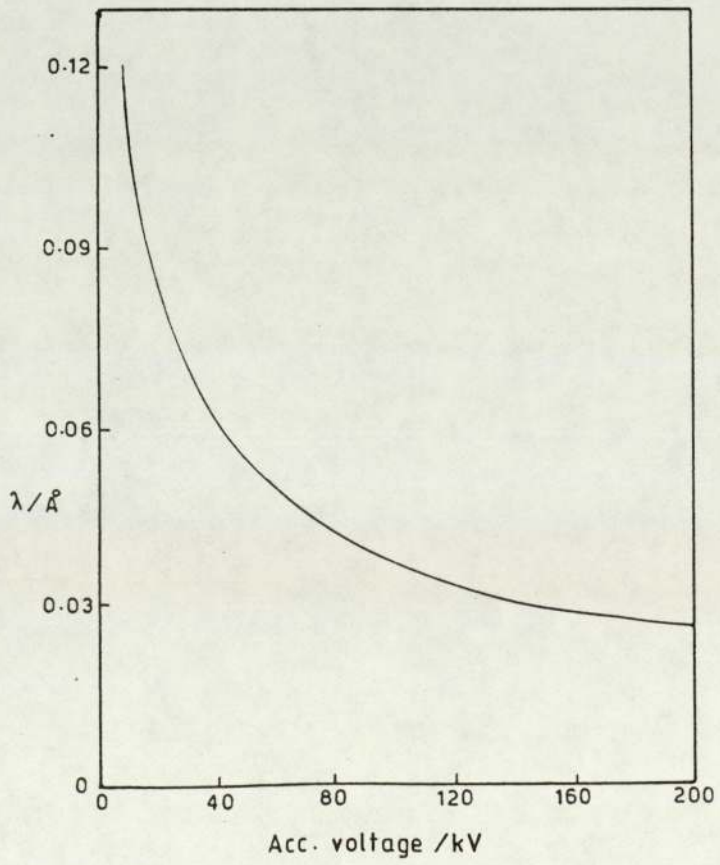

Fig. 1·1 The relativistic dependence of wavelength on accelerating voltage.

Consider a monoenergetic electron beam, as normally used in a transmission electron microscope, incident normally onto a thin crystalline specimen. The intensity distribution below the specimen and in the back focal plane of the objective lens (diffraction pattern) is of great importance in (a) structural analysis, (b) the scattering processes involved inside the specimen, and (c) in the proportional analysis of the constituents.

The interaction between electrons and atoms is much greater than that between x-ray and atoms and so the techniques of electron and x-ray diffraction, which both give information about the specimen's crystallographic structure, are complementary.

Electron diffraction is most useful when very thin layers are to be investigated and x-ray diffraction when thick specimens are to be investigated.

Before going further, we need to throw some light on the interaction of electron beams with the specimen material.

Electron scattering may be either inelastic or elastic. An atom scatters electrons inelastically when there is an interaction of the incident electrons with the electronic fields within the atom. In this scattering, the electrons inside the specimen may lose energy as a result of absorption, and this energy may be transferred in the form of atomic excitation, heat, ionization,

secondary emission, or x-rays. Measurement of these energy losses can give information about the chemical composition of the specimen.

In elastic scattering the electrons do not lose any appreciable energy. The effect of the positively charged nucleus is to produce a scattering of electrons with a change in direction only. This is due to the comparatively massive weight of the nucleus, which does not move during the interaction. The elastic scattering should, therefore, provide information about the shape and constituents of the atomic material within the specimen.

The elastic scattering of electrons is said to be incoherently scattered when considering amorphous films (i.e. the specimen atoms are incoherently arranged as compared to those in crystals). When a monochromatic electron beam is incident upon a crystalline material, the elastically scattered electrons act as coherent waves which have definite phase relations with each other and with the incident electron beam. In this interaction, the effects of diffraction and subsequent interference are obtained over large angles. The coherently scattered electrons give rise to the diffraction pattern and play a very important part in image formation and contrast. These interactions are illustrated schematically in Figure 1.2.

If the specimen to be examined is a polycrystalline metal film, the electron diffraction pattern will consist

of a number of concentric rings because the incident electron beam illuminates many crystals whose diffracting planes are positioned at all azimuthal angles to the beam.

These ring patterns arise from the elastic scattering of electrons in the crystalline region. Electrons which are inelastically scattered, together with electrons which are elastically scattered in non-crystalline regions, form a diffuse background. However, in crystal structure determination, or where the proportion of the constituents are required, it is necessary to measure the relative intensities of each diffracted ring.

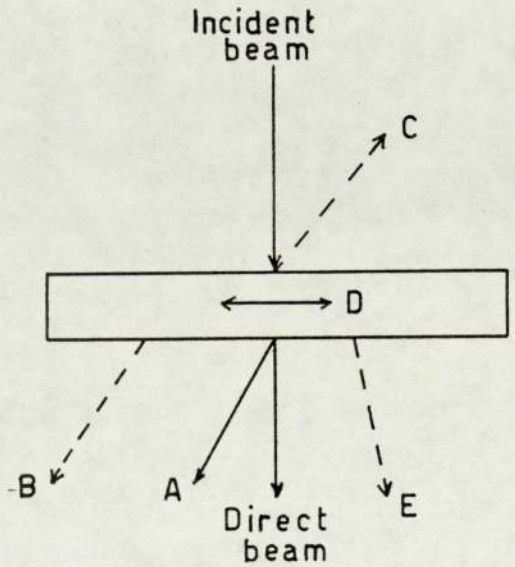

Fig.1.2 Schematic diagram of the interaction of an electron beam with specimen material.A, Coherent elastic scattering. B, Incoherent elastic scattering. C, Back scattered electrons. D, Absorption energy lost inside the specimen. E, Inelastic scattering.

There are two possible approaches to the use of electron diffraction in quantitative analysis, based respectively on the kinematic and dynamic theories of electron diffraction. In the kinematic theory it is assumed that the wave incident on each atom is simply the primary wave falling on the crystal, and therefore the total amplitude of the diffracted wave is proportional to the number of atoms in the crystal. In the dynamic theory one takes into account the fact that the reflected beam is itself reflected by the same planes of atoms. In this approach, multiple scattering is allowed and therefore the diffracted intensities are large and the diffracted waves can themselves be scattered. After the electron beam passes through a sufficient thickness of the crystal a dynamical equilibrium is established between the intensities of the original and diffracted beams.

The complete determination of structures requires an estimation of the intensities in the electron diffraction pattern, yet the equations for the calculation of the intensities in the kinematic and dynamic theories differ considerably. The diffracted intensity under kinematical conditions is formed from singly scattered electrons only, whilst under dynamical conditions the diffracted intensity is formed from plurally or multiply scattered electrons.

Investigation of the factors which influence the degrees

of scattering are of great importance in the quantitative analysis of electron diffraction patterns. Probably the best method for studying the relationships between kinematical conditions and single scattering, and between dynamical conditions and plural (or multiple) scattering is through electron diffraction contrast measurements.

The contrast of an electron diffraction pattern may be defined as the ratio of the integrated intensity of the ring (i.e. total intensity diffracted by a particular set of atomic planes) to the integrated intensity of the background at the same radius. Figure 1.3 shows an illustration of the variation in the density of blackening (D) of the photographic film at a particular diffraction ring with the radii R. In this technique, single and plural scattering conditions for a wide range of specimen thicknesses and accelerating voltages can be investigated. The effects of the amorphous content or the amorphous substrate beneath the specimen film (28) can also be investigated and consequently the intensity anomalies of the diffraction pattern can then be explained.

The development of the three-stage transmission electron microscope and of selected area electron diffraction techniques offers considerable advantages over the use of general area patterns from entire polycrystalline specimens. In the former system, a small part of the undistorted image of the electron microscope object may

be selected by means of an aperture in the image plane of the objective lens. The diffraction pattern of the selected area may then be obtained by using the projector lenses to image and magnify the back focal plane of the objective lens on the screen. A great advantage of this system is that it allows the diffraction pattern to be correlated with the microscope image.

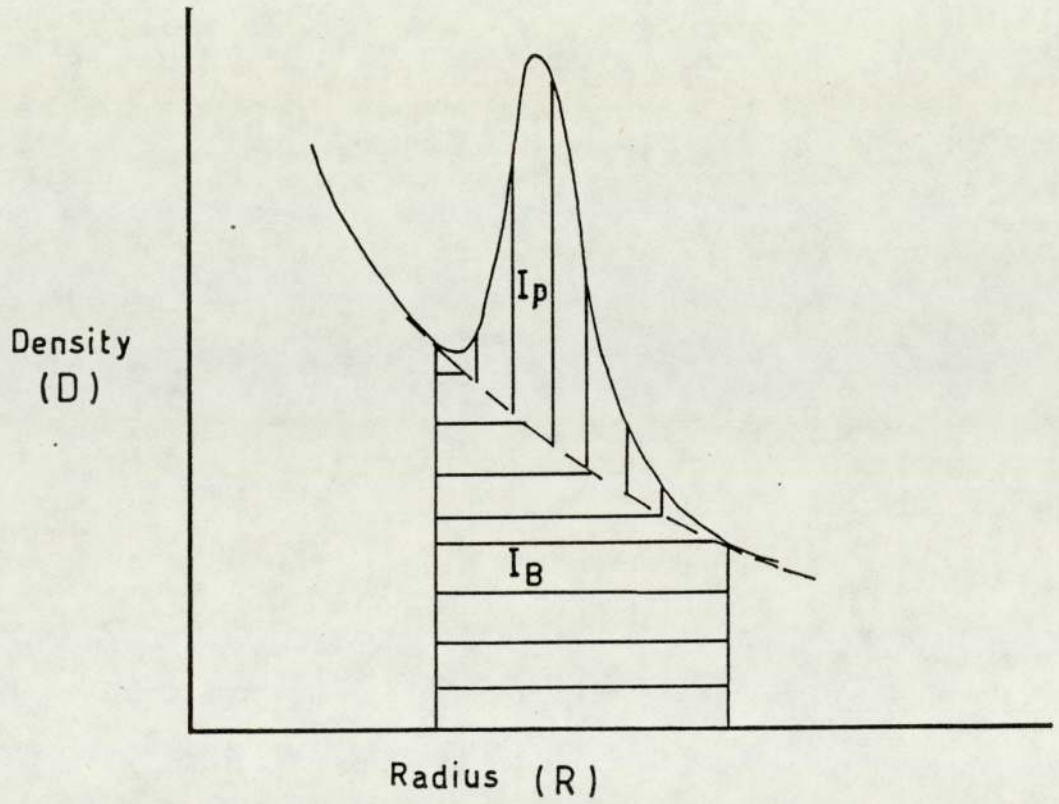

Fig.1.3 Schematic diagram of the intensity distribution in diffraction contrast measurement.

1.2 Previous work.

The intensities of the electron diffraction Debye-Scherrer rings were first studied by Thomson (2) in order to verify de Broglie's expression. In his experiment he used the diffraction of cathode rays with a beam energy of 30kV through a thin polycrystalline metal film of about 10nm thick, and later this subject was studied by several other investigators (3-5). Thomson (2) and Shirai (3) found that the observed intensities fit very well with those calculated theoretically in accordance with the kinematical theory, but T.Tol and Ornstein (4) and Lennander (5) found that the observed intensity deviates from the kinematical value. It has been reported by Kuwabara (6,7) that with very strong interaction in the diffraction of electrons, the kinematical theory fails and the dynamic theory must be referred to, even for comparatively small crystals, thus many electron diffraction phenomena should be interpreted according to the dynamical theory of electron diffraction. Blackman (8) treated these contradictions theoretically and concluded that the deviation from the kinematical theory is caused by dynamical effects in the diffraction process.

In the study of the applicability of these two theories, the relative energy of the incident electrons, film thickness, and the crystallite size clearly play an important role.

Pinsker (9), stated that the kinematical theory can safely be applied to films composed of crystallites smaller than 10nm. Specimens studied by Yamzin (10) were Al, Cu, Ag, Au, Sn and Zn with an accelerating voltage varying from 38kV to 56kV. He stated his conclusion in terms of film thickness and concluded that the kinematical theory holds for thicknesses less than 50nm, except for heavy materials such as Au. Contradicting this conclusion, Kuwabara (7) studied the specimens Al, Ag, Au, NaCl and KCl, using an accelerating voltage from 32kV to 60kV and concluded that the dynamical effect appears for films thinner than 10nm for all the materials examined. Although Kuwabara (6,7) measured the crystallite size, he concluded that the kinematical theory can be applied when the crystallite size of the specimen is very small, namely the kinematical theory was applicable for crystallites smaller than 6.8nm, 2.9nm and 2.7nm for Al, Ag and Au respectively. Also he stated that the temperature effect, which was neglected by Yamzin (10) and Blackman (8), is too large to be ignored and must be taken into account.

Kimoto (11) studied the anomaly of electron diffraction powder patterns of minute silver crystallites. He ascribed the anomalous behaviour of the intensity not to the dynamic effect, nor to the absorption of the electron beam by the sample, nor to the preferred orientation of the specimen, but suggested that the

anomoly was caused by the stacking fault parallel to the (111) plane of the crystal.

It is well known that most of the electron diffraction experiments carried out so far have only involved crystal structure determination, the intensity of the diffraction pattern being measured and the results interpreted according to the kinematical or dynamical theories of electron diffraction. Very few attempts have been made to use electron diffraction methods for a quantitative analysis of the proportion of the constituents of a composite specimen from a measurement of the diffracted intensity. The factors which might be expected to influence such an analysis are the arrangement of the diffracting component (i.e. whether the specimen is laminar, columnar or a powder), the overlap of diffraction maxima, the doubt as to whether or not to use the kinematical theory or the dynamical theory, the extent of amorphous content and the variation in crystallite size between the components of the composite specimen.

Several experiments had been performed for different materials in the form of composite laminar specimens to study the possibilities of using the electron diffraction techniques for proportional analysis of the constituents. These experiments are based on relating the relative integrated intensities of the diffraction rings of the two components with their film thicknesses.

For example, Quinn and Dawe (12) showed for composite specimens of Cu and Al that there is a linear relationship between the thickness ratios and the integrated intensity ratios for selected pairs of lines from each component of the composite specimens. Their results were based on a limited number of observations. In 1976 Quinn and Boxley (13) covered a large range of thickness ratios and different accelerating voltages by using an electron microscope in the "selected area electron diffraction mode" of operation. They found that both kinematic and dynamic theories needed to be considered in the interpretation of the results because of the deviation of the experimental results from the expected kinematical values. In further studies Quinn and Liddicoat (14) found that the crystallite size is an important factor and it was consistent with the nonlinearity in the intensity ratio versus thickness ratio plot. In 1977 Quinn and Hayes (15) published their work in "Proportional analysis of composite polycrystalline specimens of Cu and Al by electron diffraction", in which a theoretical relationship was derived. This simple theory which related the relative integrated intensities of the diffraction rings to the thickness ratio of the two constituent films of the composite specimen. This relationship was described by the following equation:-

$$(I'_{hkl})_1/(I'_{hkl})_2 = C.(k_{hkl})_1/(k_{hkl})_2.(t_1/t_2) \qquad 1.8$$

Where $(I'_{hkl})_1$ and $(I'_{hkl})_2$ are the relative integrated

intensities of the diffraction rings from material 1 and 2 of the composite specimen respectively, $(k_{hkl})_1$ and $(k_{hkl})_2$ are the fractions of electrons scattered through angles (θ_1) and (θ_2) per unit length of films 1 and 2, t_1 and t_2 are the thicknesses of the films 1 and 2, and C is a constant which had been introduced to enable Equation 1.8 to be compared with the experimentally measured ratios of relative integrated intensities.

They concluded that the observed difference between the ratio of the integrated intensities predicted by Equation 1.8 and the experimentally measured ratio of these intensites, could arise only from the dynamical effect.

Later Quinn and Al-Bermani (16) performed many experiments for different materials as single and composite specimens with a wide range of accelerating voltages. They found that for single specimens, both kinematical and dynamical conditions can occur, but the kinematical conditions dominated and for the composite specimens showed that the basic Equation (1.8) could be used to determine (t_1/t_2), provided that i) $(k_{hkl})_1$ and $(k_{hkl})_2$ were given by kinematical theory of electron diffraction, ii) the crystallite size is less than the extinction distance, and iii) the average interplanar spacing of the two diffraction maxima is greater than about 0.14 nm for the Al and Cu combination and about 0.2 nm for the Al and Ni combination.

Diffraction contrast may be regarded as another method of using the diffraction technique for quantitative analysis, particularly when the proportion of the amorphous content is to be investigated. Also in this technique single and plural scattering conditions can be investigated which may be considered as added information to the scattering processes of electrons.

It is well known that if the film thickness is increased, or the accelerating voltage reduced, the contrast in the diffraction pattern is reduced. Moreover it was reported by Halliday (17) that the contrast of a diffraction pattern is poor if the crystallite size is small and if the specimen contains a high proportion of amorphous material, or is supported on an amorphous substrate. The contrast of a diffraction pattern also depends upon the amount of plural electron scattering (i.e. in which the electrons are scattered more than once, but not a large number of times), because the diffracted electrons are scattered out of the rings into the background causing contrast to deteriorate.

Ellis (18) and Halliday (17) used the concept of peak contrast, which is defined as the ratio of the peak intensity of the ring to that of the background measured at the same position. It is convenient in practice, but probably inaccurate, to measure the peak contrast because of the possible variation in the crystallite size from one specimen to another.

Ellis (18) used films of thallium chloride and aluminium supported by collodion films on copper grids. The results showed a decrease in peak contrast with specimen thickness for different voltages, the effect of increasing voltage being to increase the contrast at any given film thickness. Halliday (17) suggested the idea of combining thickness and voltage through the use of the electron mean free path and developed an empirical universal formula relating the peak contrast in plural scattering conditions Cp to that in single scattering condition Cs as follows:-

$$Cp = Cs/\,[\,1+0.06(t/\lambda p)^2 + 0.016(t/\lambda p)^3\,] \qquad 1.9$$

where λp is the electron mean free path (which, in iron, is almost equal to the mean free paths for elastic, λ_e, and inelastic λ_i, scattering). If they are unequal, λp should be replaced by the smaller mean free path. Clearly $Cp \simeq Cs$ for $(t/\lambda p) \leqslant 1$ (according to Equation 1.9), where t is the thickness.

The contrast of a diffraction pattern is weak when the specimen contains a high proportion (k') of amorphous material, so that one should expect, in very thin specimens or in single scattering conditions, that the contrast would not remain constant as was reported by the previous workers, but it will deteriorate as k' increases.

The present work includes an experimental investigation

of the limit of validity of the kinematic and dynamic theories of electron diffraction. Hopefully, the information gained could be used to allow a quantitative analysis for the diffracted intensity to be made. For example, the proportional analysis of composite polycrystalline specimens, in which identification of the relative constituents from the measurement of the relative integrated intensities of the diffraction rings can be made,and also the investigation into the effect of the proportion of amorphous content by using the diffraction contrast method.

Single and composite polycrystalline specimens from different thicknesses and materials were prepared by vacuum evaporation onto carbon-coated electron microscope grids. Facilities provided for film thicknesses measurement. Electron diffraction patterns were obtained by using an electron microscope in the selected area electron diffraction techniques with different accelerating voltages up to 1000kV. The crystallite sizes of the specimens were measured using dark field techniques. The relative integrated intensities in each diffraction pattern were measured using microdensitometer traces of the diffraction pattern micrograph.

For single lamina specimens of copper and α-iron, the n value for each specimen was obtained by plotting Equation 2.22. This equation was originally derived from the total diffracted intensity for kinematic and

dynamic theories, given by Rymer (19). It was shown that the dynamical effect appears even for very high voltages for both materials.

Also it was shown from the values of n for the diffraction pairs, that there is a transition from dynamical to kinematical intensities as the average Bragg angle $\bar{\theta}$ of the diffraction pairs increased. The criterion of the critical thickness (see Equation 2.19), given by Rymer (19), was found to be a very good approximation to the limit of validity of the kinematic and dynamic theories.

The composite specimens of copper-iron combinations showed that for all voltages used, the diffracted intensities from the two components were not entirely produced under kinematical conditions nor under dynamical conditions alone, but was suggested that both kinematical and dynamical effects contributed to the final intensities. It is possible that the relative integrated intensity from one lamina may be given by kinematical theory whilst the relative integrated intensity from the other lamina may be given by the dynamical theory (or vice-versa). This should be taken into account (see Equations 6.1 and 6.2) in determining the thickness ratio from the relative integrated intensity ratio.

The aim of the experimental investigation into diffraction contrast (28) was i) to repeat Halliday's (17) work

for iron specimens extending it to higher voltages, to explore the region of (t/λ_T) less than unity, where λ_T is the total electron mean free path and is given by:-

$$\frac{1}{\lambda_T} = \frac{1}{\lambda_e} + \frac{1}{\lambda_i} \qquad 1.10$$

ii) To extend Halliday's work for other materials, such as aluminium and silver, which are respectively low and high in atomic numbers compared with iron, and finally, iii) to investigate the effect of amorphous carbon support film upon contrast.

The contrast variation results obtained from each material at different accelerating voltages with the ratio (t/λ_T) were fitted onto a single curve. The effect of the relative proportion of amorphous material, under single scattering conditions, tends to decrease the contrast as the specimen thickness decreases except for heavy materials such as silver. The variation of contrast from the confirmatory experiment, shown in Section 5.3 (Chapter Five) emphasized such an effect.

CHAPTER TWO

ELECTRON DIFFRACTION IN POLYCRYSTALLINE SPECIMENS.

2.1 The ring patterns.

When a monochromatic beam of electrons is transmitted in vacuum through a thin film of polycrystalline material, i.e. one which consists of a large number of small crystals randomly oriented with respect to each other, most of the electrons are undeviated. These electrons will form an intense area of blackening on the photographic plate, which we call the "centre-spot". There will, however, be a number of concentric rings formed around the centre-spot from the electrons elastically scattered in the crystalline regions, which have been diffracted according to the Bragg relation.

$$\lambda = 2d \sin\theta \qquad 2.1$$

where λ is the wavelength associated with the electrons, d is the interplanar spacing between the planes containing the atoms and θ is the Bragg angle. These will be superimposed on the general background, which has been made from the electrons inelastically scattered by the electric fields associated with the atoms of the material.

It is obvious that the radii of these rings can be calculated in connection with the θ of Bragg relation as shown in Figure 2.1. In this figure a beam of electrons is incident on a polycrystalline specimen S, the

diffracted beams will form a cone of semi-angle 2θ and therefore the radius R of the ring on photographic plate will be

$$\tan 2\theta = \frac{R}{L} \qquad 2.2$$

where L is the distance between the specimen and the photographic plate.

It is well known that the angle 2θ is very small when the accelerating voltage is in the order of hundreds of kilovolts. Hence we may write

$$\tan 2\theta = 2\theta$$

Therefore by substituting the value of 2θ in Equation 2.1 of Bragg relation we get

$$Rd = \lambda L \qquad 2.3$$

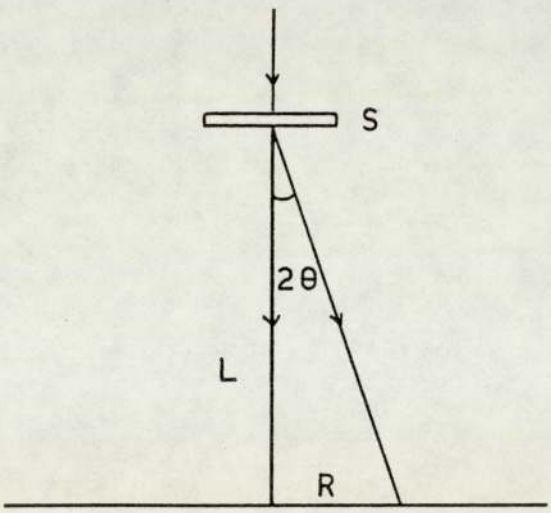

Fig.2.1 Simple diagram showing the diffracted and undiffracted beams.

It will be seen later that the kinematic and dynamic theories of electron diffraction give a satisfactory account of the main features of the diffraction patterns

obtained. Although the kinematic theory of electron diffraction provides a useful quantitative guide to the interpretation of the diffraction patterns, it is certainly valid only when the amplitude of the diffracted wave is small in comparison with the incident wave amplitude.

2.2 The intensity of the diffraction rings obtained from polycrystalline metal films.

A diffraction ring pattern can be used for other applications than the calculation of interplanar spacing and the identification of the crystal structure. The intensities of the diffracted rings can also be used to study the scattering processes of the incident electron beam with the atoms of the crystal lattice. In order to be able to interpret electron diffraction patterns in detail, it is essential to have a thorough understanding of the factors which determine the intensities of diffracted beams.

According to the kinematical and dynamical theories of electron diffraction, the intensities of the electron diffraction patterns differ considerably. It is assumed, in the kinematical theory, that only a negligible fraction of an incident electron beam is elastically scattered by the atoms of the crystal and leaves the crystal without further interaction. This means that this theory will be applied when the intensities of the diffracted beam are low, in other words, when a fast

electron beam is incident on a thin crystalline specimen.

The strong interaction of the incident electron beam with the atoms of the specimen, forms the basis of the dynamical theory. The dynamical theory becomes more essential when a thick specimen is used. After the incident electron beam passes through a sufficient thickness of crystal, a dynamical equilibrium is created between the intensities of the original and diffracted beams. This theory takes into account the fact that some electrons are diffracted back into the original direction.

2.3 The diffracted intensity in single lamina specimen.

Consider I_o is the intensity of the electron beam proceeding in the direction perpendicular to a single lamina specimen of thickness t as shown in Figure 2.2. The film is considered to be polycrystalline material. The transmitted intensity I_T is given by the exponential decay law.

$$I_T = I_o \, e^{-Kt} \qquad 2.4$$

where K is the total number of electrons scattered through all angles, by all processes, per unit length of path through the specimen.

To calculate the diffracted intensity entering one diffraction ring, I'_{hkl}, let us assume a thin sheet of thickness dx situated at a distance x from the entry face of the specimen. Then according to Equation 2.4

$$I_x = I_o e^{-Kx} \qquad 2.5$$

Let k_{hkl} be the fraction of electrons diffracted into the hkl diffraction ring per unit length through an angle 2θ, where θ is the Bragg angle. Therefore, a fraction of $(I_x k_{hkl} dx)$ of electrons will be diffracted into the solid angle 2θ. However, the diffracted beam $(I_x k_{hkl} dx)$ will suffer attenuation of the amount $e^{-K(t-x)}$ along its path before it emerges from the exit face of the specimen, which is due to the scattering by the atoms. So that the total intensity of the diffracted electrons into an angle 2θ could be found by integrating for the values of x from o to t and by substituting the value of I_x in Equation 2.5, we have

$$I'_{hkl} = \int_o^t I_o k_{hkl} e^{-Kx} . e^{-K(t-x)} \, dx$$

Then

$$I'_{hkl} = I_o k_{hkl} t \, e^{-Kt} \qquad 2.6$$

Equating $\frac{dI'_{hkl}}{dt}$ to zero in Equation 2.6, it can be shown that the maximum ring intensity can be obtained when $(t = 1/K)$ and falls rapidly with increasing film thickness.

2.4 The diffracted intensity in double lamina specimen.

In proportional analysis of composite polycrystalline specimen, Quinn and Hayes (15) assumed (see Figure 2.3) that the diffracted intensity from lamina of thickness

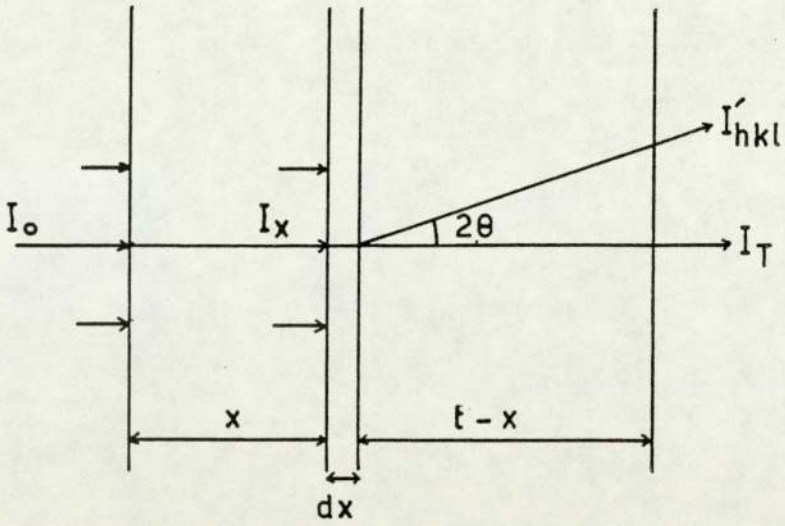

Fig. 2·2 Diffracted intensity through single lamina specimen.

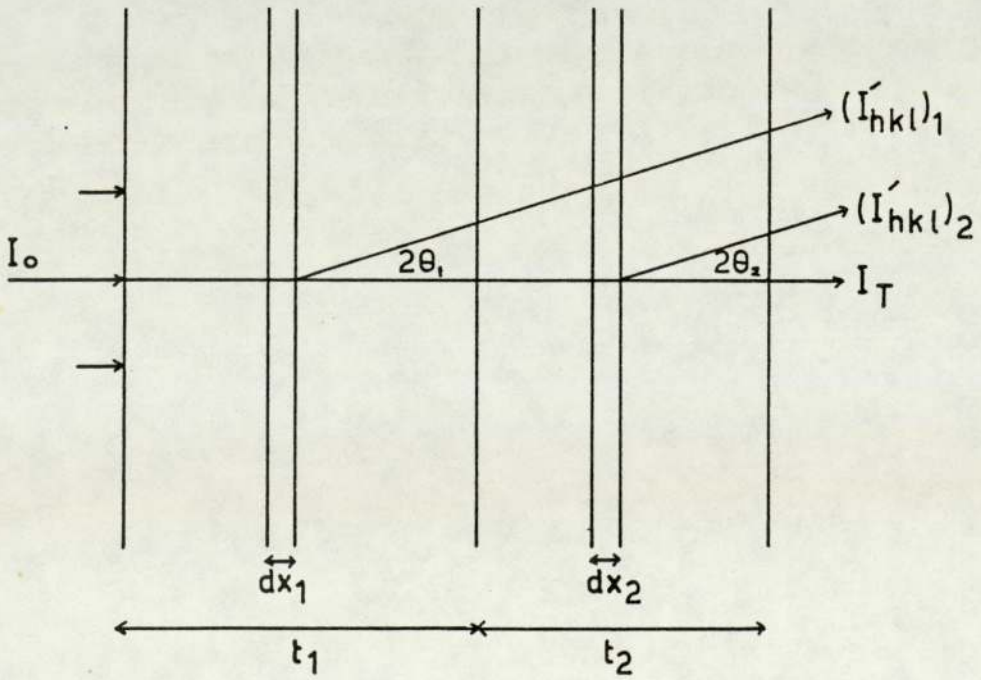

Fig. 2·3 Diffracted intensity through double laminae specimen.

t_1 will suffer attenuation by amorphous scattering whilst passing through lamina of thickness t_2 and vice versa. Let us use subscripts 1 and 2 to denote the associated particular parameters in lamina 1 and 2 respectively. Therefore the diffracted intensity $(I'_{hkl})_2$ by lamina 2 has been attenuated by the factor $e^{-K_1 t_1}$ through its path in lamina 1, also the diffracted intensity $(I'_{hkl})_1$ by lamina 1 will suffer attenuation in lamina 2 by the factor $e^{-K_2 t_2}$.

Using Equation 2.6, we have $(I'_{hkl})_1$ and $(I'_{hkl})_2$ after passing through the total thickness of the specimen, given by

$$(I'_{hkl})_1 = I_o (k_{hkl})_1 t_1 \, e^{-K_1 t_1 - K_2 t_2} \qquad 2.7$$

$$(I'_{hkl})_2 = I_o (k_{hkl})_2 t_2 \, e^{-K_1 t_1 - K_2 t_2} \qquad 2.8$$

From the last two equations, one could find an expression relating the ratio of the relative integrated intensities from the diffraction rings formed by material 1 and 2, and find that we no longer need concern ourselves with the total scattering factors K_1 and K_2, namely :-

$$\frac{(I'_{hkl})_1}{(I'_{hkl})_2} = \frac{(k_{hkl})_1}{(k_{hkl})_2} \cdot \frac{t_1}{t_2} \qquad 2.9$$

2.5 The relative integrated intensity of an electron beam diffracted by a polycrystalline specimen.

It is convenient in practice to measure the relative integrated intensity of the diffraction rings, so that we can avoid the error which might be due to the absorption of the incident beam by the specimen or the supporting grids. Theoretically there are two possible ways to calculate the intensity of an electron diffraction maxima from a crystalline specimen, namely according to the kinematical theory or the dynamical theory of electron diffraction.

2.5.1 The kinematical formula of the relative integral intensity.

In this theory, it is assumed that only a small proportion of an incident electron beam is scattered by the atoms of the crystal. This means that we can assume that an electron is elastically scattered only once whilst it is passing through the crystal and leaves the crystal without further interaction. Therefore, we do not have to take into account any attenuation of the incident beam on the way through the crystal.

It has been shown (see Equation 3.18, reference (19)) that the intensity of the electron beam diffracted by a particular set of atomic plane (hkl) into a complete diffraction ring I'_{hkl}, would be

$$\frac{I'_{hkl}}{I_o} = \frac{[F_e(\theta)]^2 . \lambda^2 . t . d_{hkl}}{2v^2} \qquad 2.10$$

where I_o is the intensity of incident electron beam, $F_e(\theta)$ is the structure factor, λ is the wavelength of the electron beam, t is the thickness of the specimen, d_{hkl} is the interplanar spacing between the atomic planes given by Miller indices (hkl) and v is the volume of the unit cell.

Normally, one would not measure the intensity of a complete diffraction ring, but the intensity across the profile of the diffraction ring with a slit of length ℓ placed tangentially to the ring. Such a slit would admit a fraction $\ell/2\pi R$ of the electrons diffracted into a complete ring of radius R. Substituting for the value of R in Equation 2.3, we get:-

$$\frac{\ell}{2\pi R} = \frac{\ell\, d_{hkl}}{2\pi \lambda L}$$

Therefore, Equation 2.10 becomes:-

$$\frac{I_{hkl}}{I_o} = \frac{[F_e(\theta)]^2 . \lambda . t . \ell . d_{hkl}^2}{4\pi L v^2} \qquad 2.11$$

where I_{hkl} is the diffracted intensity per unit length.

This expression should be modified to allow for thermal vibrations of the atoms in crystal (the Debye-Waller temperature factor) and the probability of a particular plane of atoms being available for diffraction (the

multiplicity factor, P_{hkl}).

Hence:-

$$\frac{I_{hkl}}{I_o} = \frac{[F_e(\theta)]^2 . \lambda . t . \ell . d_{hkl}^2 . e^{-2D_{hkl}} . P_{hkl}}{4\pi Lv^2} \qquad 2.12$$

where $e^{-2D_{hkl}}$ is the Debye-Waller temperature factor for the kinematical expression.

If it is desired to measure the ratio of the relative integrated intensities of the rings in a diffraction pattern, then these ratios could be found by using Equation 2.12 for any pair of diffraction maxima. So that:-

$$\frac{I_1}{I_2} = \frac{[F_e(\theta)_1]^2 . d_1^2 . e^{-2D_1} . P_1}{[F_e(\theta)_2]^2 . d_2^2 . e^{-2D_2} . P_2} \qquad 2.13$$

where the subscript 1 relates to the (hkl) of the strongest line and subscript 2 stands for all the other possible (hkl) maxima in the electron diffraction pattern.

2.5.2 The dynamical formula of the relative integrated intensity.

We know that, under the conditions where the dynamical theory applies, an equilibrium situation occurs between the intensities of the original beam and the diffracted beam. In deriving the dynamical formula of the relative integrated intensity allowance is made for the fact that some electrons are diffracted back into the original directions. It can be shown (see Equation 6.50, reference (19)) that for a specimen consisting of a single layer of crystal, the diffracted intensity I'_{hkl} for a complete diffraction ring, would be:-

$$\frac{I'_{hkl}}{I_o} = \frac{F_e(\theta) \cdot \lambda \cdot d_{hkl}}{4v} \qquad 2.14$$

If the specimen (of thickness, t) consists of a number of such layers each of average crystal thickness ϵ, then the above expression of the relative integrated intensity must be multiplied by (t/ϵ)

Hence:-

$$\frac{I'_{hkl}}{I_o} = \frac{F_e(\theta) \cdot \lambda \cdot d_{hkl}}{4v} \cdot \frac{t}{\epsilon} \qquad 2.15$$

To allow for thermal vibrations, multiplicity factor, attenuation factor which due to the inelastic scattering and the method of measuring the intensities, Equation 2.15 must be multiplied by $e^{-D_{hkl}}$, P_{hkl}, e^{-Kt} and $(\ell d_{hkl}/2\pi\lambda L)$. Therefore, the full expression of the relative integrated intensity becomes

$$\frac{I_{hkl}}{I_o} = \frac{F_e(\theta) \cdot t.\ell.d_{hkl}^2.P_{hkl}.e^{-D_{hkl}}.e^{-Kt}}{8\pi vL\epsilon} \qquad 2.16$$

To compare between the relative integrated intensities in a diffraction pattern, one must measure the ratio of the relative integrated intensity of the strongest line to any other diffraction maxima. This ratio should be theoretically given by :-

$$\frac{I_1}{I_2} = \frac{F_e(\theta)_1.e^{-D_1}.d_1^2.P_1}{F_e(\theta)_2.e^{-D_2}.d_2^2.P_2} \qquad 2.17$$

where the subscripts (1) and (2) are related to the hkl of the strongest line intensity and for all the other possible diffraction maxima respectively.

2.5.3 Comparison between the kinematical and dynamical formulae.

A possible approach for the limit of validity of the kinematical theory could be made in comparing expressions 2.10 and 2.14 for the total diffracted intensity according to the kinematical and dynamical theories, namely :-

$$\frac{(I'_{hkl}/I_o)\text{Kinematical}}{(I'_{hkl}/I_o)\text{Dynamical}} = \frac{2F_e(\theta).\lambda.t}{v} \qquad 2.18$$

At a certain thickness (t_c), one obtains equality between the kinematical and dynamical intensities, namely :-

$$t_c = \frac{V}{2F_e(\theta).\lambda} \qquad 2.19$$

For a thickness greater than t_c, it is suggested that the dynamic theory should operate. There is no general agreement about the criterion to be used, but Rymer(19) suggests that the crystal thickness should not exceed the extinction distance Δ for using the kinematic theory, where Δ is given by

$$\Delta = \frac{\pi V}{F_e(\theta).\lambda} \qquad 2.20$$

It is important to notice here that the crystal thickness in Equation 2.19 and the extinction distance in Equation 2.20 are inversely proportional to the structure factor. This means that, at a given wavelength λ, each diffraction ring in a diffraction pattern will have its own associated crystal thickness t_c or extinction Δ distance . However, it would be possible for the inner rings of an electron diffraction pattern to have their t_c different from the t_c for the outer rings. Hence, if the specimen thickness does lie between these two values, then the outer rings will have their intensities given by one theory whilst the inner rings will have their intensities given by the other theory.

2.6 Theoretical analysis of the relative integrated intensity for single and composite polycrystalline specimens.

In this section, we shall examine whether a given specimen is diffracted according to the kinematical or dynamical theory of electron diffraction, by comparing the intensity I_2 of each diffraction maximum with the strongest intensity I_1, in a diffraction pattern.

Comparing Equations 2.13 and 2.17 of the ratio of the relative integrated intensities for kinematical and dynamical theories respectively, one could put them in one expression.

$$\frac{I_1}{I_2} = \left[\frac{F_e(\theta)_1 \; e^{-D_1}}{F_e(\theta)_2 \; e^{-D_2}}\right]^n \cdot \frac{d_1^2 \; P_1}{d_2^2 \; P_2} \qquad 2.21$$

when $n = 1$, dynamical theory

$n = 2$, kinematical theory

and the last expression could be written in the form of

$$\text{Log}\left[\frac{I_1}{I_2} \cdot \frac{d_2^2 \; P_2}{d_1^2 \; P_1}\right] = n \; \text{Log}\left[\frac{F_e(\theta)_1 \; e^{-D_1}}{F_e(\theta)_2 \; e^{-D_2}}\right] \qquad 2.22$$

Provided that the extinction distance is such that I_1, and I_2 are both kinematical or both dynamical, then a graph of $\text{Log}\left[\frac{I_1}{I_2} \cdot \frac{d_2^2 \; P_2}{d_1^2 \; P_1}\right]$ versus $\text{Log}\left[\frac{F_e(\theta)_1 \; e^{-D_1}}{F_e(\theta)_2 \; e^{-D_2}}\right]$ will give a straight line of slope (n) equal to one or two respectively. In general, I_1 and I_2 need not be theoretically given by the same theory, so that Equation 2.22

should be used for computing n for each pair of diffraction maxima. In this way, possible effects at atomic number, specimen thickness and electron accelerating voltage can be investigated.

If the specimen is in the form of composite laminae of two different materials, one could use Equation 2.9 which related the ratio of the integrated intensities of the complete diffraction rings from each lamina with their thicknesses ratio, through the expression

$$\frac{(I'_{hkl})_1}{(I'_{hkl})_2} = \frac{(k_{hkl})_1}{(k_{hkl})_2} \cdot \frac{t_1}{t_2} \qquad 2.9$$

The last expression should be modified to allow for the fact that one must use the intensity across the profile of the diffraction ring with a slit of length l placed tangentially to the ring of radius R. Therefore, Equation 2.9 must be multiplied by $(\frac{\ell}{2\pi R_1} / \frac{\ell}{2\pi R_2})$ and in conjunction with the Equation 2.3 one obtains the following Equation:-

$$\frac{(I_{hkl})_1 / (I_{hkl})_2}{t_1 / t_2} = \frac{(k_{hkl})_1}{(k_{hkl})_2} \cdot \frac{(d_{hkl})_1}{(d_{hkl})_2} \qquad 2.23$$

where I_{hkl} is the integrated intensity per unit length.

Equation 2.9 was derived from Equation 2.6 for a specimen in the form of a lamina, given by

$$\frac{I'_{hkl}}{I_o} = k_{hkl} \cdot t \cdot e^{-Kt} \qquad 2.6$$

It is worth remembering that in deriving Equation 2.6, account was taken of the diminution of the incident beam and the diffracted beam by total scattering. To allow Equation 2.23 to be used in the analysis of the composite laminae specimen, one should find the theoretical expressions of k_{hkl} for kinematical and dynamical theory of electron diffraction.

Comparison of Equation 2.6 with Equation 2.10, suitably modified to allow for thermal vibrations of atoms, the multiplicity factor and the diminution by total scattering (e^{-Kt}), gives us the kinematical theoretical expression for k_{hkl}, namely:-

$$(k_{hkl})_K = \frac{[F_e(\theta)]^2 . \lambda^2 . d_{hkl} . e^{-2D_{hkl}} . P_{hkl}}{2v^2} \qquad 2.24$$

In this expression, the exponential term has been ignored since Equation 2.10 did not allow for total scattering.

In the same way, when comparing Equation 2.6 with Equation 2.15, thermal vibrations of atoms and the multiplicity factor must also be taken into account, so that the dynamical theoretical expression for k_{hkl} is:-

$$(k_{hkl})_D = \frac{F_e(\theta) . \lambda . d_{hkl} . e^{-D_{hkl}} . P_{hkl}}{4v\epsilon} \qquad 2.25$$

Therefore, if the conditions are those of the kinematical theory, then Equation 2.23 can be written from Equation

2.24 to give the following expression:-

$$\frac{(I_{hkl})_1 / (I_{hkl})_2}{t_1 / t_2} = \frac{[F_e(\theta)_1]^2}{[F_e(\theta)_2]^2} \cdot \frac{e^{-2D_1}}{e^{-2D_2}} \cdot \frac{d_1^2 P_1}{d_2^2 P_2} \cdot \frac{v_2^2}{v_1^2}$$

2.26

If the conditions are those of the dynamical theory, Equation 2.23 can be written from Equation 2.25, and becomes:-

$$\frac{(I_{hkl})_1 / (I_{hkl})_2}{t_1 / t_2} = \frac{F_e(\theta)_1}{F_e(\theta)_2} \cdot \frac{e^{-D_1}}{e^{-D_2}} \cdot \frac{d_1^2 P_1}{d_2^2 P_2} \cdot \frac{v_2}{v_1} \cdot \frac{\epsilon_2}{\epsilon_1}$$

2.27

Where the subscripts 1 and 2 now stand for the materials 1 and 2 respectively in a two component sandwich.

Equations 2.26 and 2.27 can be written in the following form:-

$$\frac{(I_{hkl})_1 / (I_{hkl})_2}{t_1 / t_2} \cdot \frac{d_2^2 P_2}{d_1^2 P_1} = \left[\frac{F_e(\theta)_1 . e^{-D_1} . v_2}{F_e(\theta)_2 . e^{-D_2} . v_1}\right]^n \cdot \left(\frac{\epsilon_2}{\epsilon_1}\right)^{2-n}$$

2.28.

when

n = 1 the dynamical expression would be obtained, and

n = 2 the kinematical expression would be obtained.

In a special case, when the two laminae in a sandwich specimen have approximately the same crystallite size, then a logarithmic plot of

$$\frac{(I_{hkl})_1 / (I_{hkl})_2}{t_1 / t_2} \cdot \frac{d_2^2 P_2}{d_1^2 P_1} \text{ versus } \left(\frac{F_e(\theta)_1 . e^{-D_1} . v_2}{F_e(\theta)_2 . e^{-D_2} . v_1}\right)$$

should, therefore, produce a straight line whose slope is equal to the value of n which determines whether a given sandwich specimen diffracted according to the kinematic or dynamic theory of electron diffraction. Clearly, if one could be sure which theory operates, then it is possible to use Equations 2.26 and 2.27 to deduce the thickness ratio from the measurement of the relative integrated intensity ratio.

However, these are very special conditions, since it has also been assumed that the extinction distances for I_1 and I_2 are such that the kinematical (or the dynamical theory) is applicable to both maxima. Equation 2.28 is, therefore, only of limited value to these experimental analysis which follow. It is much better to consider Equations 2.26 and 2.27 as two special cases, with other possible cases regarding $(I_{hkl})_1$, being kinematical and $(I_{hkl})_2$ being dynamical (or vice versa) according to the thickness or crystallite size.

CHAPTER THREE

EXPERIMENTAL PROCEDURES.

3.1 Evaporation techniques.

Various thicknesses of α-iron, copper, silver and aluminium films were vacuum-evaporated onto carbon-coated electron microscope grids. The amorphous carbon supporting substrate was extremely thin ($\simeq$ 5nm). Facilities were provided for making a sharp step on a clean microscrope slide for film thickness measurement purpose.

Several thicknesses of aluminium film without a supporting substrate onto microscope grids and an aluminium film on different thicknesses of amorphous carbon substrate were also evaporated.

Films of several thickness combinations of α-iron and copper, as composite specimens, were prepared by two stages vacuum-evaporation onto carbon-coated electron microscope grids.

3.1.1 The preparation of carbon-coated electron microscope grids.

The amorphous carbon films were vacuum-evaporated on a sheet of mica for specimen supports. The vapour source consisted of two pointed carbon rods of 0.5cm diameter with the points held lightly together by a tungsten

tension spring, so that an intense local hot spot would be established in the region of contact. A pencil sharpener was used to make the carbon rods sharply pointed. A drop of oil on a piece of white ceramic was used, as an indicator for evaporation. An alternating current of around 40A was applied for evaporation and the vacuum pressure was maintained at 10^{-5}torr through the evaporation.

After the evaporation was completed, air was let into the bell jar of the vacuum system and the carbon-coated mica was then removed.

Facilities for transferring the carbon film onto the electron microscope grids, were provided which consisted of a clean distilled water dish with a turning valve beneath the dish. A piece of metal guaze was located in the middle of the dish so that the electron microscope grids could rest on it.

The carbon film was released by slowly immersing the mica at an angle, with the carbon film on the top, into the distilled water until it was completely submerged. The floating carbon film could be seen by using an ordinary table lamp. The electron microscope grids were carefully situated on the metal guaze without disturbing the carbon film. By stirring the water very slowly, it was possible to bring the floating carbon film onto the top of the metal guaze, and the water was then allowed

to flow out by turning the valve beneath the dish. When the carbon film was laid over the grids, they were then allowed to dry for a few hours. An optical microscope was used to ensure the presence of the carbon film on each grid.

It was found experimentally that when the thickness of the carbon film exceeds about 10nm, it was difficult to release the film from the mica. However, if thicker carbon substrates are required, such as for examining the effect of carbon substrate on the contrast, then successive vacuum-evaporation of carbon onto carbon-coated electron microscope grids may be used.

3.1.2 The specimen preparation.

Single and composite polycrystalline specimens of various materials with wide range of film thicknesses were required. The specimens were prepared by vacuum-evaporation from a "V" shaped tungsten filament onto carbon-coated electron microscope grids. The approximate mass (m) of the metal of density (ρ), needed to deposit a certain thickness (t), at a distance (ℓ') from the filament, was calculated by assuming a spherical evaporation from a point source. This can be described by the following equation:-

$$t = \frac{m}{4\pi\rho(\ell')^2} \qquad 3.1$$

It is clear from Equation 3.1 that the required

approximate film thickness can be obtained by varying the mass of the metal and the distance of the target from the filament.

It was necessary to use different filaments for each evaporation to avoid contamination from any residual metal which had been left on the filament from the previous evaporation.

Several film thicknesses were obtained from the same evaporation, at the same time, by placing the grids on a type of ladder (as shown in Figure 3.1) with movable steps so that one could position the steps in such a way that an unobstructed path from the filament to the grids on the steps would be ensured. Also, according to Equation 3.1, the grids at the greatest distance from the filament, would have a thinner film deposited on them.

Arrangements were also made to produce single and composite polycrystalline metal films of copper and α-iron. In order to provide a thickness measurement of the deposited film, clean microscope slides were placed on each of the five steps of the ladder. It was necessary to have a very definite step to the edge of the film on the microscope slide and to achieve this, a razor blade was placed on each slide and the whole assembly was supported by a "crocodile clip", to prevent the slide moving due to the vibrations caused by the

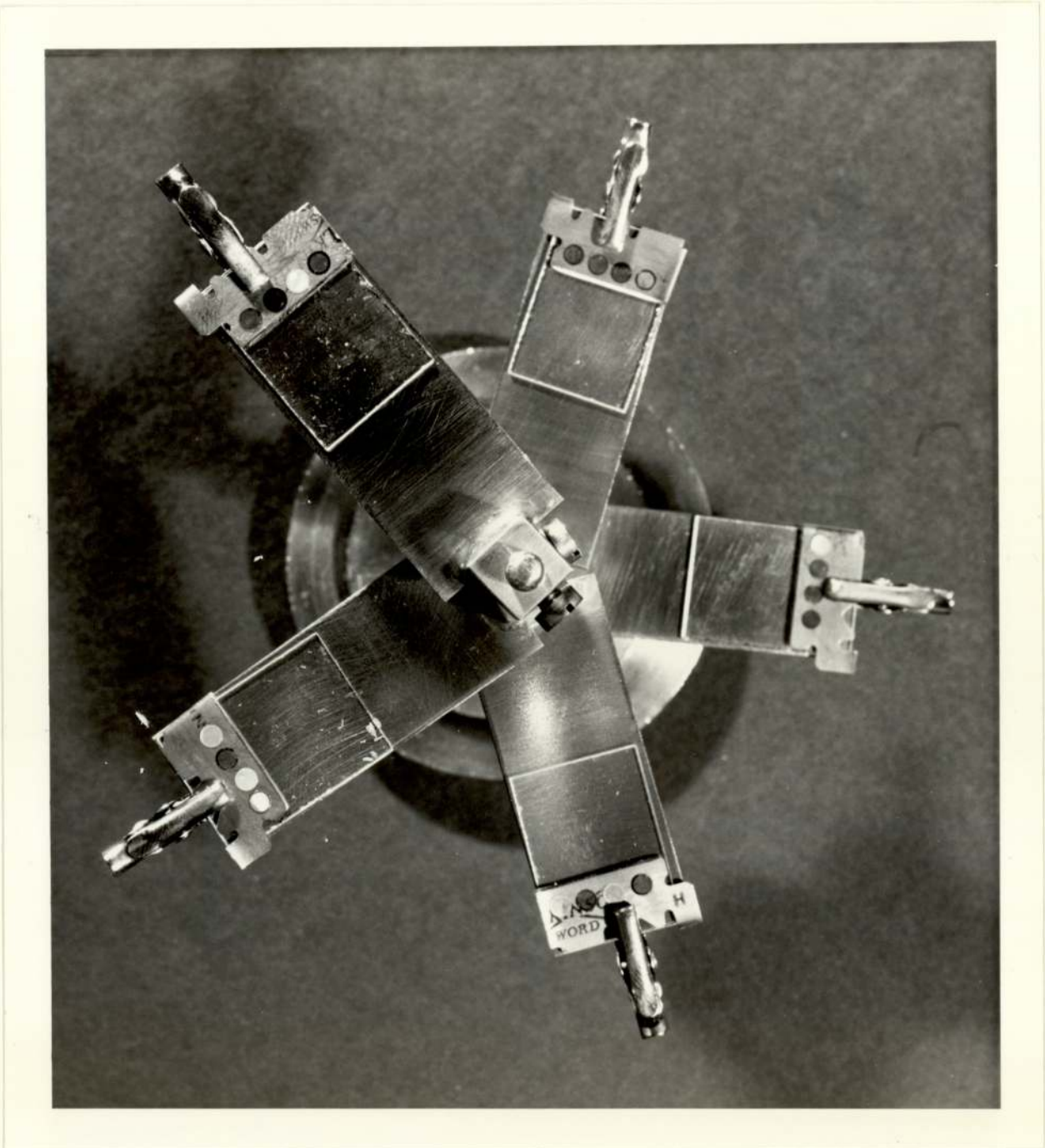

Fig.3.1 Specimens holder for vacuum evaporation.

vacuum backing pump. A tungsten filament, wound with a known mass of thin copper wire, was screwed into the heating terminals of the evaporator. The distances between the filament and the steps were also measured. Six carbon-coated electron microscope grids were placed carefully on each step of the ladder, as shown in Figure 3.1. The cleaned bell jar, which was used as an evacuated chamber, was placed over the evaporator. The rotary and diffusion pumps were switched on according to the instructions and the system was left until a vacuum of 10^{-5} torr was attained. The copper wire was evaporated from the tungsten filament by increasing the heater current rapidly until a hot white filament was observed, which was enough to melt the wire and form a droplet at the base of the "V" shape filament. The current was then quickly decreased to prevent sputtering of the metal. The current was then increased slowly until the filament was white hot. As soon as the droplet had completely evaporated, the heater current was switched off.

After the first evaporation of the copper was completed, the baffle valve was closed and the air was let into the bell jar, which was then removed and its inside wall was polished. Five specimens, one from each step were collected and kept in a special grids box as a single copper specimen. The copper-coated microscope slides were labelled and replaced by new ones. The position of the remaining copper-coated grids were changed so

that sandwiches of various thickness combinations would be obtained. One blank carbon-coated grid was also placed on each step so that a single α-iron specimen could be obtained. A new filament, wound with a known mass of α-iron, was replaced.

The procedure for α-iron evaporation was almost the same as the previous one. After the second evaporation was completed, the specimens were kept in the grids box, each being labelled so that the different specimens could be identified. In this way, twenty five sandwich specimens of different thickness combinations and ten single specimens of different thicknesses from copper and α-iron were prepared.

The specimens which had been prepared, were placed in a grids box, each one being labelled so that the different specimens could be identified.

The microscope slides were then overlaid, by vacuum-evaporation, with an aluminium film of about 100 nm thick for thickness measurement purpose.

The same evaporation technique was used in preparing the single specimens from silver and aluminium of different thicknesses.

3.2 Electron microscopy.

Diffraction patterns for all the specimens at different

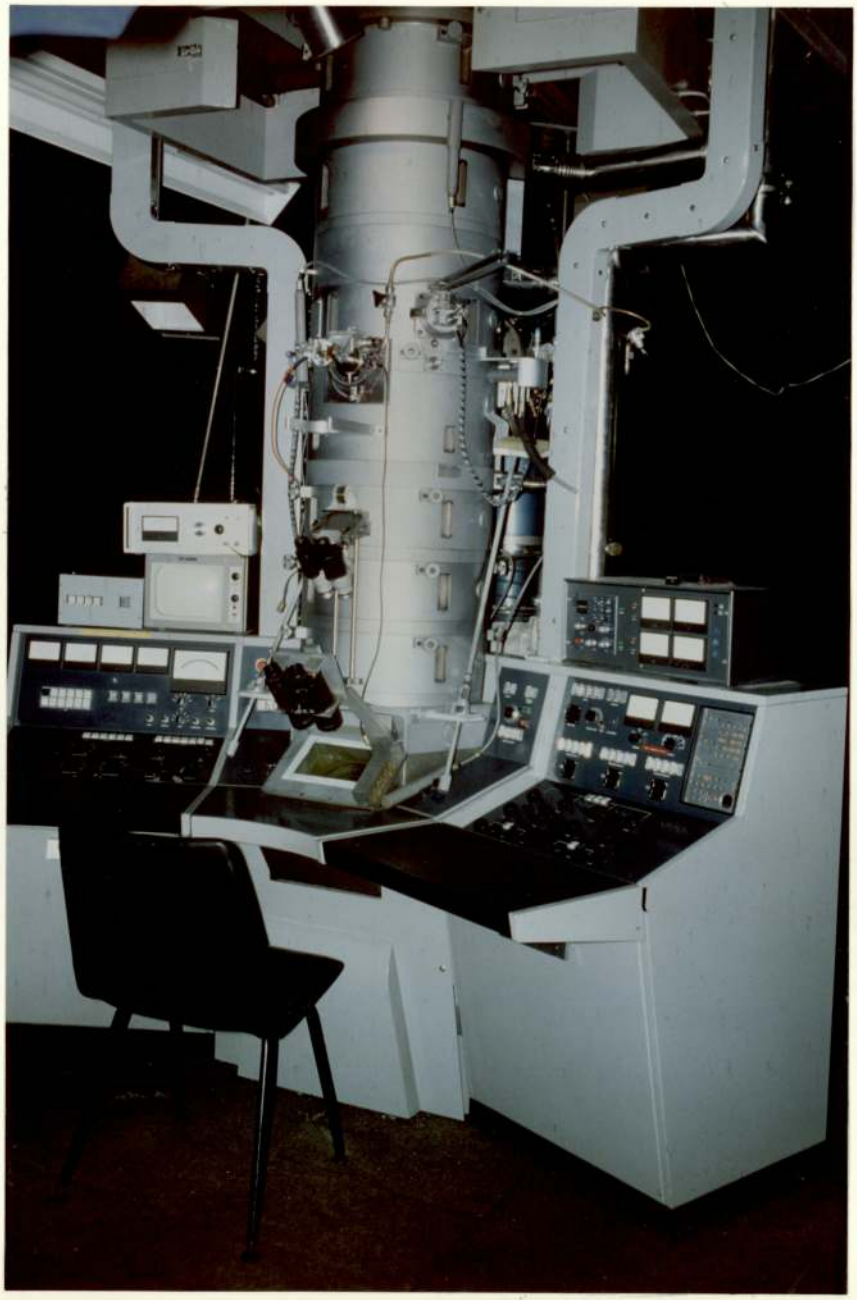

Fig.3.2 An EM7 electron microscope.

accelerating voltages, up to 1000kV, were obtained by using an EM7 microscope as shown in Figure 3.2. Diffraction experiments were carried out using, a selected area diffraction technique, in which a uniform unbroken area of the specimen was selected.

Because the investigations were concerned with the crystallite size of the specimen, an EM200 microscope was used at 100kV to produce a dark field image for crystallite size measurement purpose. In this technique only one diffracted beam from a selected area of the specimen was allowed to contribute to the final image.

3.2.1 Selected area electron diffraction technique.

It is well known that the usual way of using an electron microscope to produce a diffraction pattern is through Selected Area Diffraction. In this method, a fine, parallel beam of electrons is incident on the specimen S as shown in Figure 3.3. On emerging from the specimen, the diffracted beam and the transmitted beam are focused in the back focal plane, D, of the objective lens O. If the specimen consists of randomly-oriented crystallites, which was the case in our experiment, then the diffraction pattern in the back focal plane would consist of a number of concentric rings of uniform intensity. It can be seen also that the transmitted and diffracted electrons from the same area of the specimen meet to form an intermediate image in front of the intermediate lens (first projector lens).

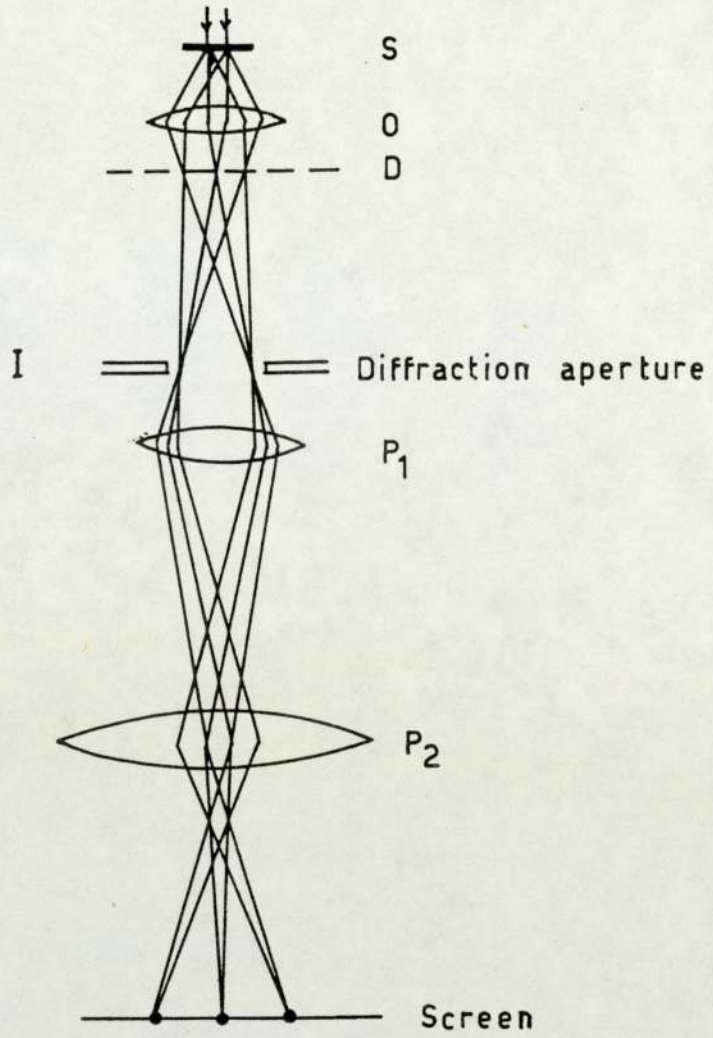

Fig.3.3 Ray diagram (electron diffraction)

While the transmission picture is on the screen, the diffraction aperture is inserted into the plane of the intermediate image, I, so that the only electrons which can reach the screen are those which have already passed through the aperture at I. Consequently, the diffraction pattern obtained by this technique is that produced from an area of the intermediate image, exactly equal to the area of the aperture. This diffraction pattern which has formed in the back focal plane of the objective lens, can then be magnified and projected onto the screen.

The pattern may be sharpened by underfocusing the second condenser lens.

There are two major sources of errors to be considered when taking a selected area diffraction pattern. These are (i) spherical aberration due to the lenses and (ii) incorrect focusing of the objective lens. The best way to minimize the effects of spherical aberration is to use a small diffraction aperture ($\simeq$ 50 u), but unfortunately this sometimes produces spotty diffraction patterns, because there are not enough crystallites in the area under examination. In this case, a bigger aperture is recommended. The second source of error could be overcome by varying the current in the first projector lens and the current in the objective lens to ensure that the intermediate image is formed in the plane of the diffraction aperture. In other words, the inner edge of the aperture and the image of the specimen inside the aperture must be sharply focussed on the screen before turning to the diffraction mode.

Photographs of the diffraction patterns from all the specimens were taken, with exposure times applicable to the brightness of the pattern. Figure 3.4 shows samples of the diffraction patterns of copper, α-iron and their combination specimens.

∝-Fe

Cu

∝-Fe + Cu

Fig.3.4 Diffraction patterns from single and composite polycrystalline metal films of copper and ∝-iron specimens.

3.2.2 Dark field microscopy with selected diffracted beams.

Dark field techniques were used to measure the crystallite size of each specimen. An EM200 microscope was used with an accelerating voltage of 100 kV in 'the selected area diffraction mode of operation' to produce a diffraction pattern for each specimen. A small objective aperture was then inserted and the beam was tilted until a part of the strongest diffraction ring came into view through the objective aperture. The microscope was then switched back in the normal manner, and an image of bright crystals in a dark field was formed. Samples of photographs taken under dark-field conditions are shown in Figure 3.5. Many images of crystallite in each photograph, were measured with the aid of a graph paper and a viewer. The average value of the crystallite size was obtained after allowance of magnification had been taken into account.

3.3. Microdensitometry.

In order to determine the diffraction ring intensity in the diffraction pattern, a measurement of the density of blackening of the photographic plate had to be obtained. The density variations were measured with an Automatic Recording Microdensitometer, in which the intensity of light passing through the micrograph was compared with that passing through a standard glass wedge (along which the density of blackening varied from minimum to maximum with a known gradient).

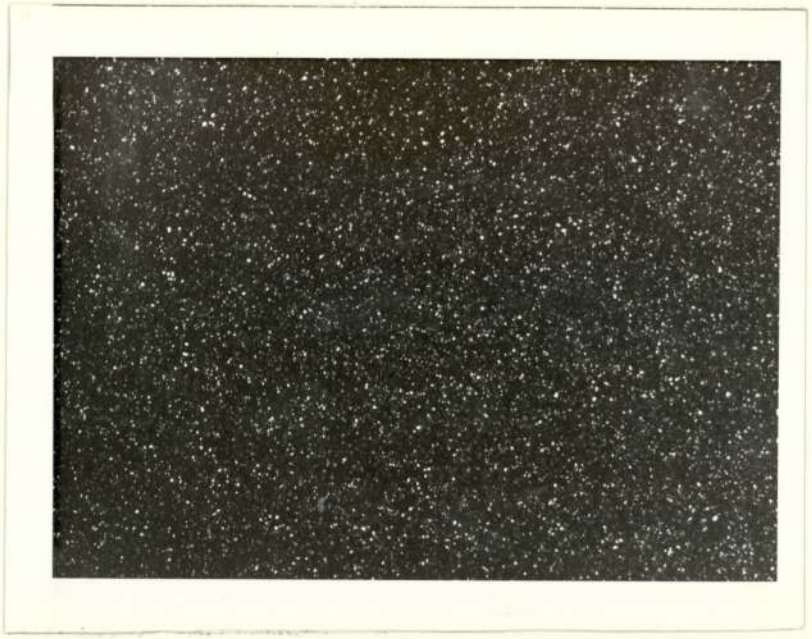

∝-iron

copper

Fig.3.5 Samples from darkfield photographs.

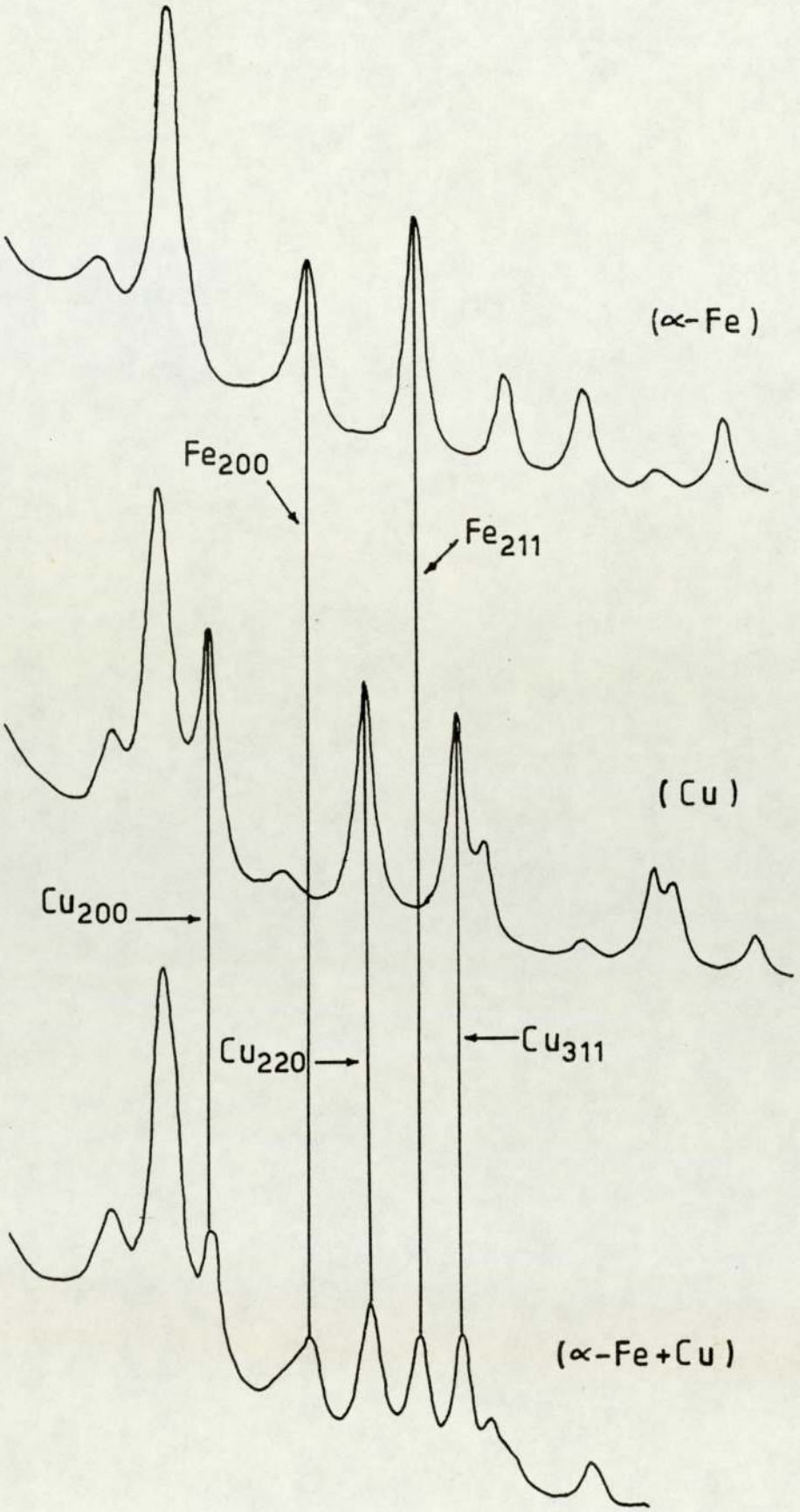

Fig. 3.6 Typical microdensitometer traces of α-iron, copper and their combination.

The microdensitometer trace, across the rings in the pattern, showed the diffraction rings as peaks on a rising background. The zero level of the density of blackening was traced from an unexposed area in the micrograph called "clear plate" area so that a reference would be made to measure the density of blackening in terms of centimeters.

Typical microdensitometer traces are shown in Figure 3.6.

3.4 Measurement of diffraction intensity.

The diffraction intensity was determined experimentally by photographic method in which the intensity was determined as a function of the blackening. The relationship between the intensity of an electron beam, falling on a given photographic plate and the magnitude of blackening caused by this beam, had to be obtained. This was done by constructing a calibration curve relating the density of blackening to the exposure dose, the latter quantity being proportional to the product of intensity and the exposure time for which the photographic plate was exposed to the electrons. In the following sections, the method of constructing the calibration curve and the way of measuring the relative integrated intensity are explained.

3.4.1 Calibration of the photographic plates.

It is well known that the response of a photographic plate to the incident electron intensity is non linear(20).

Therefore, the integrated intensities formed by the electron beams are not directly proportional to the densities of blackening in the micrograph, but are proportional to the exposure dose. In this situation a calibration curve relating density of blackening to the exposure dose is essential.

A calibration curve was constructed for each batch of photographic plates by taking four photographs of one specimen using a range of exposure times. Microdensitometer traces of these micrographs were taken, and a smooth background curve was drawn below the diffraction maxima on the microdensitometer trace of each micrograph.

The height of the peak point and the background point from the clear plate line were measured for a number of peaks in each trace (see Figure 3.7) and converted into units of density of blackening (D_a) and (D_b) respectively by multiplying these heights with the gradient of the glass wedge. These values were plotted against the exposure time in logarithmic graph paper.

The plot was similar to that shown in Figure 3.8a.

A similar transparent graph paper was superimposed on the previous plot, and by moving it toward the x-direction, the converted points combined to give the resultant calibration curve of the density of blackening versus the exposure dose as illustrated in Figure 3.8b.

The calibration curves were constructed and used in the relative integrated intensity measurements.

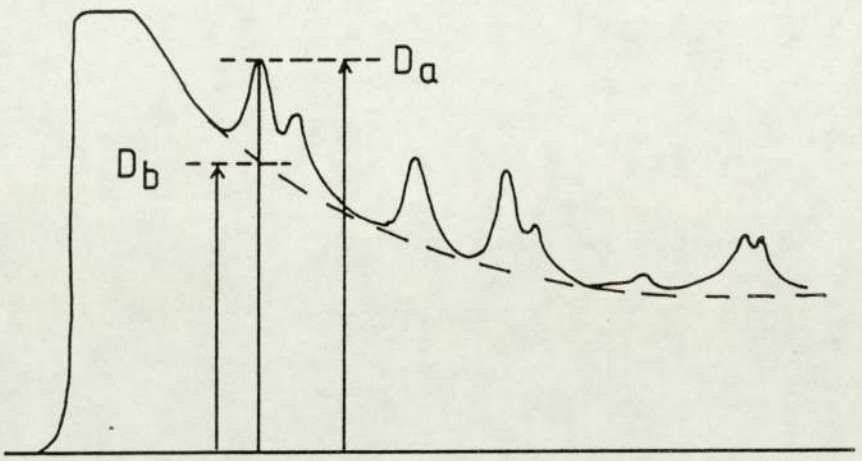

Fig. 3.7 Evaluation of photographic blackening.

3.4.2 Relative integrated intensity.

The relative integrated intensities of the diffraction maxima were measured from their microdensitometer traces in the following manner.

A general background curve was drawn under the peaks together with lines parallel to the ordinate axis through the maximum points of the peaks. The density of blacken-

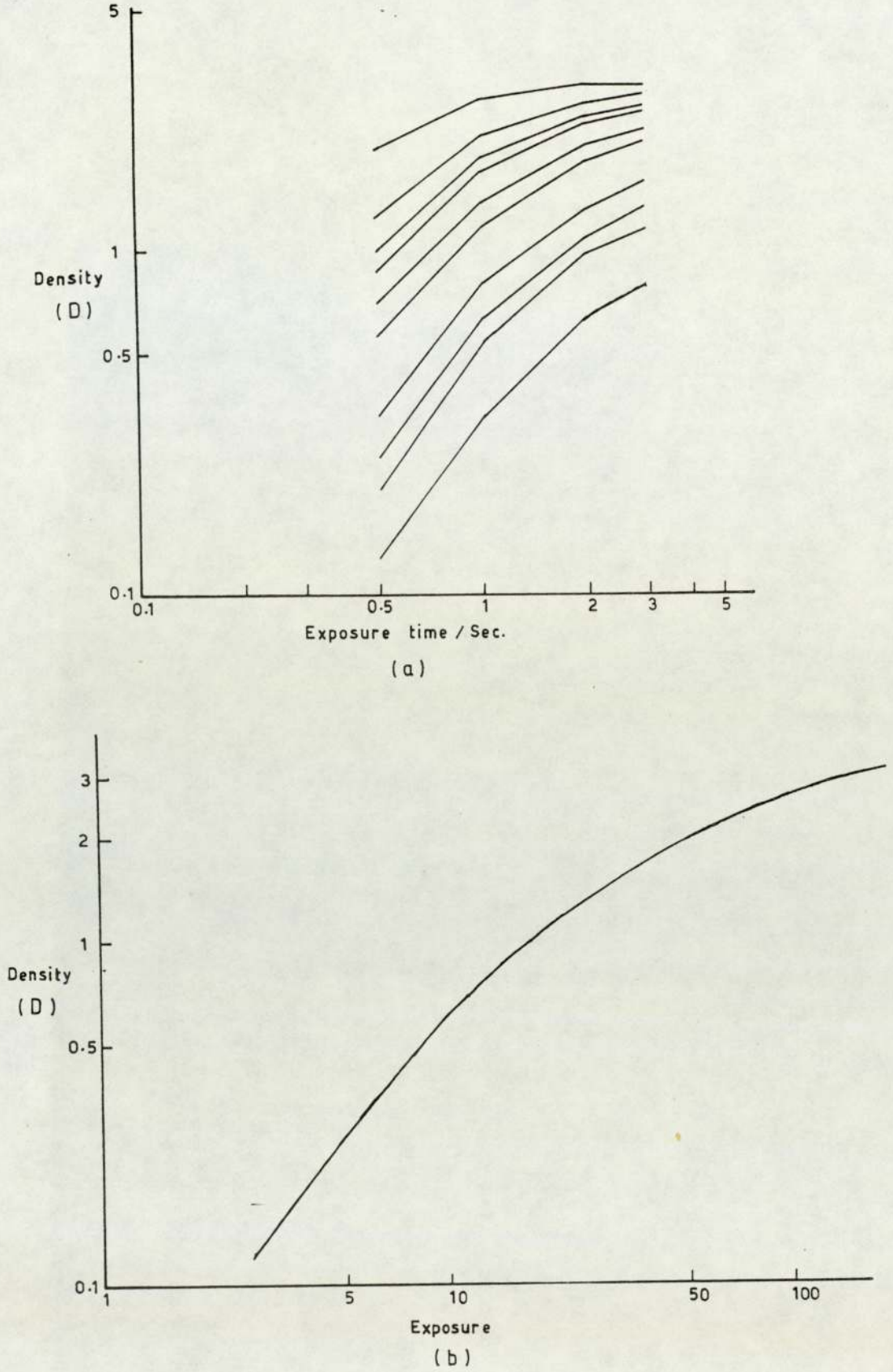

Fig. 3.8 Construction of a calibration curve.

ing of the peak (D_a) and the background (D_b) for all possible peaks were measured and their corresponding exposures (Σ_a) and (Σ_b) were found by using the calibration curve. The half-peak point was found by taking the mean value of these two exposures and converting it back into density of blackening units, and then into height on the microdensitometer trace. A line parallel to the background curve was drawn through the half-peak point. A right-angled triangle was constructed beneath this line, to be used as a hypotenuse, and the other two sides would be parallel to the x and y axes. The base of the triangle (w), which was the width at the half-peak point, was measured as shown in Figure 3.9.

The relative integrated intensity, which was equivalent to the area under the peak, taken as the product of the half-peak width and the exposure dose of the peak above the background. The relative integrated intensity (R.I.I.) was then given by:-

$$R.I.I. = w(\Sigma_a - \Sigma_b) \qquad 3.2$$

This assumes that all the peaks have the usual Gaussian profile.

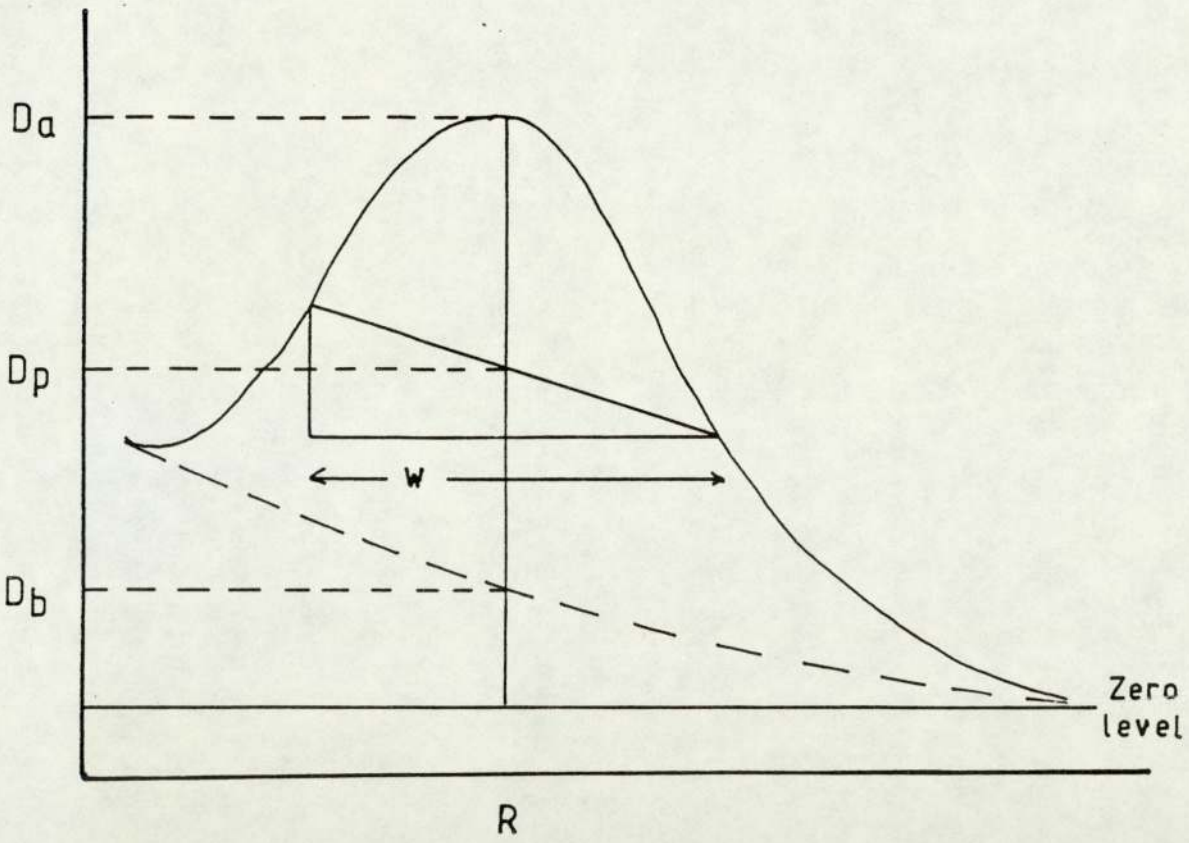

Fig. 3.9 Method of measuring the relative integrated intensity.

3.5 Film thickness measurement.

A multiple beam interferometer was used to measure the thickness of the film which has been deposited on the microscope slide. In this technique, the edge of the film which was to be measured, was overlaid with about 100nm of a highly reflecting material, such as aluminium. A step was formed over the edge of the film and it was independent of the thickness of the overlay. A semi-reflecting optical flat surface, which was situated on the specimen table of the interferometer, was placed over the step and an air gap was formed between the surfaces as shown in Figure 3.10a.

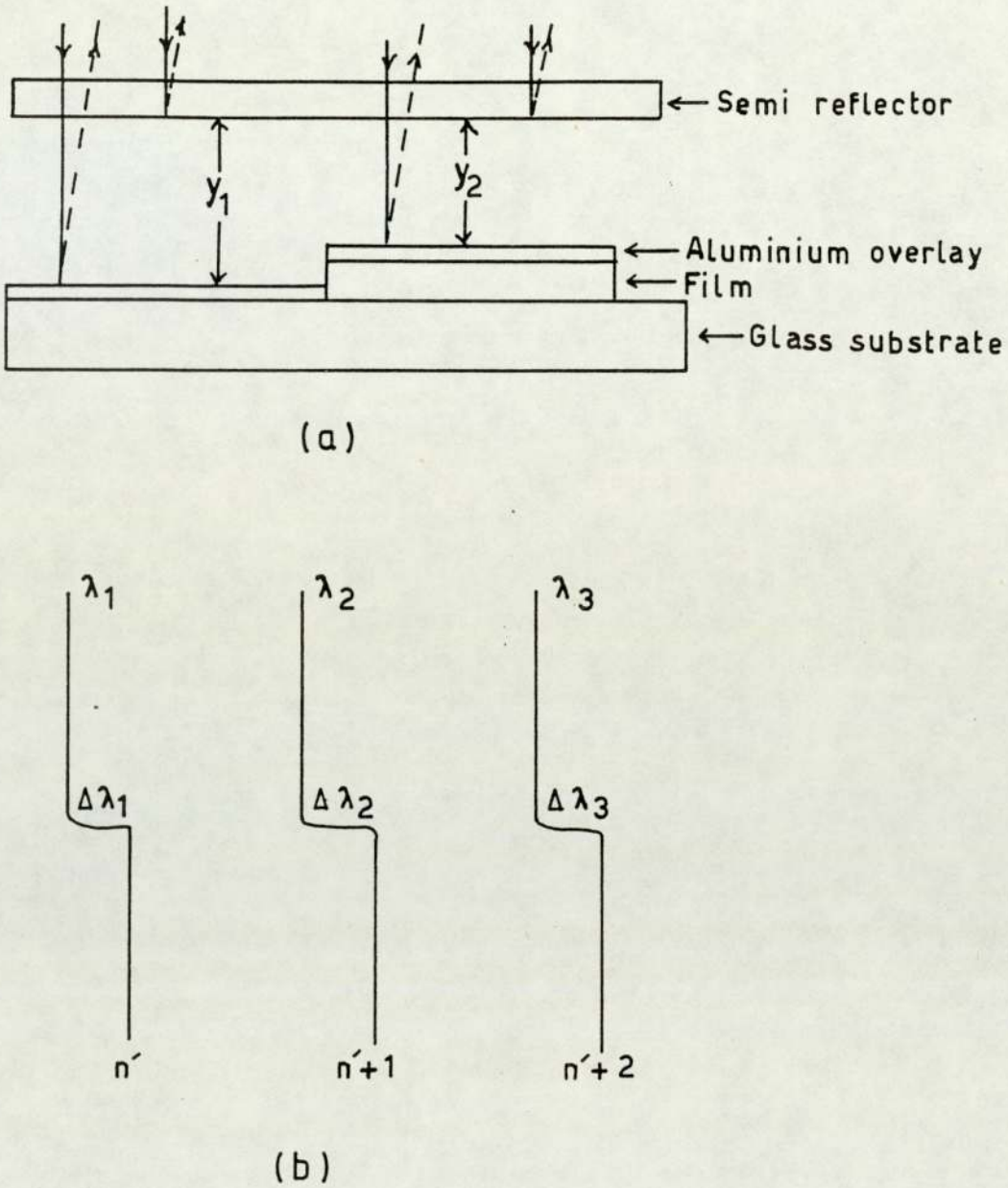

Fig. 3.10 Film thickness measurement.

Then a beam of white light was incident onto the system and interference took place between the light reflected from either side of the step and the semi-reflecting surface. If the air gap thickness is a multiple of $(\lambda/2)$, where λ is the wavelength of light, then a destructive interference takes place for that particular wavelength (21), and dark fringes will appear in the field of view.

The fringes produced are of equal chromatic order and seen to have a "kink" due to the discontinuity in the air gap caused by the step as shown in Figure 3.10b.

The order for each fringe, from red to violet, have an upward trend and differ by unity. The fringe at wavelength λ_1, has an order n' given by the following equation:-

$$y_1 = n'(\lambda_1/2) \qquad 3.3$$

$$2y_1 = n'\lambda_1 \qquad 3.4$$

Similarly the order corresponding to a fringe at λ_2 should be $(n'+1)$, Then:-

$$2y_1 = (n'+1)\,\lambda_2 \qquad 3.5$$

$$n' = \lambda_2/(\lambda_1-\lambda_2) \qquad 3.6$$

In the same way the order of the other fringes can be determined.

The displacement of the fringe formed at λ_1 has the same order n', but interference corresponds to a wave-

length ($\lambda_1 - \Delta\lambda_1$) which was caused by the interference in the gap y_2, and since the film thickness t was equal to $y_1 - y_2$, then it can be shown that

$$2y_2 = n'(\lambda_1 - \Delta\lambda_1) \qquad 3.7$$

Subtracting Equation 3.7 from Equation 3.4, we get

$$2y_1 - 2y_2 = n'\Delta\lambda_1 \qquad 3.8$$

$$t = \frac{n'\Delta\lambda_1}{2}$$

Following the same method, the film thickness was measured at several wavelengths and the mean value was taken.

CHAPTER FOUR

EXPERIMENTAL RESULTS AND ANALYSIS OF SINGLE AND DOUBLE LAMINA SPECIMENS.

4.1 Single lamina specimens.

Two groups of different film thicknesses from pure copper and ∝-iron specimens were prepared by vacuum evaporation directly onto carbon-coated electron microscope grids. The analysis of each diffraction pattern in terms of relative integrated intensities was carried out by using Equation 2.22.

$$\text{Log}\left[\frac{I_1}{I_2}.\frac{d_2^2\,P_2}{d_1^2\,P_1}\right] = n\ \text{Log}\left[\frac{F_e(\theta)_1.\ e^{-D_1}}{F_e(\theta)_2.\ e^{-D_2}}\right] \qquad 2.22$$

In this Equation (2.22) the subscript 1 relates to the (hkl) of the strongest line which was always (111) in the case of copper and (110) in the case of ∝-iron, and the subscript 2 was for all the other possible (hkl) maxima in the diffraction pattern.

The above equation could be written in the following form:-

$$\text{Log}(J) = n\ \text{Log}(Q) \qquad 4.1$$

$$\text{where } J = \frac{I_1}{I_2}.\frac{d_2^2\,P_2}{d_1^2\,P_1} \quad \text{and} \quad Q = \frac{F_e(\theta)_1.\ e^{-D_1}}{F_e(\theta)_2.\ e^{-D_2}} \qquad 4.2$$

In this analysis the experimental values of Log(J) were plotted against the values of Log(Q) for each pattern. The resultant may be a straight line whose slope has a

value of n, which determines whether the given specimen was diffracted according to the kinematic or dynamic theory. Also the n values for each pair of diffraction maxima were calculated in an attempt to find the variation of these values with their corresponding average Bragg angles $\bar{\theta}$ (in the event that the above plot does not turn out to be a straight line).

4.1.1 Experimental results.

This section presents the basic experimental result of the single copper and α-iron specimens. Five specimens of various film thicknesses from each material were prepared and measured by a Multiple Beam Interferometer (see Section 3.5). Dark field microscopy was used to measure the crystallite size of each of the previous specimens(see Section 3.2.2).

Table 4.1 shows the films thickness (t) of copper and α-iron specimens prepared by vacuum evaporation onto glass microscope slides and their mean crystallite sizes (ϵ). Note the tendency for the crystallite size (ϵ) to decrease with decreasing thickness (t).

Diffraction patterns were obtained using an electron microscope in the selected area electron diffraction mode of operation at different accelerating voltages up to 1000kV, the size of the diffraction aperture being chosen to give rings of uniform intensity.

Table 4.1 Film thickness and mean crystallite size of copper and α-iron specimens.

Copper	t/nm	ϵ/nm	α-iron	t/nm	ϵ/nm
Cu_1	63.7	11.0	Fe_1	90.0	10.7
Cu_2	45.6	9.6	Fe_2	50.0	9.3
Cu_3	36.0	9.0	Fe_3	35.0	9.4
Cu_4	30.0	8.9	Fe_4	23.0	7.9
Cu_5	23.0	8.7	Fe_5	16.7	6.7

Four photographs, at different exposure times, were taken of the diffraction patterns from a selected specimen to enable a calibration curve of 'exposure versus optical density' to be deduced for each batch of used photographic films.

The density variations in each micrograph were measured with an Automatic Recording Microdensitometer (see section 3.3).

The relative integrated intensities of all possible diffraction maxima in each microdensitometer trace were measured as previously explained in section 3.4.2.

The relative integrated intensity ratios of the strongest ring to all other possible diffraction maxima in each micrograph, were calculated as shown in Tables 4.2 and 4.3.

These ratios were then analysed as shown in the next section.

Table 4.2 Relative integrated intensity ratio of copper specimens at different accelerating voltage.

Specimen Copper	Relative integrated intensity ratio $\frac{111}{200}$	$\frac{111}{220}$	$\frac{111}{311}$	$\frac{111}{400}$	$\frac{111}{422}$	Acc. voltage
Cu_1	1.98	2.73	2.65	21.55	12.45	
Cu_2	2.00	2.94	2.65	23.77	12.63	
Cu_3	2.02	2.84	2.85	19.60	14.19	200kV
Cu_4	2.07	2.88	2.75	24.46	16.96	
Cu_5	2.07	2.84	2.97	27.49	14.11	
Cu_1	2.05	3.15	2.86	34.29	22.49	
Cu_2	2.03	3.00	2.77	30.46	20.25	
Cu_3	2.04	2.98	2.69	26.20	16.08	600kV
Cu_4	2.00	2.96	2.76	25.00	14.24	
Cu_5	2.07	2.53	2.87	25.00	16.81	
Cu_1	2.07	3.30	3.41	40.74	26.71	
Cu_2	2.05	3.11	3.24	47.70	27.64	
Cu_3	2.05	3.16	3.21	43.10	30.71	1000kV
Cu_4	2.06	3.03	3.58	48.89	29.41	
Cu_5	2.08	2.96	3.86	47.60	29.80	

Table 4.3 Relative integrated intensity ratio of ∝-iron specimens at different accelerating voltages.

Specimen ∝-iron	Relative integrated intensity ratio $\frac{110}{200}$	$\frac{110}{211}$	$\frac{110}{220}$	$\frac{110}{310}$	$\frac{110}{321}$	Acc. voltage
Fe_1	5.54	2.56	8.74	7.71	8.73	
Fe_2	5.56	2.67	9.98	8.66	10.18	
Fe_3	5.20	2.60	10.52	8.14	9.51	200kV
Fe_4	5.42	2.76	10.78	8.71	10.35	
Fe_5	5.57	3.38	14.47	11.70	13.62	
Fe_1	5.58	2.96	10.37	9.68	10.52	
Fe_2	5.54	2.89	9.74	8.49	9.85	
Fe_3	5.68	3.03	10.96	9.18	10.25	600kV
Fe_4	5.86	3.18	11.21	10.00	12.60	
Fe_5	5.64	3.64	15.90	12.95	14.38	
Fe_1	-	-	-	-	-	
Fe_2	5.56	3.21	11.03	9.98	14.58	
Fe_3	5.65	3.47	12.43	11.77	14.71	1000kV
Fe_4	5.67	3.26	12.22	11.12	14.97	
Fe_5	-	5.40	22.86	17.01	21.05	

4.1.2 Analysis of the diffraction patterns obtained from single specimens.

The preliminary stage of the analysis of the diffraction patterns obtained from single specimens was to determine the relative integrated intensity ratios of the diffraction rings intensities as shown in Tables 4.2 and 4.3. These intensity ratios were then used to determine the n value for each diffraction pattern by plotting the calculated values of Log(J) against Log(Q) of the Equation 2.22. The value of J (see Equation 4.2) included the ratios of both the square of d spacing between the atomic planes and the multiplicity factor P. This quantity could be calculated from Table 4.4 below.

Table 4.4 The interplanar spacing (d) and the multiplicity factor (P) of copper and α-iron.

Copper			α-iron		
hkl	d/nm	P	hkl	d/nm	P
111	0.209	8	110	0.203	12
200	0.181	6	200	0.143	6
220	0.128	12	211	0.117	24
311	0.109	24	220	0.101	12
400	0.090	6	310	0.091	24
422	0.074	24	321	0.077	48

The value of Q included the ratios of both the structure factor ($F_e(\theta)$) and the Deby-Waller factor (e^{-D}). These values were listed in Tables A.1 and B.1 respectively, (see Appendix).

Figures 4.1 to 4.6 are graphs of log(J) versus log(Q) of various film thicknesses of copper and α-iron specimens taken at different accelerating voltages. It was noticed that a straight line could possibly be fitted through the experimental points of each graph. A computer programme "LINEFIT" was arranged to give slope, intercept and correlation coefficient for each plot. The best lines passing through the experimental points were obtained with very high correlation coefficient, of about 0.97, for most of them. This was sufficient indication of the presence of the linear relationship between the experimental points of each graph.

The slope of each graph in the previous figures (4.1 to 4.6) should, therefore, be equal to the value of n.

The obtained values of n for all copper and α-iron specimens at different accelerating voltages are shown in Table 4.5

This table shows that, for 1000kV, $n = 2.02 \pm 0.04$, indicating that despite changes in thickness and material, both maxima obey the kinematical theory. Although the copper specimens showed a tendency for n to be close to unity at 200KV, the remainder of the n values indicate a mixture of both kinematical and dynamical effects. There was a tendency for n to increase with decreasing specimen thickness. Whilst it was interesting to see that straight line graphs were

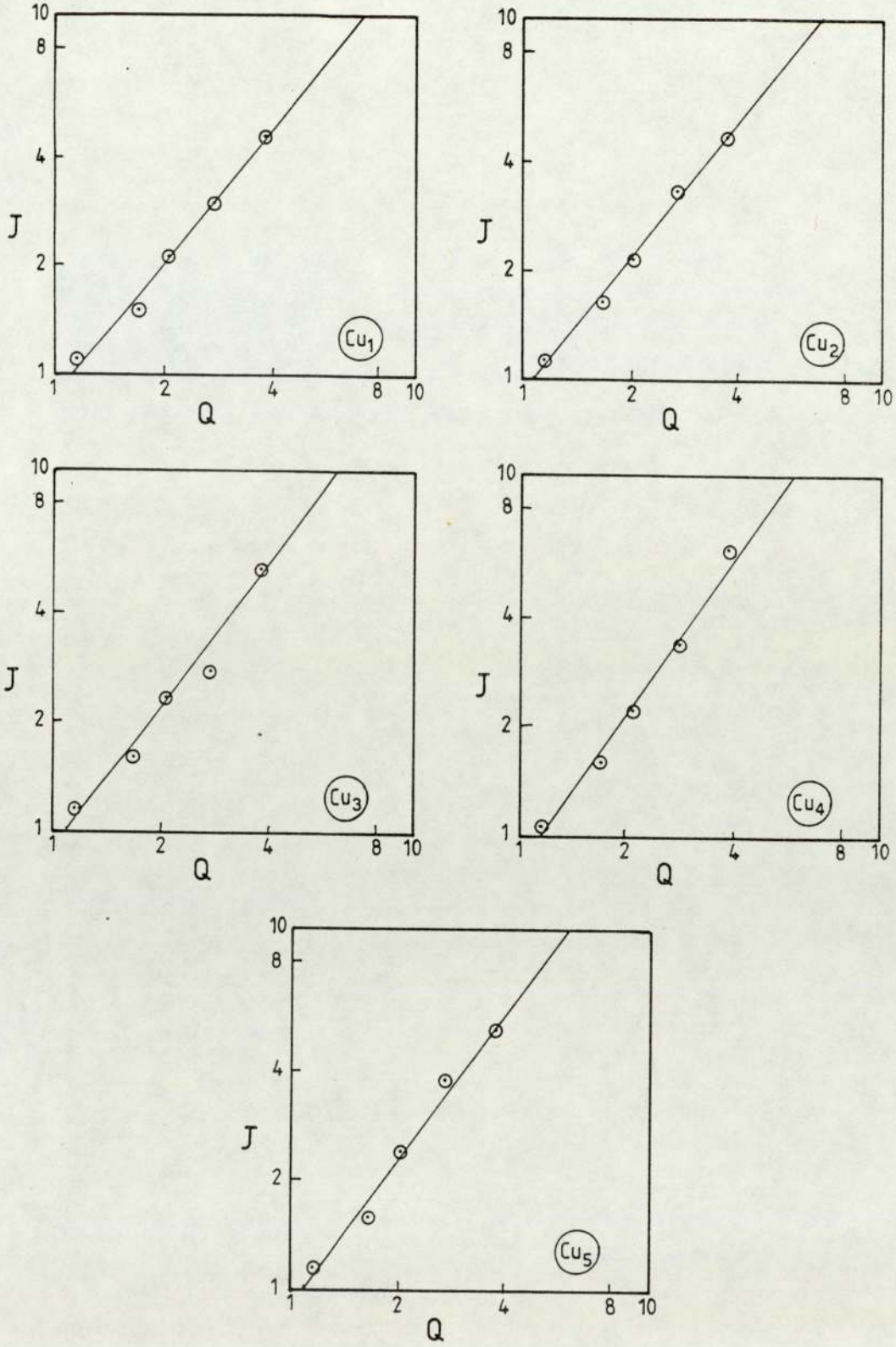

Fig. 4.1 Logarithmic plot of J versus Q for copper specimens at 200kV.

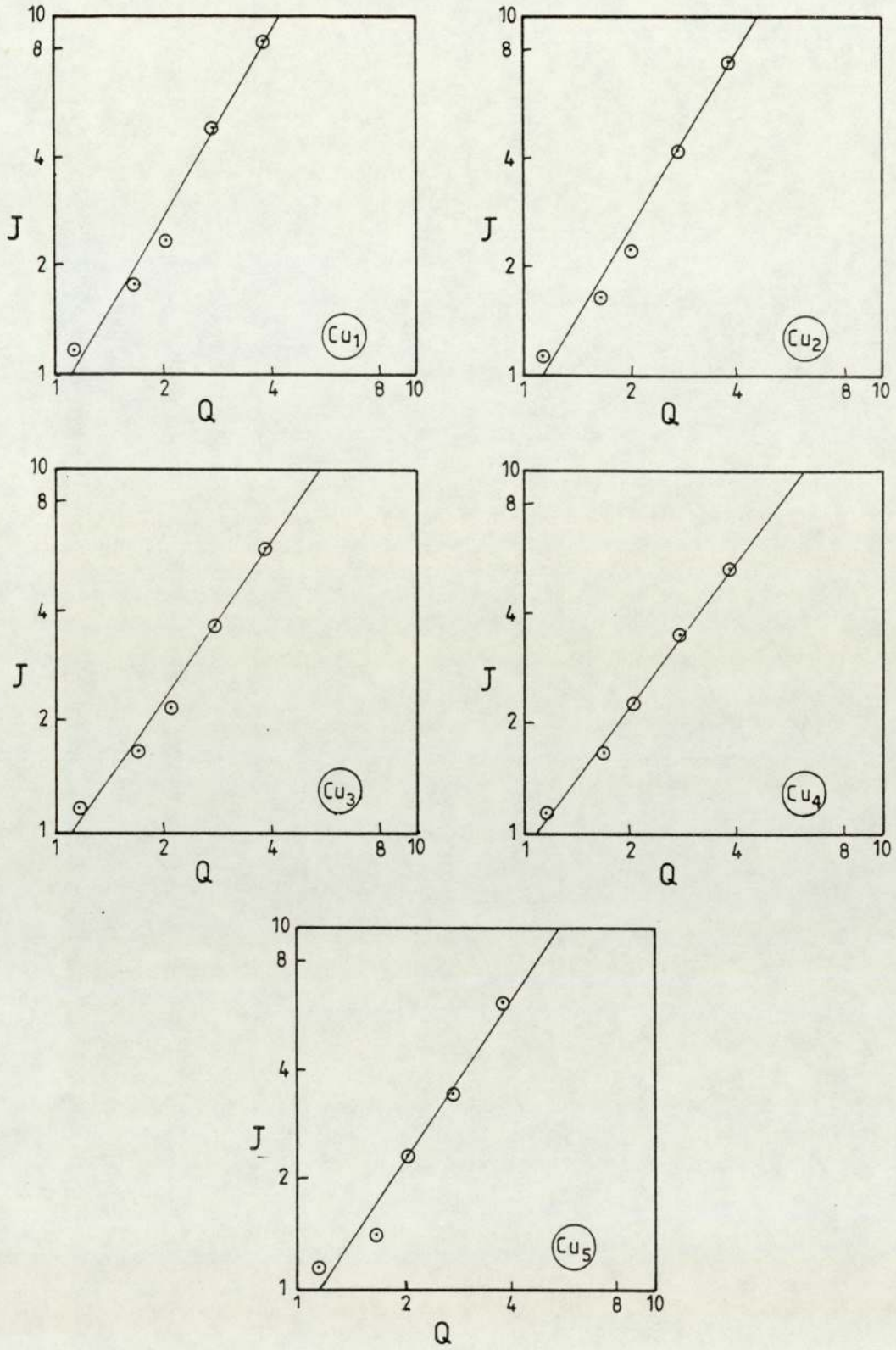

Fig. 4.2 Logarithmic plot of J versus Q for copper specimens at 600kV.

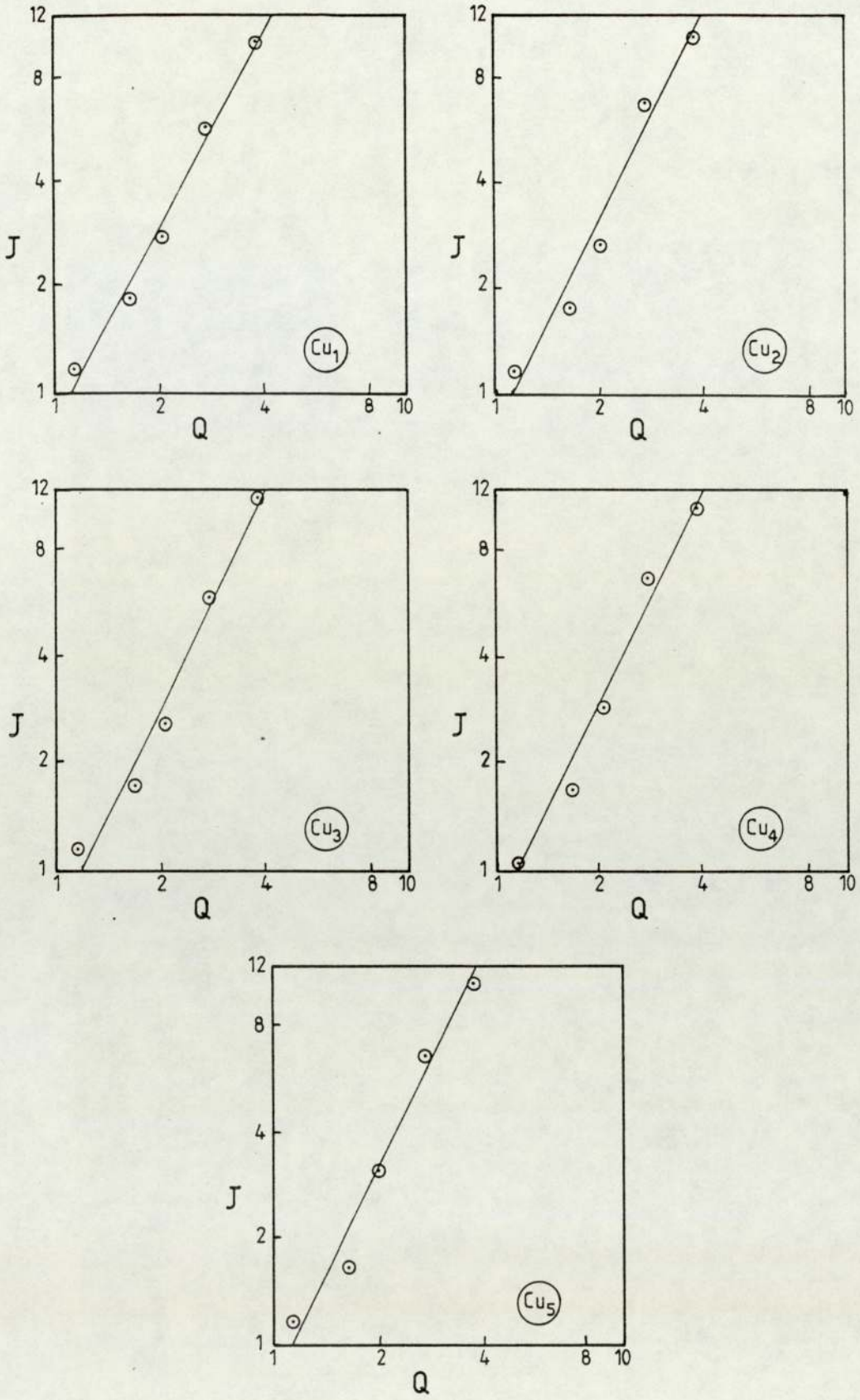

Fig. 4.3 Logarithmic plot of J versus Q for copper specimens at 1000kV.

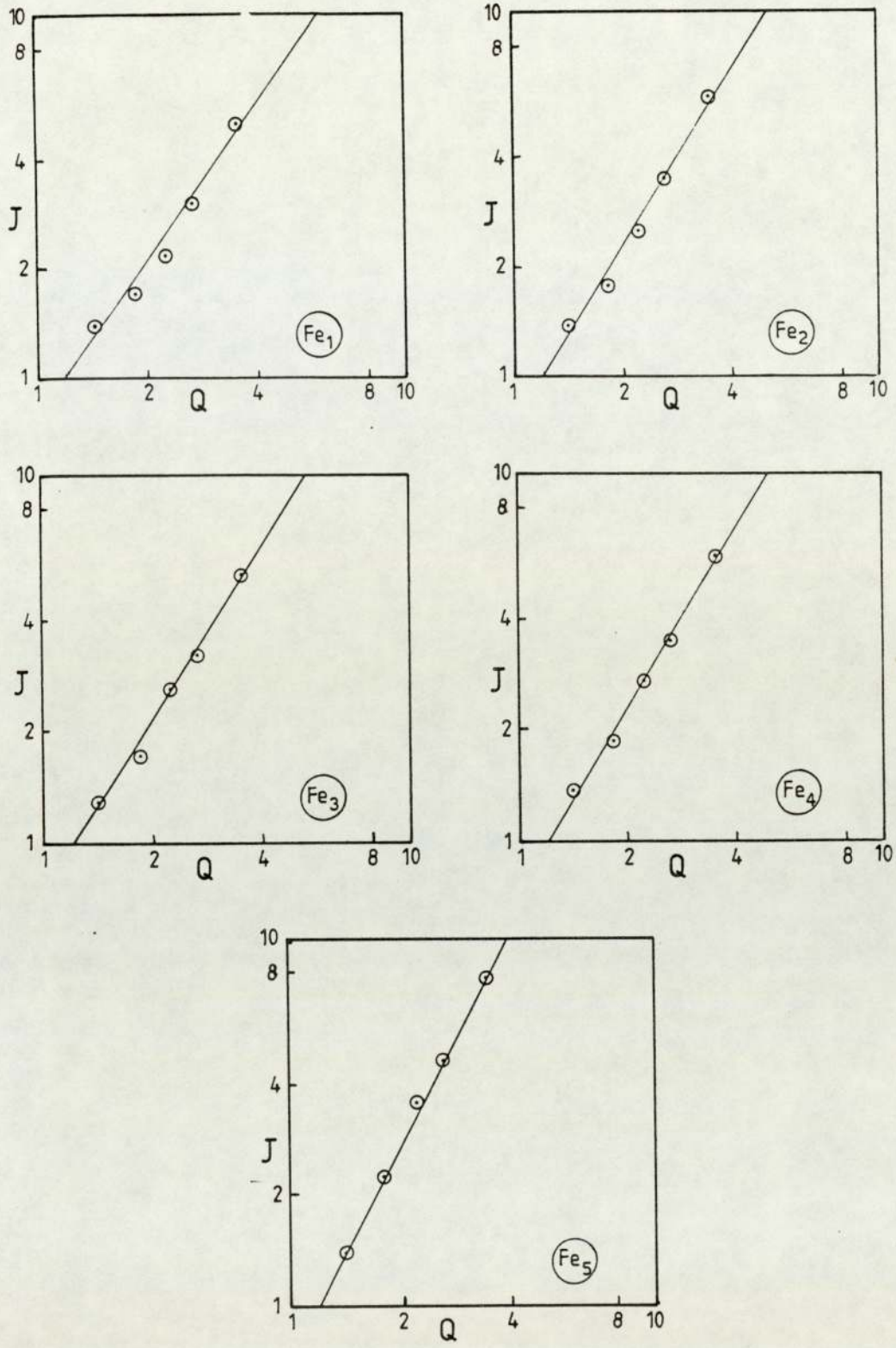

Fig.4.4 Logarithmic plot of J versus Q for α-iron specimens at 200kV.

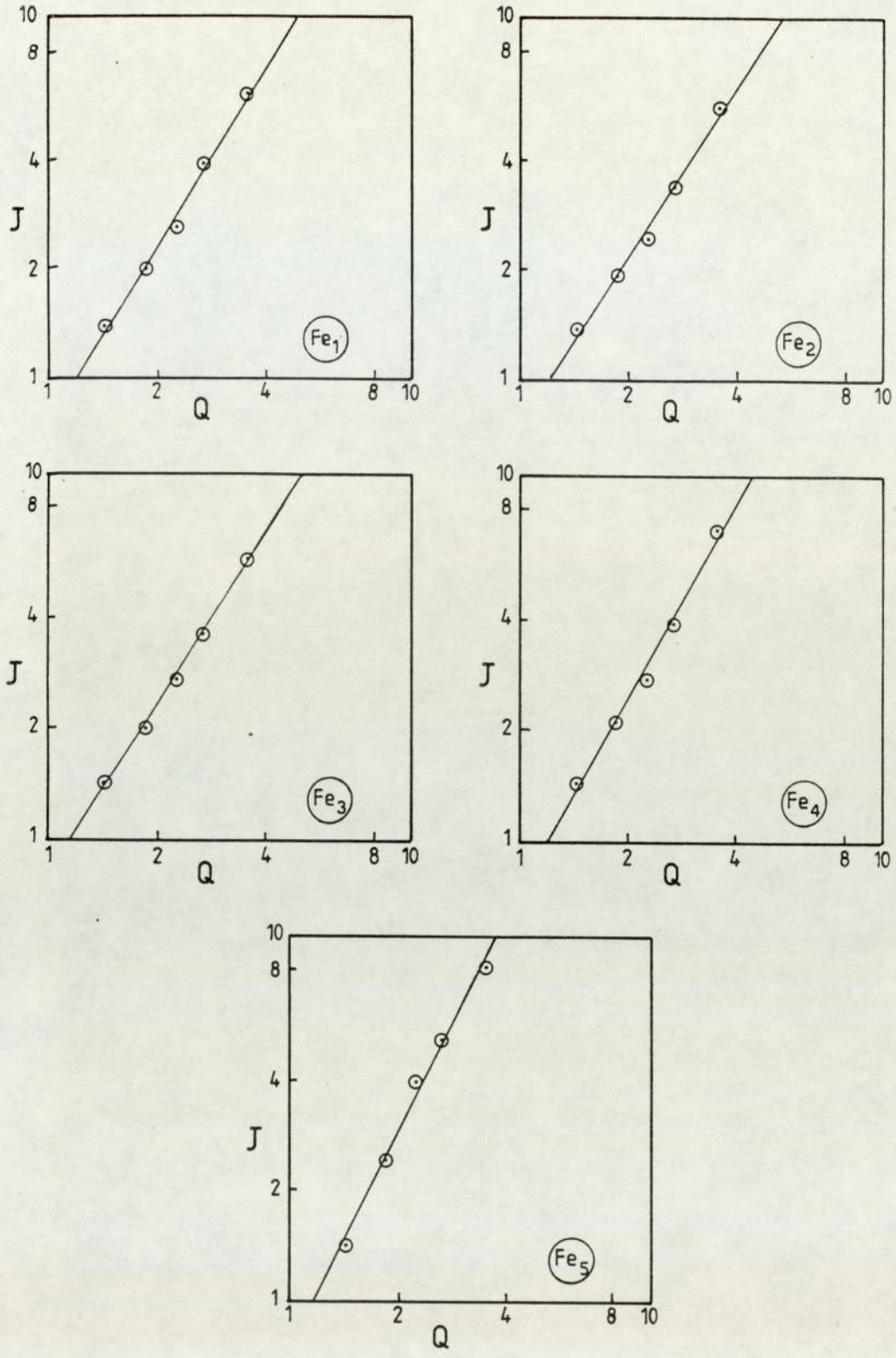

Fig.4.5 Logarithmic plot of J versus Q for ∝-iron specimens at 600kV.

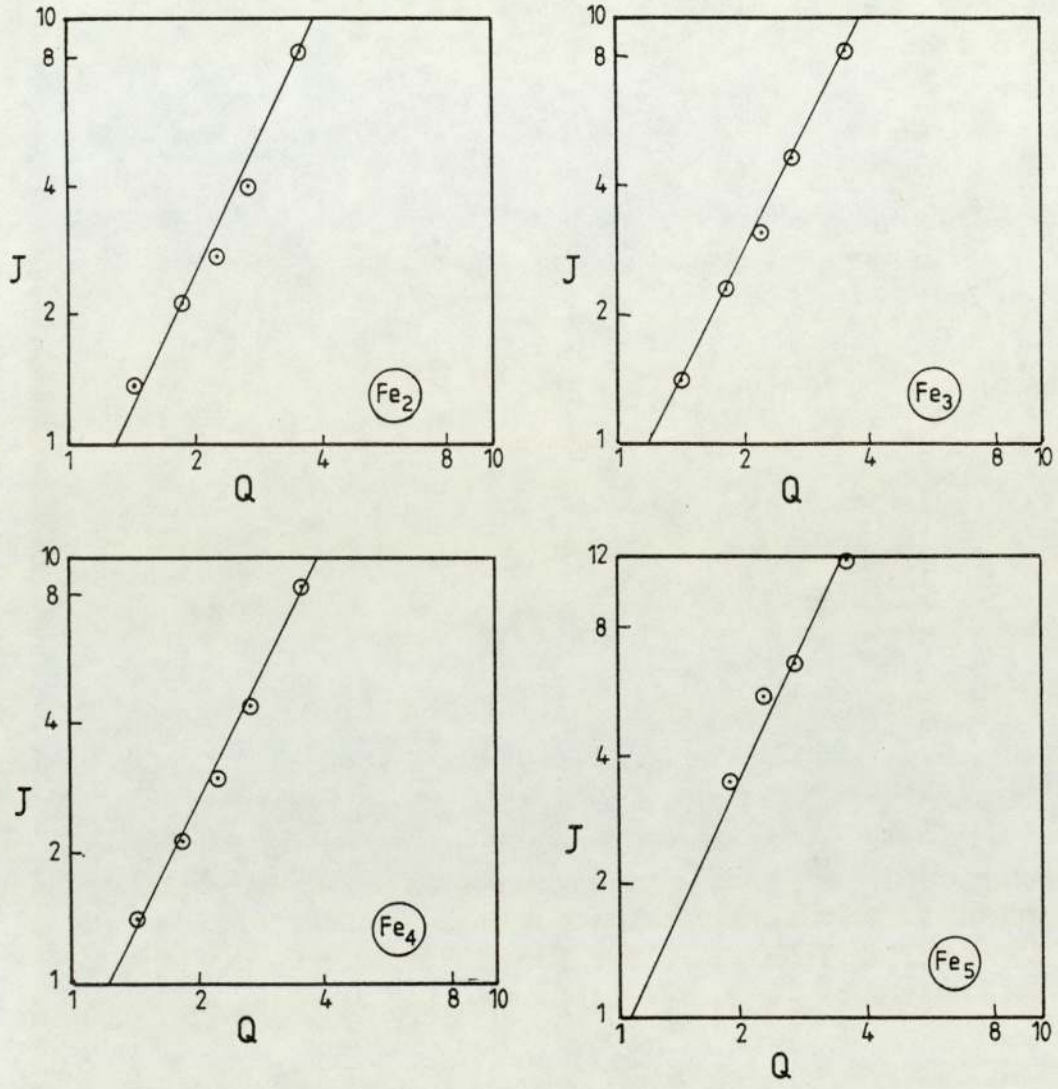

Fig.4.6 Logarithmic plot of J versus Q for α-iron specimens at 1000kV.

Table 4.5 The n values of copper and ∝-iron specimens measured from the Figures 4.1 to 4.6.

Specimen	n		
	200kV	600kV	1000kV
Cu_1	1.23	1.74	1.9
Cu_2	1.25	1.65	2.00
Cu_3	1.27	1.44	2.03
Cu_4	1.45	1.35	2.04
Cu_5	1.36	1.49	2.04
Fe_1	1.45	1.65	-
Fe_2	1.62	1.55	2.1
Fe_3	1.61	1.58	1.97
Fe_4	1.65	1.76	1.99
Fe_5	1.92	1.97	2.13

obtained in Figures 4.1 to 4.6, it is clear that one needs to deduce the n for each pair of rings independently (according to Equation 2.22). These are given in Tables 4.6 and 4.7 for all the copper and iron specimens respectively.

Table 4.6 The calculated (n) values for each pair of rings of copper specimens at different accelerating voltage

Specimen	n					Acc. Voltage
	$\frac{111}{200}$	$\frac{111}{220}$	$\frac{111}{311}$	$\frac{111}{400}$	$\frac{111}{422}$	
Cu_1	0.78	0.84	1.09	1.11	1.17	
Cu_2	0.86	0.98	1.09	1.21	1.18	
Cu_3	0.93	0.92	1.20	1.02	1.27	200kV
Cu_4	1.10	0.94	1.14	1.24	1.40	
Cu_5	1.10	0.92	1.25	1.35	1.26	
Cu_1	1.02	1.12	1.20	1.58	1.62	
Cu_2	0.96	1.02	1.16	1.46	1.54	
Cu_3	1.00	1.01	1.11	1.31	1.36	600kV
Cu_4	0.86	1.00	1.15	1.26	1.27	
Cu_5	1.1	0.7	1.21	1.26	1.40	
Cu_1	1.11	1.21	1.45	1.75	1.75	
Cu_2	1.04	1.09	1.38	1.91	1.77	
Cu_3	1.04	1.12	1.36	1.81	1.85	1000kV
Cu_4	1.07	1.04	1.52	1.93	1.82	
Cu_5	1.14	1.00	1.62	1.91	1.83	

Table 4.7 The calculated (n) values for each pair of rings of ∝-iron specimens at different accelerating voltage.

Specimen	n					Acc. Voltage
	$\frac{110}{200}$	$\frac{110}{211}$	$\frac{110}{220}$	$\frac{110}{310}$	$\frac{110}{321}$	
Fe_1	0.95	0.88	0.98	1.16	1.29	
Fe_2	0.95	0.96	1.15	1.28	1.41	
Fe_3	0.76	0.91	1.21	1.22	1.36	200kV
Fe_4	0.89	1.01	1.25	1.29	1.42	
Fe_5	0.96	1.35	1.61	1.59	1.64	
Fe_1	0.97	1.13	1.20	1.40	1.44	
Fe_2	0.94	1.09	1.12	1.26	1.38	
Fe_3	1.02	1.17	1.27	1.34	1.42	600kV
Fe_4	1.11	1.25	1.29	1.43	1.58	
Fe_5	1.00	1.47	1.73	1.70	1.69	
Fe_1	-	-	-	-	-	
Fe_2	0.95	1.26	1.27	1.43	1.70	
Fe_3	1.00	1.39	1.43	1.60	1.71	
Fe_4	1.01	1.29	1.40	1.54	1.72	1000kV
Fe_5	-	2.12	2.19	1.98	1.99	

It can be seen from the last two tables (4.6 and 4.7) that the diffraction rings combinations have been chosen in such away to relate all possible diffraction rings in the pattern with the strongest one. The value of n for each pair of rings was calculated according to Equation 2.22.

It could be noticed that these calculated n values of the diffraction pairs for any particular specimen have lower values than that previously obtained for the same specimen as a whole (see Table 4.5).

However, the n values of the diffraction pairs given in Tables 4.6. and 4.7 of copper and α-iron specimen increase as we go further away from the centre spot of each diffraction pattern. Therefore, it was decided to analyse the relationship which existed between these values and their corresponding average Bragg angle $\bar{\theta}$ for each particular pattern.

The Bragg angle θ, of each diffraction ring, was calculated at different accelerating voltages by using Bragg relation (2.1).

The average Bragg angle $\bar{\theta}$ was given as:-

$$\bar{\theta} = \frac{\theta_{h_1k_1l_1} + \theta_{h_2k_2l_2}}{2} \qquad 4.3$$

where $\theta_{h_1k_1l_1}$ is the Bragg angle of the strongest line

in the pattern and $\theta_{h_2k_2l_2}$ is the Bragg angle for any other possible diffraction maxima in the pattern.

Table 4.8 shows the calculated $\bar{\theta}$ of the diffraction pairs of copper and α-iron at different accelerating voltages.

The values of (n) of the diffraction pairs of copper and α-iron specimens in the previous tables (4.6 and 4.7), were plotted against their average Bragg angles $\bar{\theta}$ for each specimen separately at different accelerating voltages. Samples from these plots of copper and α-iron specimens are shown in Figures 4.7 and 4.8 respectively.

It appeared from the previous plots that the values of n of each diffraction pattern increased as the average Bragg angles $\bar{\theta}$ and the accelerating voltages went higher.

However, the disagreement between the above results with the theoretical approach (at which the value of n was equal to 1 under entirely dynamical conditions and equal to 2 under entirely kinematical conditions), one could initially have explained the situation by assuming that the scattering process in each diffraction pattern involved both the dynamical and kinematical conditions, or in other words, the inner rings might have their intensities given by one theory whilst the outer rings have their intensities given by the other theory.

Table 4.8 The average Bragg angle ($\bar{\theta}$) for each pair of rings of copper and α-iron at different accelerating voltage.

Specimen	$\bar{\theta}(\frac{111+200}{2})$	$\bar{\theta}(\frac{111+220}{2})$	$\bar{\theta}(\frac{111+311}{2})$	$\bar{\theta}(\frac{111+400}{2})$	$\bar{\theta}(\frac{111+422}{2})$	Acc. Voltage
	0.405	0.495	0.548	0.623	0.72	200kV
copper	0.234	0.286	0.316	0.359	0.415	600kV
	0.181	0.222	0.245	0.278	0.322	1000kV
	$\bar{\theta}(\frac{110+200}{2})$	$\bar{\theta}(\frac{110+211}{2})$	$\bar{\theta}(\frac{110+220}{2})$	$\bar{\theta}(\frac{110+310}{2})$	$\bar{\theta}(\frac{110+321}{2})$	
	0.468	0.529	0.581	0.627	0.706	200kV
α-iron	0.270	0.305	0.335	0.361	0.407	600kV
	0.209	0.237	0.260	0.280	0.316	1000kV

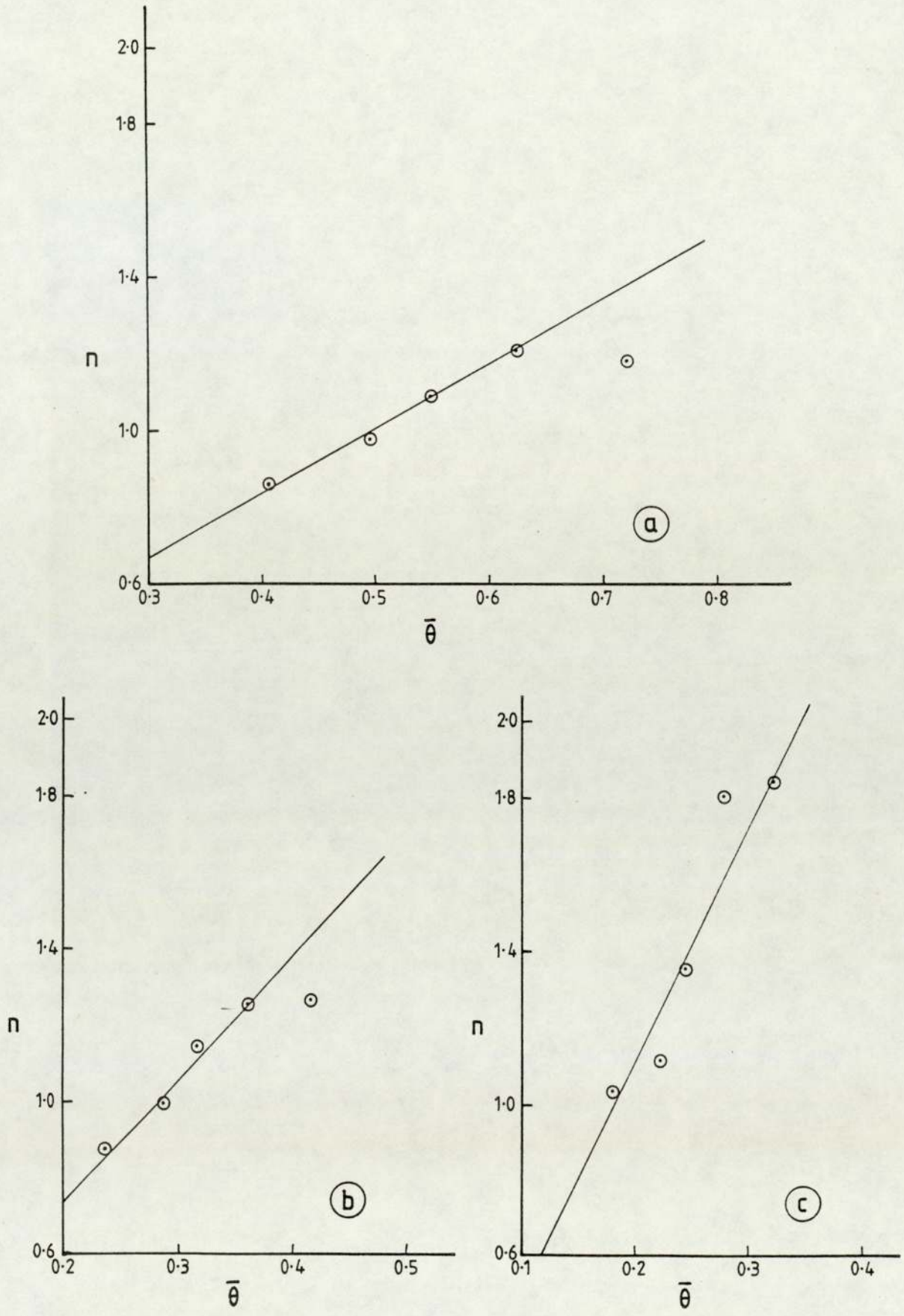

Fig.4.7 Variation of n with the average Bragg angle $\bar{\theta}$ for copper specimens. (a)200kV, (b)600kV, (c)1000kV.

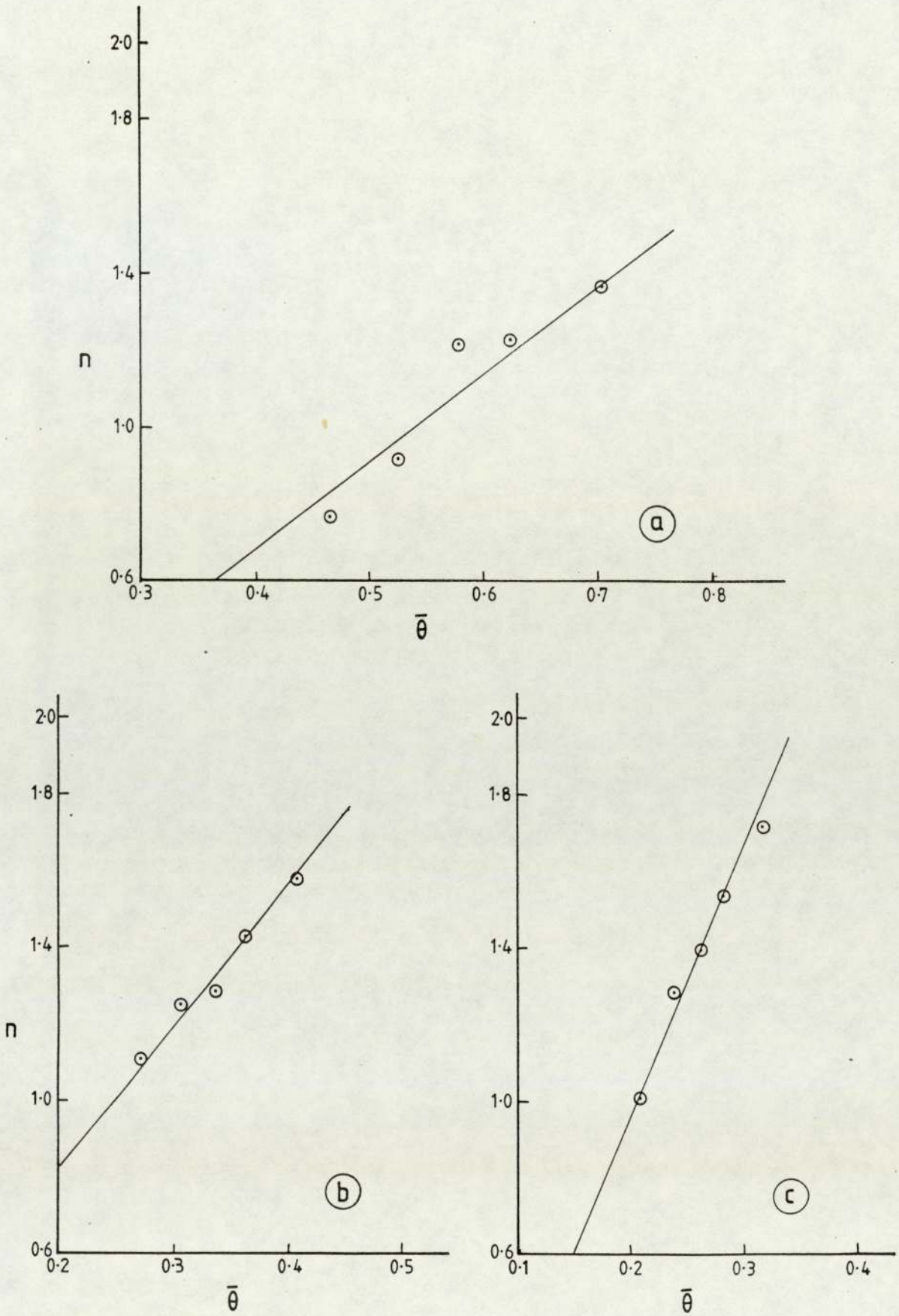

Fig.4.8 Variation of n with the average Bragg angle $\bar{\theta}$ for α-iron specimens. (a)200kV, (b)600kV, (c)1000kV.

Regarding this possible explanation, Kuwabara (6) stated "that when the thickness of the films was increased gradually, at first the reflexions of lower indices showed the dynamical intensity, and finally all the reflexions showed the dynamical one". This statement means that at a certain thickness, it could be possible for the rings of lower indices to have their intensities given by dynamic theory and the outer rings have their intensities given by kinematic theory. The results found in this work were in agreement with the previous statement.

On the other hand, it was shown in Chapter 2, that the critical thickness (t_c) of a specimen to produce equality between dynamic and kinematic intensities was inversely proportional to the structure factor ($F_e(\theta)$) and the electron wavelength (λ), (see Equation 2.19). For a given λ, however, it is possible for the inner rings of an electron diffraction pattern to have a smaller t_c than for the outer rings. This is obviously due to the difference in $F_e(\theta)$ values.

It could be concluded from the above argument that, for a certain ranges of specimen thickness, the intensities of the diffraction pattern would show a transition from dynamic intensities to kinematic ones as one moves further away from the centre spot. This is consistent with the results obtained earlier in this present work.

4.2 Proportional analysis of composite polycrystalline specimen.

Sandwich specimens of different film thicknesses combination from copper and ∝-iron were prepared by two stages vacuum evaporation directly onto carbon-coated electron microscope grids. Selected area diffraction patterns, for all specimens, were obtained and each diffraction pattern was analysed in terms of relative integrated intensities, by using Equation 2.23. This equation was modified from Equation 2.9 to allow the (R.I.I.) per unit length to be used.

$$\frac{I_1/I_2}{t_1/t_2} = \frac{k_1}{k_2} \cdot \frac{d_1}{d_2} \qquad 2.23$$

Where the subscripts 1 and 2 stand for the materials 1 and 2 respectively of the composite specimen. The theoretical expressions of the scattering factor (k) in Equation 2.23, for both kinematical and dynamical conditions, were given in Equations 2.24 and 2.25 respectively.

The aim of this experiment was to evaluate the thickness ratio of the two films constituent of the composite specimen from their relative integrated intensities ratio.

In this attempt, it was observed that Equation 2.23 was not a straightforward relation for this evaluation, because one does not know whether to use the kinematical or dynamical theory of electron diffraction to calculate

the scattering factors (k_1/k_2). Thus studying the diffraction conditions through the variation of the integrated intensities of selected pairs of rings from the two laminae of the specimen with their thickness ratios was essential.

4.2.1 Experimental results.

Twenty five composite specimens, from the same copper and ∝-iron films shown in Table 4.1, were obtained. The same procedures, as previously explained in Section 4.1, were carried out to calculate the relative integrated intensity for selected rings from each diffraction pattern. Figure 3.6 shows typical micro-densitometer traces from copper, ∝-iron and (copper + ∝-iron) specimens. It can be seen, from these traces, that Cu_{200}, Cu_{220}, Cu_{311}, Fe_{200} and Fe_{211} rings were suitable to be used for analysis. The relative integrated intensities of these rings from all diffraction patterns at different accelerating voltages were calculated and tabulated in Tables 4.9 to 4.11.

The composite specimens, referred to in the above tables, were prepared in such a way, that each particular thickness of copper specimens was overlaid with different thicknesses of ∝-iron films, so that various thicknesses ratios of copper and ∝-iron films would be obtained. It will be noticed, from the above tables, that some of the relative integrated intensities are missing. This was because some of the rings in the diffraction patterns

Table 4.9 The relative integrated intensity of (copper + ∝-iron) composite specimens at 200kV.

Specimen	$\frac{t_{Cu}}{t_{Fe}}$	Relative integrated intensity for (Cu + ∝-Fe)				
		$I_{Cu_{200}}$	$I_{Fe_{200}}$	$I_{Cu_{220}}$	$I_{Fe_{211}}$	$I_{Cu_{311}}$
Cu_1+Fe_1	0.71	5.18	3.54	3.08	4.95	3.35
Cu_1+Fe_2	1.27	8.78	3.15	4.97	6.17	6.78
Cu_1+Fe_3	1.82	-	-	-	-	-
Cu_1+Fe_4	2.77	13.92	2.08	10.50	4.20	9.50
Cu_1+Fe_5	3.81	15.22	1.78	10.50	-	12.82
Cu_2+Fe_1	0.51	6.60	2.32	2.81	4.86	4.62
Cu_2+Fe_2	0.91	10.85	2.49	5.61	5.49	7.58
Cu_2+Fe_3	1.3	9.51	1.79	6.82	3.88	7.55
Cu_2+Fe_4	1.98	11.78	1.09	7.35	4.14	9.60
Cu_2+Fe_5	2.73	14.82	0.68	9.92	-	9.90
Cu_3+Fe_1	0.4	-	5.00	2.79	7.63	3.65
Cu_3+Fe_2	0.72	6.4	4.09	4.75	7.50	4.84
Cu_3+Fe_3	1.03	12.60	3.60	8.46	7.35	8.92
Cu_3+Fe_4	1.57	13.44	2.44	10.49	4.80	11.45
Cu_3+Fe_5	2.16	15.65	2.40	11.95	-	12.25
Cu_4+Fe_1	0.33	-	3.80	3.90	10.20	4.46
Cu_4+Fe_2	0.60	8.36	4.50	4.30	8.84	5.22
Cu_4+Fe_3	0.86	12.74	3.49	9.00	9.30	10.27
Cu_4+Fe_4	1.3	11.40	4.40	8.60	5.75	9.12
Cu_4+Fe_5	1.8	15.48	1.96	12.00	-	12.20
Cu_5+Fe_1	0.26	-	4.32	1.66	8.64	2.35
Cu_5+Fe_2	0.46	6.68	5.10	3.36	10.24	3.60
Cu_5+Fe_3	0.66	20.92	10.08	13.50	16.07	13.50
Cu_5+Fe_4	1.0	19.99	8.66	14.31	7.88	12.60
Cu_5+Fe_5	1.38	24.15	5.28	19.35	-	15.74

Table 4.10 The relative integrated intensity of (copper + ∝-iron) composite specimens at 600kV.

Specimen	$\frac{t_{Cu}}{t_{Fe}}$	Relative integrated intensity for (Cu + ∝-Fe)				
		$I_{Cu_{200}}$	$I_{Fe_{200}}$	$I_{Cu_{220}}$	$I_{Fe_{211}}$	$I_{Cu_{311}}$
Cu_1+Fe_1	0.71	3.84	4.06	4.26	7.76	4.29
Cu_1+Fe_2	1.27	9.41	4.50	7.79	8.38	7.80
Cu_1+Fe_3	1.82	16.24	-	11.62	6.97	14.70
Cu_1+Fe_4	2.77	14.85	-	11.34	3.90	11.94
Cu_1+Fe_5	3.81	15.60	-	11.40	-	12.98
Cu_2+Fe_1	0.51	7.75	2.97	4.03	7.63	5.70
Cu_2+Fe_2	0.91	11.59	4.22	7.95	8.25	8.84
Cu_2+Fe_3	1.3	12.90	2.16	8.45	5.39	9.17
Cu_2+Fe_4	1.98	12.65	2.28	10.95	4.69	10.05
Cu_2+Fe_5	2.73	15.98	-	10.90	-	11.47
Cu_3+Fe_1	0.4	4.59	6.08	4.14	10.56	4.13
Cu_3+Fe_2	0.72	-	-	-	-	-
Cu_3+Fe_3	1.03	8.96	3.71	8.00	7.00	7.99
Cu_3+Fe_4	1.57	9.75	-	9.68	4.84	9.98
Cu_3+Fe_5	2.16	11.18	-	9.52	-	9.95
Cu_4+Fe_1	0.33	5.81	5.53	3.52	9.24	3.35
Cu_4+Fe_2	0.60	4.05	5.37	3.96	8.94	3.17
Cu_4+Fe_3	0.86	8.94	3.47	7.98	7.50	8.19
Cu_4+Fe_4	1.3	11.25	1.68	9.24	5.80	9.54
Cu_4+Fe_5	1.8	10.09	-	11.10	-	9.32
Cu_5+Fe_1	0.26	-	-	-	-	-
Cu_5+Fe_2	0.46	4.69	5.95	3.71	9.03	3.42
Cu_5+Fe_3	0.66	7.13	4.16	6.00	6.57	5.73
Cu_5+Fe_4	1.0	7.20	-	7.70	3.60	6.63
Cu_5+Fe_5	1.38	9.11	-	15.04	-	8.20

Table 4.11 The relative integrated intensity of (copper + ∝-iron) composite specimens at 1000kV.

Specimen	$\frac{t_{Cu}}{t_{Fe}}$	Relative integrated intensity for (Cu + ∝-Fe)				
		$I_{Cu_{200}}$	$I_{Fe_{200}}$	$I_{Cu_{220}}$	$I_{Fe_{211}}$	$I_{Cu_{311}}$
Cu_1+Fe_1	0.71	9.11	3.17	4.56	8.26	5.89
Cu_1+Fe_2	1.27	10.28	3.53	6.41	7.54	7.25
Cu_1+Fe_3	1.82	19.24	-	8.26	4.14	9.96
Cu_1+Fe_4	2.77	12.20	-	8.10	4.15	8.91
Cu_1+Fe_5	3.81	17.92	-	12.65	-	12.27
Cu_2+Fe_1	0.51	6.29	3.57	3.52	6.75	3.88
Cu_2+Fe_2	0.91	7.30	2.39	4.06	5.86	5.82
Cu_2+Fe_3	1.3	13.90	1.48	9.65	5.16	9.32
Cu_2+Fe_4	1,98	15.86	1.31	8.69	4.77	10.25
Cu_2+Fe_5	2.73	20.58	-	12.05	3.23	11.99
Cu_3+Fe_1	0.4	7.14	5.85	3.76	10.20	3.90
Cu_3+Fe_2	0.72	9.59	5.33	6.18	9.90	6.11
Cu_3+Fe_3	1.03	12.54	1.89	7.68	6.42	7.59
Cu_3+Fe_4	1.57	14.40	-	10.14	-	9.45
Cu_3+Fe_5	2.16	15.12	-	11.85	-	10.81
Cu_4+Fe_1	0.33	2.80	3.38	2.09	6.84	2.77
Cu_4+Fe_2	0.60	9.24	5.94	5.25	9.60	4.59
Cu_4+Fe_3	0.86	13.56	-	10.67	11.75	12.15
Cu_4+Fe_4	1.3	16.52	-	12.65	11.04	15.45
Cu_4+Fe_5	1.8	-	-	-	-	-
Cu_5+Fe_1	0.26	-	-	-	-	-
Cu_5+Fe_2	0.46	-	-	-	-	-
Cu_5+Fe_3	0.66	13.75	-	11.02	12.00	10.42
Cu_5+Fe_4	1.0	14.30	-	12.90	8.40	11.13
Cu_5+Fe_5	1.38	21.68	-	18.11	-	14.62

were not clear enough to be traced by the microdensitometer.

4.2.2 Analysis of the diffraction patterns obtained from composite specimens.

The relative integrated intensities shown in the previous tables (4.9 to 4.11) were the basic experimental results to be analysed. The composite specimens of copper and ∝-iron were listed as combinations of copper + ∝-iron.

According to Equation 2.23, an attempt to evaluate the ratio of the scattering factors (k_1/k_2), by plotting the relative integrated intensity ratio against thickness ratio of the two laminae composite specimen, may reveal significant tendencies.

Figures 4.9 to 4.11 are sample graphs of the intensity ratio (I_{Cu}/I_{Fe}) versus thickness ratio (t_{Cu}/t_{Fe}), at which two diffraction pairs of rings at each particular voltage, were chosen.

It can be seen, from these plots, that the intensity ratio increased as the thickness ratio increased. But more than one straight line passing through the experimental points, in each plot, could be drawn. The scattered points in these figures (4.9 to 4.11) may be justified for the reason that some unestimated experimental errors were involved during the measurement.

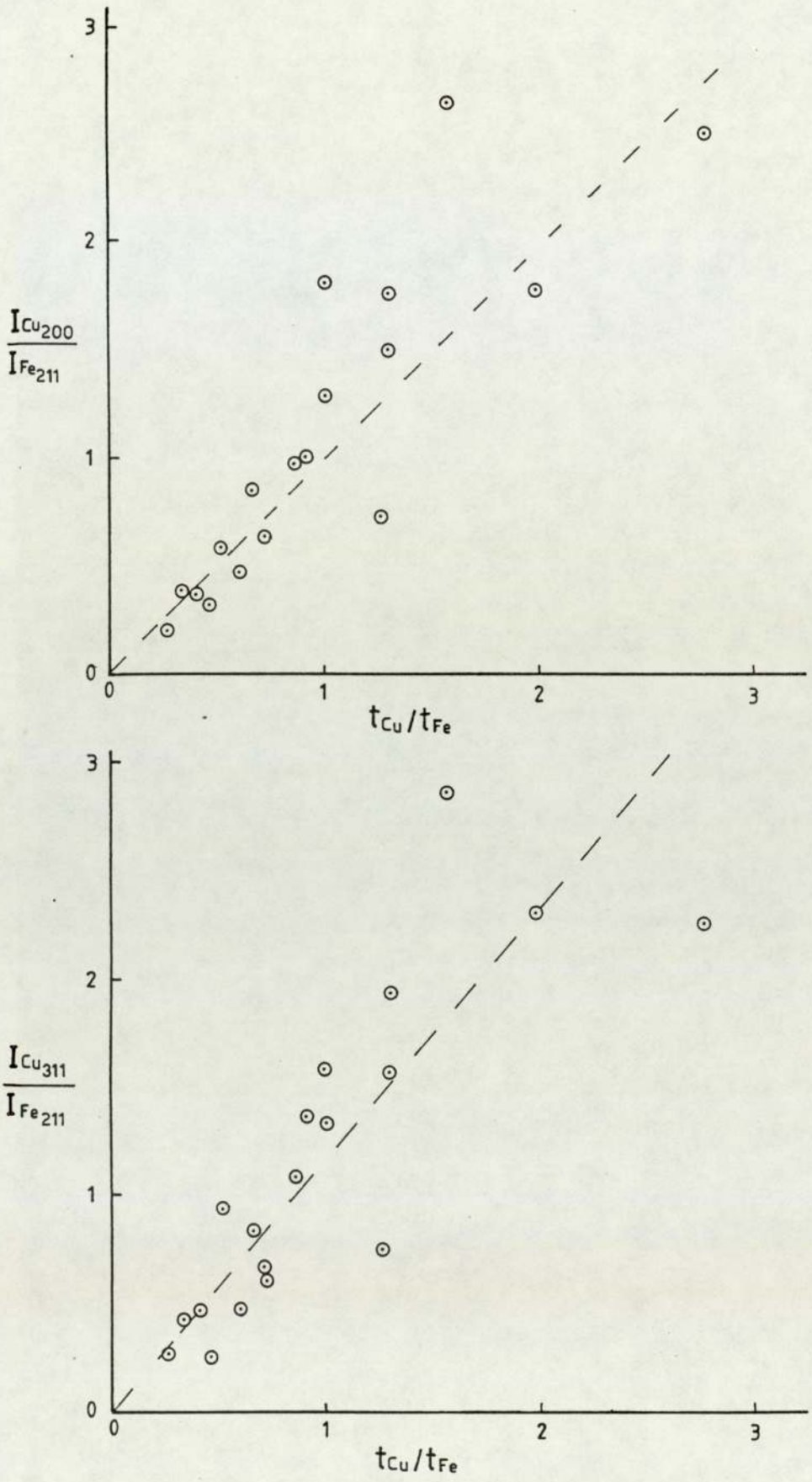

Fig.4.9 Relative integrated intensity ratio versus thickness ratio for (α-iron + copper) composite specimens at 200kV.

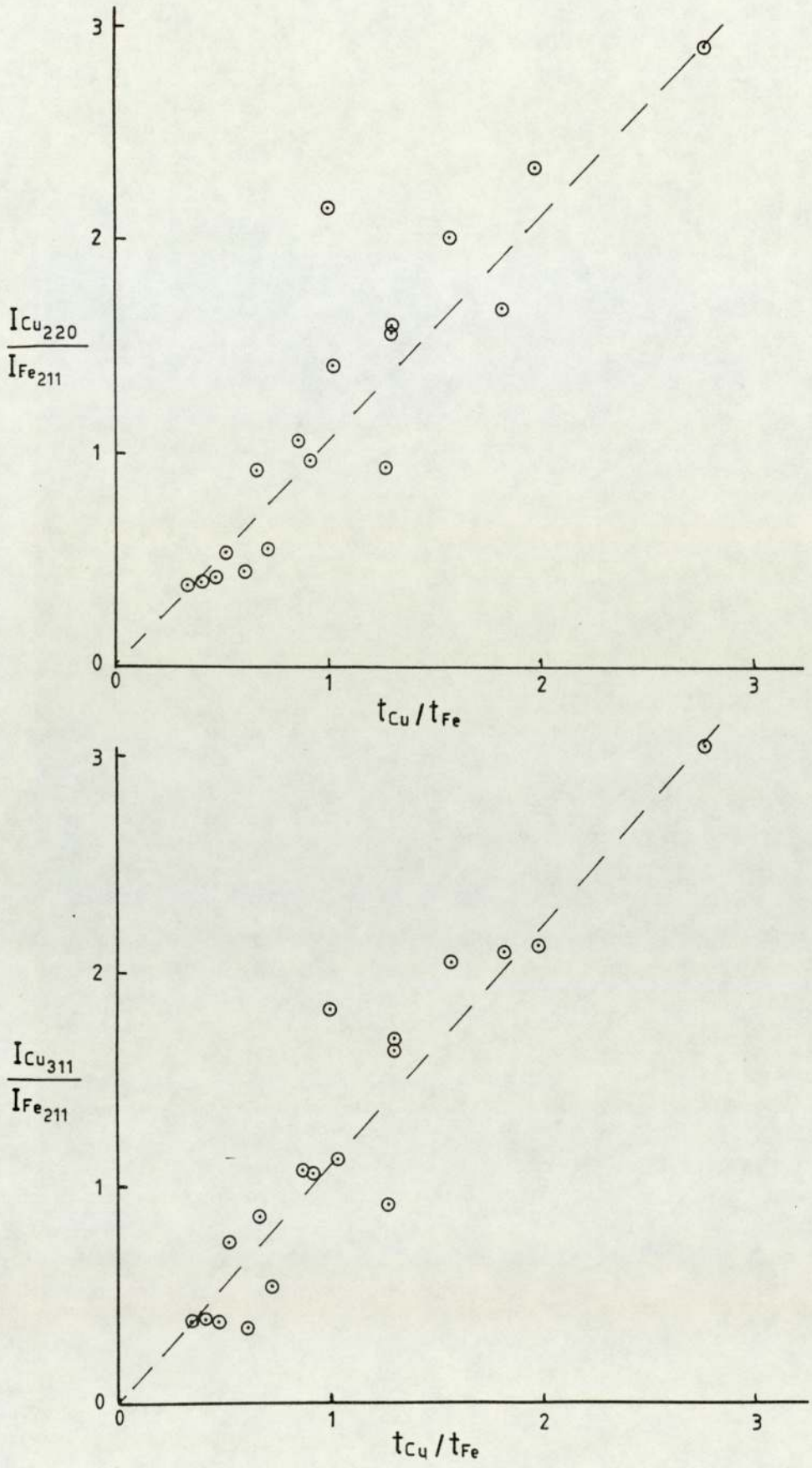

Fig. 4.10 Relative integrated intensity ratio versus thickness ratio for (∝-iron + copper) composite specimens at 600kV.

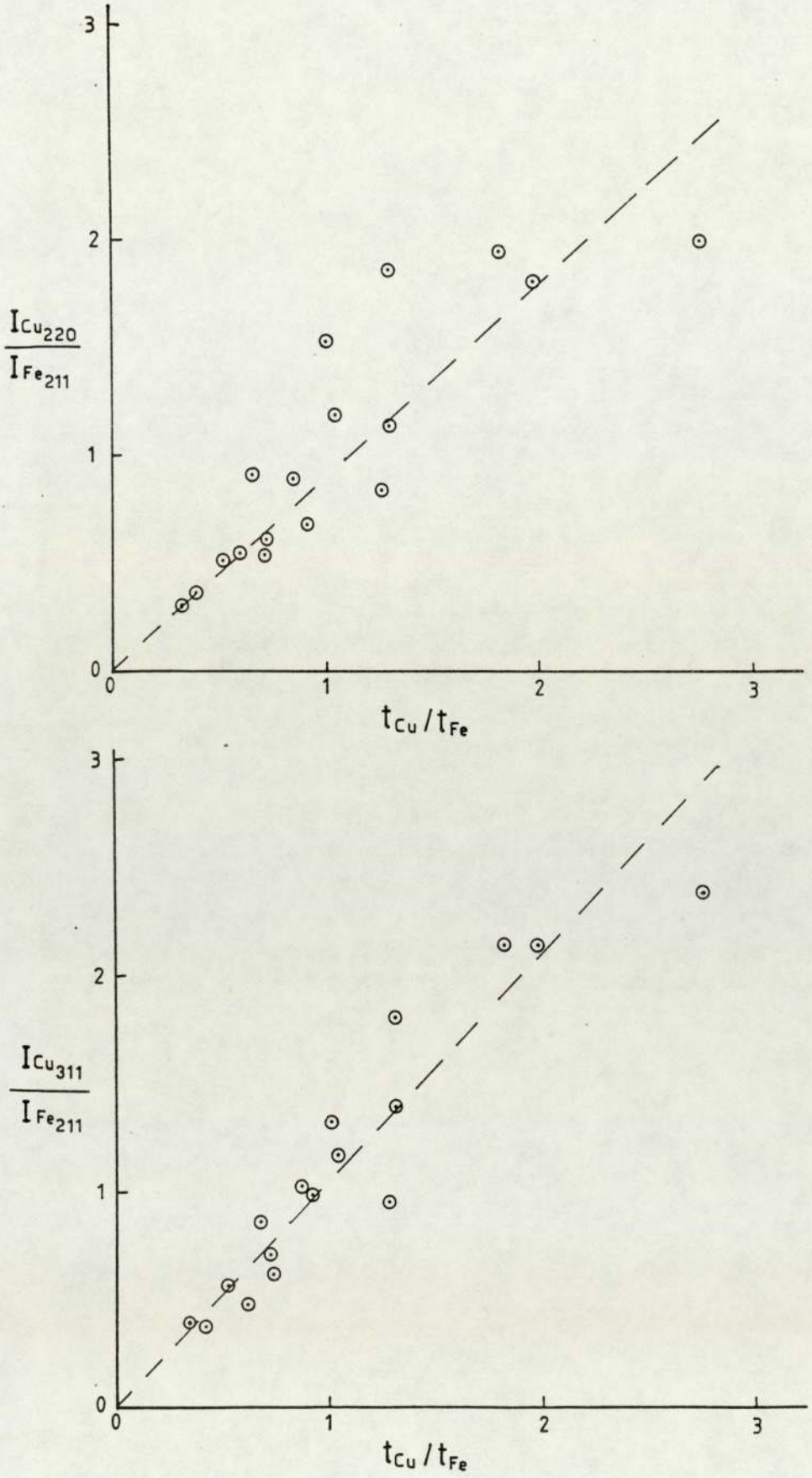

Fig. 4.11 Relative integrated intensity ratio versus thickness ratio for (α-iron + copper) composite specimens at 1000kV.

But the main reason could be understood by referring to Equations 2.26 and 2.27 of the kinematical and dynamical expressions respectively. The kinematical expression (2.26) shows that the intensity ratio to the thickness ratio should give a constant value, for each particular pair of rings. This means the experimental points of the intensity ratio versus thickness ratio should lie on a straight line passing through the origin with slope equal to the constant value mentioned above. However, the dynamical expression (2.27) shows that the intensity ratio to the thickness ratio, for any particular pair of rings, would give different values for different crystallite sizes of the two laminae composite specimen. Therefore, one should expect scattered points in the plot of the intensity ratio versus thickness ratio, if both theories are operative.

Referring to the above argument, one suspects that the experimental results, shown in Figures 4.9 to 4.11, were not obtained completely under kinematical theory. The scattered points in these figures may reveal that the scattering process was under dynamical theory or a mixture of dynamical and kinematical effects.

Therefore, measuring the slope of each plot, to evaluate the ratio of the scattering factors (k_1/k_2)(16) is an unsuitable method.

In Chapter 2, the general Equation 2.28 was written from

Equations 2.26 and 2.27

$$\frac{I_1/I_2}{t_1/t_2}\cdot\frac{d_2^2P_2}{d_1^2P_1}=\left[\frac{F_e(\theta)_1\cdot e^{-D_1}\cdot v_2}{F_e(\theta)_1\cdot e^{-D_2}\cdot v_1}\right]^n\cdot\left(\frac{\epsilon_2}{\epsilon_1}\right)^{2-n} \qquad 2.28$$

In order to allow Equation 2.28 to be used, let us consider the crystallite sizes of the two laminae in the composite specimens are equal. Taking the logarithm of the two sides of this equation, would give:-

$$\log\left[\frac{I_1/I_2}{t_1/t_2}\cdot\frac{d_2^2P_2}{d_1^2P_1}\right]=n\log\left[\frac{F_e(\theta)_1\cdot e^{-D_1}\cdot v_2}{F_e(\theta)_2\cdot e^{-D_2}\cdot v_1}\right] \qquad 4.4$$

Then the logarithmic plot of

$\frac{I_1/I_2}{t_1/t_2}\cdot\frac{d_2^2P_2}{d_1^2P_1}$ versus $\frac{F_e(\theta)_1\cdot e^{-D_1}\cdot v_2}{F_e(\theta)_2\cdot e^{-D_2}\cdot v_1}$ should, therefore, produce a straight line whose slope is equal to the value of n which determines whether a given composite specimen diffracted according to the kinematic or dynamic theory of electron diffraction.

The above equation could be written in the following form:-

$$\log(G) = n\log(F) \qquad 4.5$$

where $G=\frac{I_1/I_2}{t_1/t_2}\cdot\frac{d_2^2P_2}{d_1^2P_1}$ and $F=\frac{F_e(\theta)_1\cdot e^{-D_1}\cdot v_2}{F_e(\theta)_2\cdot e^{-D_2}\cdot v_1}$ 4.6

The values of F of the diffraction pairs were calculated by the aid of Tables A.1 and B.1, (see Appendix), and listed in Table 4.12.

Table 4.12 The calculated values of F

$(hkl)_{Cu}$ / $(hkl)_{Fe}$	F
200/200	1.24
200/211	1.60
220/200	0.85
220/211	1.10
311/200	0.70
311/211	0.91

The G values of the diffraction pairs for all specimens at different accelerating voltages were calculated as shown in Tables 4.13 to 4.15. A logarithmic plot of the values of G against the values of F could then be drawn for each specimen separately as shown in the sample Figures 4.12 to 4.14.

It can be seen, from Figures (4.12 to 4.14), that a straight line. passing through the experimental points of each plot, could be drawn. This was the case for most of the plots, the remainder showed a considerable scattering of points.

However, according to Equation 4.4 the slope of each plot is equal to the value of n. These values were measured and tabulated in Table (4.16).

Table 4.13 The experimental values of G at 200kV

$$G = \frac{I_1/I_2}{t_1/t_2} \cdot \frac{d_2^2 P_2}{d_1^2 P_1}$$

Specimen	$\frac{Cu_{200}}{Fe_{200}}$	$\frac{Cu_{200}}{Fe_{211}}$	$\frac{Cu_{220}}{Fe_{200}}$	$\frac{Cu_{220}}{Fe_{211}}$	$\frac{Cu_{311}}{Fe_{200}}$	$\frac{Cu_{311}}{Fe_{211}}$
Cu_1+Fe_1	1.29	2.47	0.77	1.47	0.58	1.10
Cu_1+Fe_2	1.37	2.02	0.78	1.05	0.73	0.99
Cu_1+Fe_3	-	-	-	-	-	-
Cu_1+Fe_4	1.51	2.00	1.14	1.50	0.71	0.94
Cu_1+Fe_5	-	-	-	-	-	-
Cu_2+Fe_1	3.51	4.47	1.49	1.90	1.69	2.16
Cu_2+Fe_2	2.99	3.62	1.54	1.87	1.44	1.73
Cu_2+Fe_3	2.56	3.13	1.83	2.25	1.40	1.71
Cu_2+Fe_4	3.40	2.38	2.12	1.50	1.90	1.34
Cu_2+Fe_5	-	-	-	-	-	-
Cu_3+Fe_1	-	-	-	-	-	-
Cu_3+Fe_2	1.36	2.00	1.00	1.47	0.66	0.97
Cu_3+Fe_3	2.13	2.77	1.43	1.87	1.04	1.51
Cu_3+Fe_4	2.20	3.60	1.72	2.82	1.29	2.11
Cu_3+Fe_5	-	-	-	-	-	-
Cu_4+Fe_1	-	-	-	-	-	-
Cu_4+Fe_2	1.94	2.63	0.99	1.35	0.83	1.13
Cu_4+Fe_3	2.66	2.67	1.88	1.88	1.48	1.48
Cu_4+Fe_4	1.24	2.53	0.94	1.92	0.69	1.40
Cu_4+Fe_5	-	-	-	-	-	-
Cu_5+Fe_1	-	-	-	-	-	-
Cu_5+Fe_2	1.44	2.37	0.73	1.18	0.53	0.87
Cu_5+Fe_3	2.26	3.30	1.28	2.13	0.88	1.47
Cu_5+Fe_4	1.44	4.23	1.03	3.03	0.62	1.84
Cu_5+Fe_5	-	-	-	-	-	-

Table 4.14 The experimental values of G at 600kV

$$G = \frac{I_1/I_2}{t_1/t_2} \cdot \frac{d_2^2 P_2}{d_1^2 P_1}$$

Specimen	$\frac{Cu_{200}}{Fe_{200}}$	$\frac{Cu_{200}}{Fe_{211}}$	$\frac{Cu_{220}}{Fe_{200}}$	$\frac{Cu_{220}}{Fe_{211}}$	$\frac{Cu_{311}}{Fe_{200}}$	$\frac{Cu_{311}}{Fe_{211}}$
Cu_1+Fe_1	0.84	1.17	0.93	1.30	0.64	0.90
Cu_1+Fe_2	1.03	1.47	0.85	1.22	0.59	0.84
Cu_1+Fe_3	-	2.13	-	1.53	-	1.33
Cu_1+Fe_4	-	2.28	-	1.75	-	1.28
Cu_1+Fe_5	-	-	-	-	-	-
Cu_2+Fe_1	3.22	3.33	1.68	1.73	1.63	1.69
Cu_2+Fe_2	1.88	2.57	1.29	1.77	0.99	1.34
Cu_2+Fe_3	2.86	3.07	1.88	2.00	1.41	1.51
Cu_2+Fe_4	1.75	2.27	1.51	1.97	0.96	1.24
Cu_2+Fe_5	-	-	-	-	-	-
Cu_3+Fe_1	1.18	1.80	1.06	1.63	0.73	1.13
Cu_3+Fe_2	-	-	-	-	-	-
Cu_3+Fe_3	1.47	2.07	1.31	1.85	0.90	1.28
Cu_3+Fe_4	-	2.15	-	2.13	-	1.52
Cu_3+Fe_5	-	-	-	-	-	-
Cu_4+Fe_1	1.97	3.15	1.19	1.90	0.78	1.25
Cu_4+Fe_2	0.80	2.92	0.78	1.23	0.43	0.68
Cu_4+Fe_3	1.88	2.32	1.68	2.06	1.19	1.46
Cu_4+Fe_4	3.22	2.48	2.64	2.03	1.88	1.46
Cu_4+Fe_5	-	-	-	-	-	-
Cu_5+Fe_1	-	-	-	-	-	-
Cu_5+Fe_2	1.07	1.88	0.85	1.48	0.54	0.94
Cu_5+Fe_3	1.63	2.75	1.38	2.32	0.91	1.53
Cu_5+Fe_4	-	3.33	-	3.57	-	2.11
Cu_5+Fe_5	-	-	-	-	-	-

Table 4.15 The experimental values of G at 1000kV

$$G = \frac{I_1/I_2}{t_1/t_2} \cdot \frac{d_2^2 P_2}{d_1^2 P_1}$$

Specimen	$\frac{Cu_{200}}{Fe_{200}}$	$\frac{Cu_{200}}{Fe_{211}}$	$\frac{Cu_{220}}{Fe_{200}}$	$\frac{Cu_{220}}{Fe_{211}}$	$\frac{Cu_{311}}{Fe_{200}}$	$\frac{Cu_{311}}{Fe_{211}}$
Cu_1+Fe_1	2.54	2.60	1.27	1.30	1.13	1.16
Cu_1+Fe_2	1.43	1.78	0.89	1.12	0.69	0.86
Cu_1+Fe_3	-	4.25	-	1.83	-	1.52
Cu_1+Fe_4	-	1.77	-	1.17	-	0.90
Cu_1+Fe_5	-	-	-	-	-	-
Cu_2+Fe_1	2.18	3.07	1.21	1.72	0.92	1.30
Cu_2+Fe_2	2.09	2.28	1.16	1.27	1.15	1.25
Cu_2+Fe_3	4.51	3.45	3.12	2.38	2.08	1.60
Cu_2+Fe_4	3.82	2.80	2.09	1.53	1.70	1.24
Cu_2+Fe_5	-	3.88	-	2.28	-	1.56
Cu_3+Fe_1	1.91	2.92	1.01	1.53	0.72	1.10
Cu_3+Fe_2	1.56	2.25	1.01	1.45	0.69	0.99
Cu_3+Fe_3	4.03	3.17	2.47	1.93	1.68	1.32
Cu_3+Fe_4	-	-	-	-	-	-
Cu_3+Fe_5	-	-	-	-	-	-
Cu_4+Fe_1	1.56	2.05	1.16	1.53	1.06	1.40
Cu_4+Fe_2	1.62	2.67	0.92	1.52	0.56	0.92
Cu_4+Fe_3	-	2.25	-	1.77	-	1.39
Cu_4+Fe_4	-	1.92	-	1.47	-	1.23
Cu_4+Fe_5	-	-	-	-	-	-
Cu_5+Fe_1	-	-	-	-	-	-
Cu_5+Fe_2	-	-	-	-	-	-
Cu_5+Fe_3	-	2.90	-	2.33	-	1.52
Cu_5+Fe_4	-	2.83	-	2.57	-	1.53
Cu_5+Fe_5	-	-	-	-	-	-

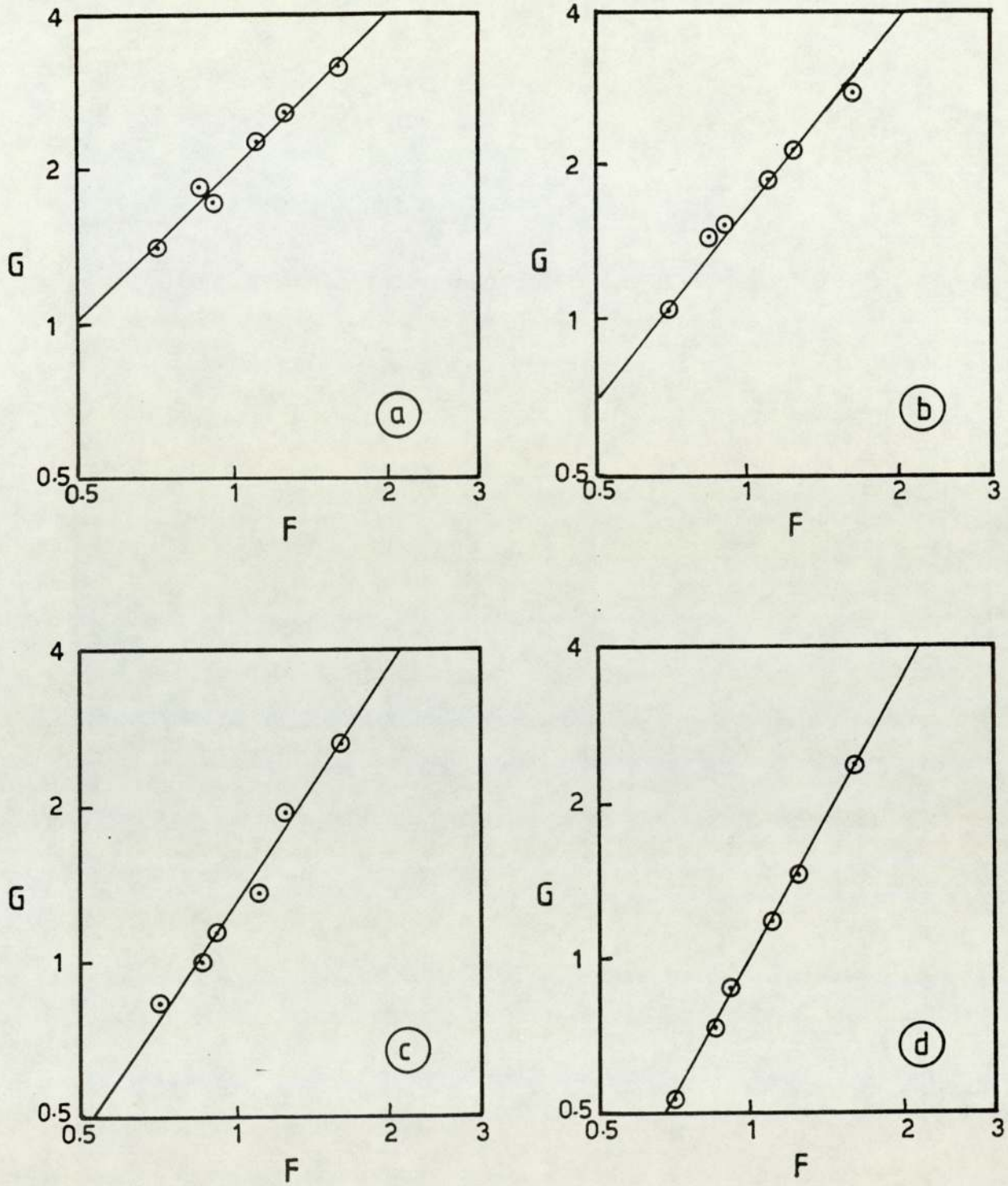

Fig. 4.12 Logarithmic plot of G versus F for (α-iron + copper) composite specimens at 200kV.
a:(Cu_2+Fe_3), b:(Cu_3+Fe_3), c:(Cu_4+Fe_2), d:(Cu_5+Fe_2).

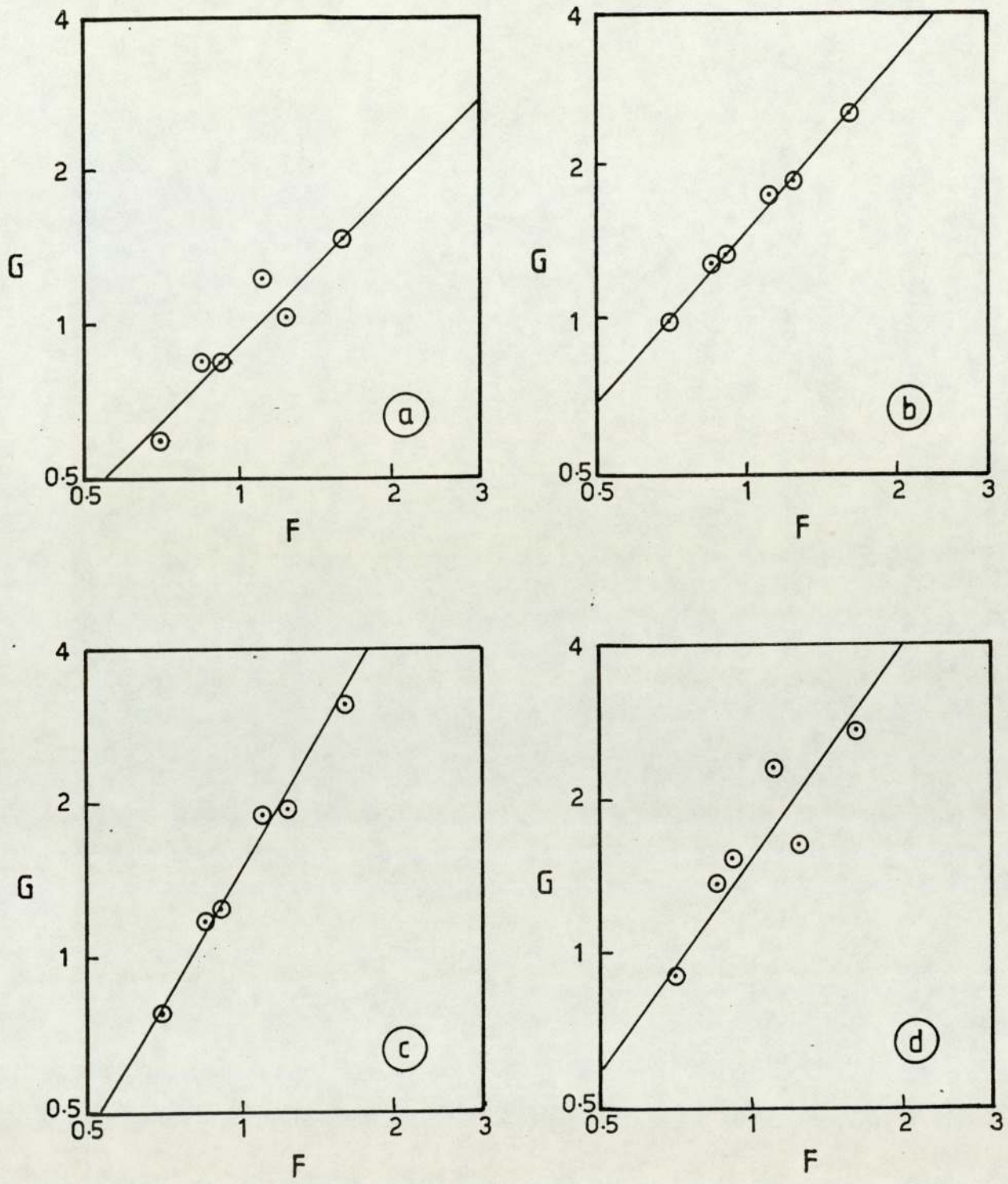

Fig. 4.13 Logarithmic plot of G versus F for (∝-iron + copper) composite specimens at 600kV.
a:(Cu_1+Fe_2), b:(Cu_2+Fe_2), c:(Cu_4+Fe_1), d:(Cu_5+Fe_3).

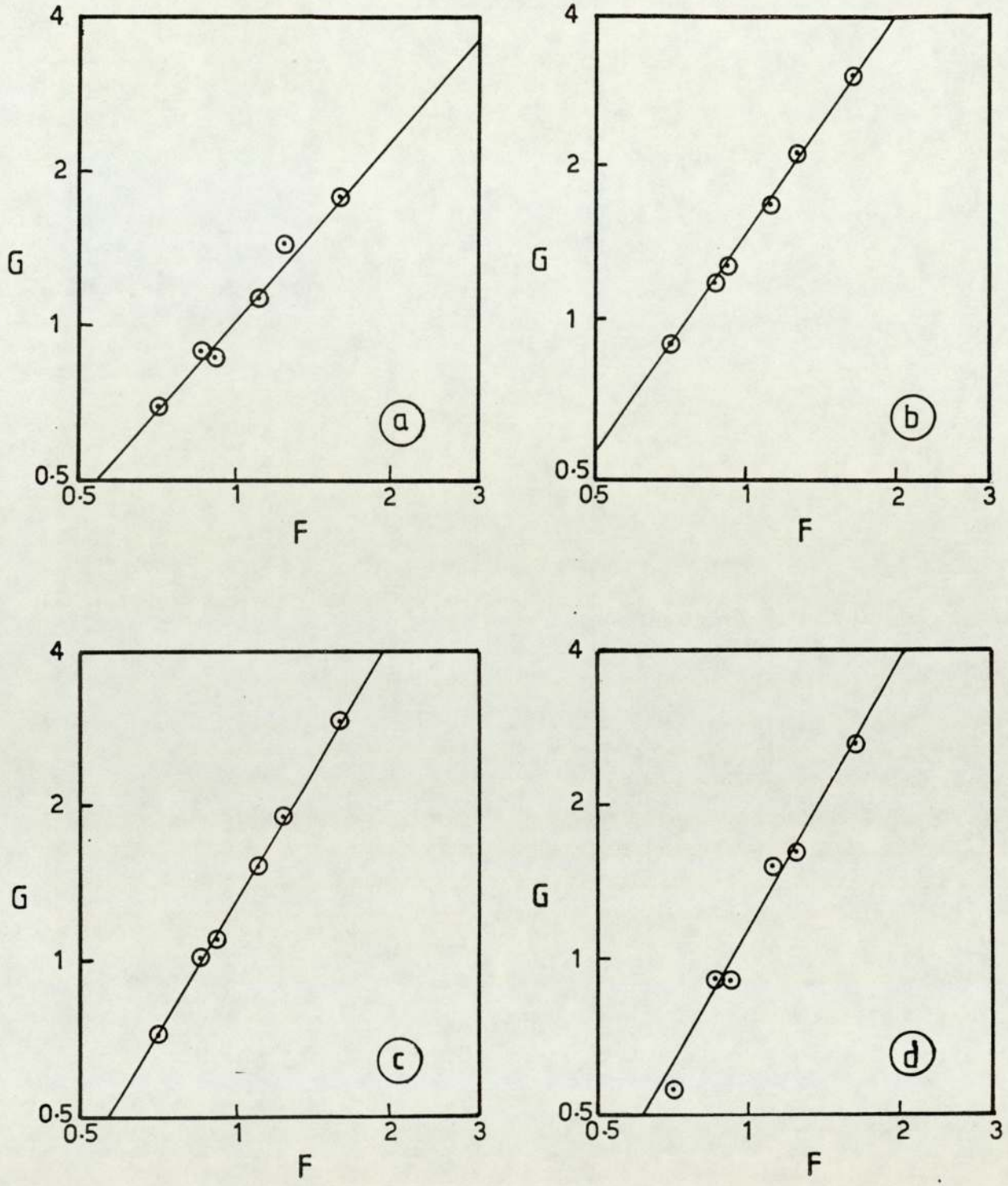

Fig. 4.14 Logarithmic plot of G versus F for (α-iron + copper) composite specimens at 1000kV.
a:(Cu_1+Fe_2), b:(Cu_2+Fe_1), c:(Cu_3+Fe_1), d:(Cu_4+Fe_2).

Table 4.16 The values of n for the composite specimens.

Specimens	Total thickness (nm) Cu + Fe	n		
		200kV	600kV	1000kV
$Cu_1 + Fe_1$	153.7	1.76	0.9	0.98
$Cu_1 + Fe_2$	113.7	1.36	1.0	1.14
$Cu_1 + Fe_4$	86.7	1.31	-	-
$Cu_2 + Fe_1$	135.6	1.51	1.06	1.44
$Cu_2 + Fe_2$	95.6	1.35	1.13	1.14
$Cu_2 + Fe_3$	80.6	0.98	0.97	1.38
$Cu_2 + Fe_4$	68.6	1.3	1.05	1.29
$Cu_3 + Fe_1$	126.0	-	1.18	1.67
$Cu_3 + Fe_2$	86.0	1.36	-	1.38
$Cu_3 + Fe_3$	71.0	1.24	1.16	1.33
$Cu_3 + Fe_4$	59.0	1.14	-	-
$Cu_4 + Fe_1$	120.0	-	1.73	0.86
$Cu_4 + Fe_2$	80.0	1.51	2.64	1.76
$Cu_4 + Fe_3$	65.0	1.43	0.81	-
$Cu_4 + Fe_4$	53.0	1.58	2.07	-
$Cu_5 + Fe_2$	73.0	1.84	1.59	-
$Cu_5 + Fe_3$	58.0	1.48	1.36	-
$Cu_5 + Fe_4$	46.0	2.21	-	-

The above table (4.16) shows the obtained values of n for each specimen at different accelerating voltages with the total thickness of the two laminae composite specimens.

It can be noticed that most of these values are close to unity, indicating that I_1 and I_2 (see Equation 4.4) were obtained under dynamical conditions. But this is not enough to emphasise the scattering process involved, since there are about 40% of the specimens showing values of n close to two.

However, Equation 2.28 assumes "all dynamic" or "all kinematic" conditions occur for each set of specimens. It is much better to consider Equations 2.26 and 2.27 as two special cases, with other possible cases regarding I_1, being kinematical and I_2 dynamical (or vice versa) according to the thicknesses of the two laminae of composite specimen.

In this way, one could compare the thicknesses of the two laminae composite specimen with the critical thicknesses shown in Table 6.1 (Chapter 6) to decide which one of the above cases should be used. The success of this method would mean that one can determine the thickness ratio $(\frac{t_1}{t_2})$ of the two laminae of composite specimen from their relative integrated intensity ratio $(\frac{I_1}{I_2})$ by using one of the above cases accordingly.

In order to examine the method mentioned above, the experimental analysis should include a very wide range of thicknesses for each lamina in the composite specimens. Also it is important to avoid the effect of the proportion of the amorphous material which was caused by the amorphous carbon substrate as we shall see in Chapter 6.

CHAPTER FIVE

CONTRAST IN ELECTRON DIFFRACTION PATTERNS.

5.1 The effect of amorphous material on the diffraction patterns.

It has long been known that when a beam of electrons passes through a thin polycrystalline metal film, the diffracted ring intensities depend upon the extent of the crystalline region in the specimen. The effect of the proportion of amorphous material produces an additional incoherent elastic scattering to the background intensity and hence the intensity of the rings is reduced as compared with the background. If the relative intensities are also affected by the proportion of amorphous material, then it is difficult to compare the relative ring intensity with values predicted by the kinematical and dynamical diffraction theories. In this investigation we shall concentrate on the effect of the amorphous substrate on the contrast of electron diffraction patterns.

5.2 Experimental techniques and results.

Sets of different film thicknesses from pure aluminium, α-iron and silver were prepared by vacuum evaporation directly onto carbon-coated microscope grids. Evaporated films of aluminium and silver, which have lower and higher atomic numbers respectively than α-iron, were used to investigate the effect of atomic number on

contrast. The evaporation techniques and the measurement of the film thicknesses were similar to those mentioned in Sections 3.1 and 3.5. The diffraction patterns were recorded in an electron microscope in the selected area electron diffraction mode of operation with an adequate diffraction aperture to give rings of uniform intensity. High accelerating voltages, up to 1000kV, were used to explore the single scattering region, i.e. ($t/\lambda_T \leqslant 1$), where λ_T is the total electron mean free path, and t is the film thickness. Four photographs at different exposure times were taken of the diffraction patterns from a selected specimen to enable a calibration curve of "exposure versus optical density" to be obtained for each batch of photographic films used. The density variations in each film were measured with an Automatic Recording Microdensitometer, (see Section 3.3).

Table 5.1 shows the film thicknesses of aluminium, α-iron and silver specimens which were prepared by vacuum evaporation onto glass microscope slides. These thicknesses were measured by the aid of a multiple-beam interferometer.

Table 5.1 Specimen thicknesses.

Material	Film thickness / nm								
Aluminium	168	145	104	68	50	45	36	30	20
α-iron	90	50	35	23	16.7				
Silver	105	67	60	47.5	40	31	27	20	

The electron mean free paths for elastic (λ_e) and inelastic (λ_i) scattering were calculated by using data from Lenz (22), (see Appendix 3). The total electron mean free path (λ_T) was then calculated, using Equation 1.3. The resulting values of (λ_T) are given in Table C.1.

Referring to Section 1.1 and Figure 1.3 the electron diffraction contrast C(hkl) can be defined by the following equation:-

$$C(hkl) = \frac{\mathcal{E}_p}{\mathcal{E}_B}\frac{w}{W} \qquad 5.1$$

where $\mathcal{E}_p$ is the "Exposure dose" (intensity multiplied by the exposure time) of the peak,

w is the width of the peak at the half peak point,

$\mathcal{E}_B$ is the "Exposure dose"of the background and

W is the width of the background.

However, the electron diffraction contrast C(hkl) for the strongest rings from the diffraction patterns of aluminium, α-iron and silver have been measured by applying Equation 5.1 to the microdensitometer traces of each diffraction pattern.

Tables 5.2, 5.3 and 5.4 show the contrast results of aluminium, α-iron and silver specimens respectively for different accelerating voltages.

Table 5.2 Diffraction contrast results of the aluminium specimens.

	Contrast results							
	200kV		400kV		600kV		1000kV	
t_{Al} (nm)	C(111)	C(220)	C(111)	C(220)	C(111)	C(220)	C(111)	C(220)
168	-	-	0.246	0.22	0.262	0.25	0.42	0.36
145	0.214	0.195	0.278	0.245	0.309	0.24	0.34	0.34
104	0.295	0.248	0.388	0.43	0.385	0.37	0.58	0.53
68	0.418	0.30	0.395	0.30	0.519	0.36	0.667	0.61
50	0.502	0.39	0.55	0.40	0.54	0.42	0.467	0.37
45	0.642	0.49	0.69	0.52	0.66	0.45	0.71	0.40
36	0.71	0.55	0.59	0.38	0.59	0.35	0.67	0.46
30	0.62	0.41	0.57	0.40	0.58	0.39	0.56	0.39
20	0.46	0.31	0.42	0.23	0.39	0.22	0.39	0.25

Table 5.3 Diffraction contrast result of the ∝-iron specimens.

	Contrast results							
	100kV		200kV		600kV		1000kV	
t_{Fe} (nm)	C(110)	C(211)	C(110)	C(211)	C(110)	C(211)	C(110)	C(211)
90	0.32	0.27	0.41	0.34	0.64	0.51	-	-
50	0.53	0.37	0.58	0.46	0.70	0.55	0.74	0.52
35	0.57	0.40	0.56	0.45	0.61	0.45	0.54	0.37
23	0.62	0.44	0.56	0.38	0.44	0.29	0.51	0.36
16.7	0.67	0.35	0.50	0.30	0.38	0.26	0.35	0.18

Table 5.4 Diffraction contrast results of the silver specimens.

t_{Ag} (nm)	C(111)		
	300kV	600kV	1000kV
105	0.39	0.54	0.58
67	0.54	0.61	0.74
60	0.62	0.69	0.88
47.5	0.72	0.82	0.97
40	0.92	0.95	1.03
31	0.93	1.03	1.20
27	1.07	1.17	1.21
20	1.07	1.20	1.50

5.3 Variation of contrast with the ratio of the film thickness to the total mean free path (t/λ_T).

All the experimental values of the contrast for the 111 diffraction ring of aluminium for each particular accelerating voltage in Table 5.2 are plotted separately against the appropriate values of (t/λ_T) in Figures 5.1(a), (b), (c) and (d). The variation at 200kV, 400kV and 600kV follows a similar "universal" curve with maximum contrast of about 0.68 at the point where (t/λ_T) $\simeq$ 0.9. However, the variation at 1000kV (see Figure 5.1d) slightly diverges from the "universal"curve B in the region where (t/λ_T) $\geq$ 1. This is probably due to the effect of the high voltage which causes more kinematical diffraction to occur in this region, so that the solid line A, which is the best curve passing through the experimental points, had higher contrast values than the "universal" curve at large values of (t/λ_T).

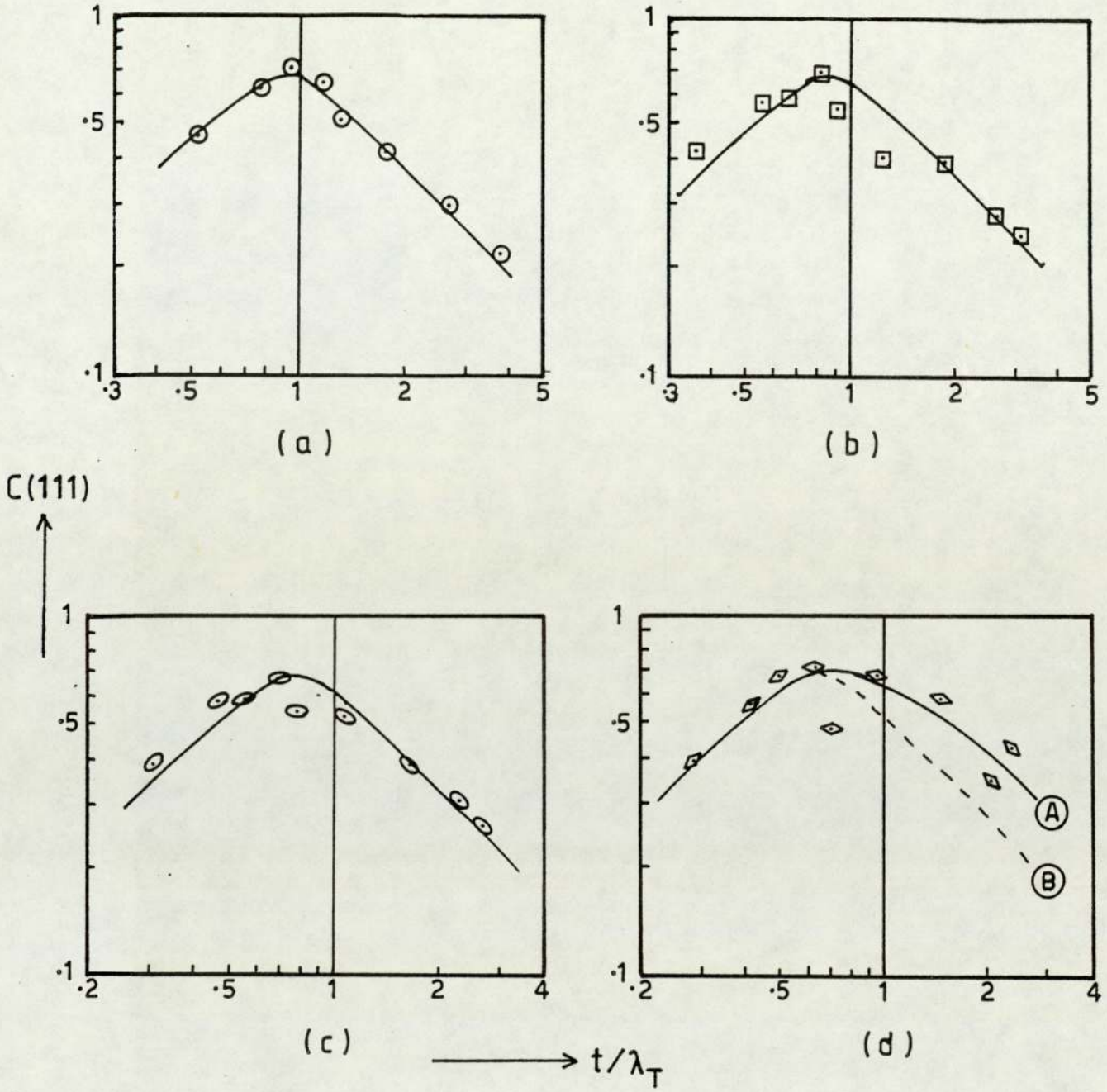

Fig. 5.1 The variation of contrast of the (111) diffraction maxima with the ratio (t/λ_T) for vacuum-evaporated aluminium films.
(a)200kV, (b)400kV, (c)600kV, (d)1000kV.

It was possible to plot the curves in Figure 5.1 on to a single curve, as shown in Figure 5.2. Similar variations of the contrast of the 220 diffraction ring with the ratio (t/λ_T) can be seen in Figure 5.3 with a maximum contrast of about 0.51.

It was relevant to note that the prepared specimens for this work, were supported by the same thickness ($\triangleq$ 5nm) of a carbon film. In comparison to the results found by Halliday (17) (see Figure 5.4), in which the variation of peak contrast with the ratio $(t/\lambda_e) \leqslant 1$, seemed to be different from the results found in this work at that region or, $(t/\lambda_T) \leqslant 1$, where λ_T was always less than λ_e. In single scattering conditions, Halliday (17) maintained that the contrast, $C_s(hkl)$ was given by:-

$$C_s(hkl) = \frac{k_1(\theta)}{k_2(\theta)} \qquad 5.2$$

where $k_1(\theta)$ is the fraction of electrons diffracted per unit specimen thickness per unit solid angle into the peak of the diffraction ring, and $k_2(\theta)$ is a similar fraction for the inelastically scattered electrons. When the specimen contains amorphous material, then $k_1(\theta)$ in Equation 5.2 must be multiplied by $(1-k')$, where k' is the proportion of amorphous material, because the diffracted intensity depends upon the amount of pure crystalline material. However, $k_2(\theta)$ will apparently increase because of the additional elastic scattering of the electrons by the amorphous material in the carbon

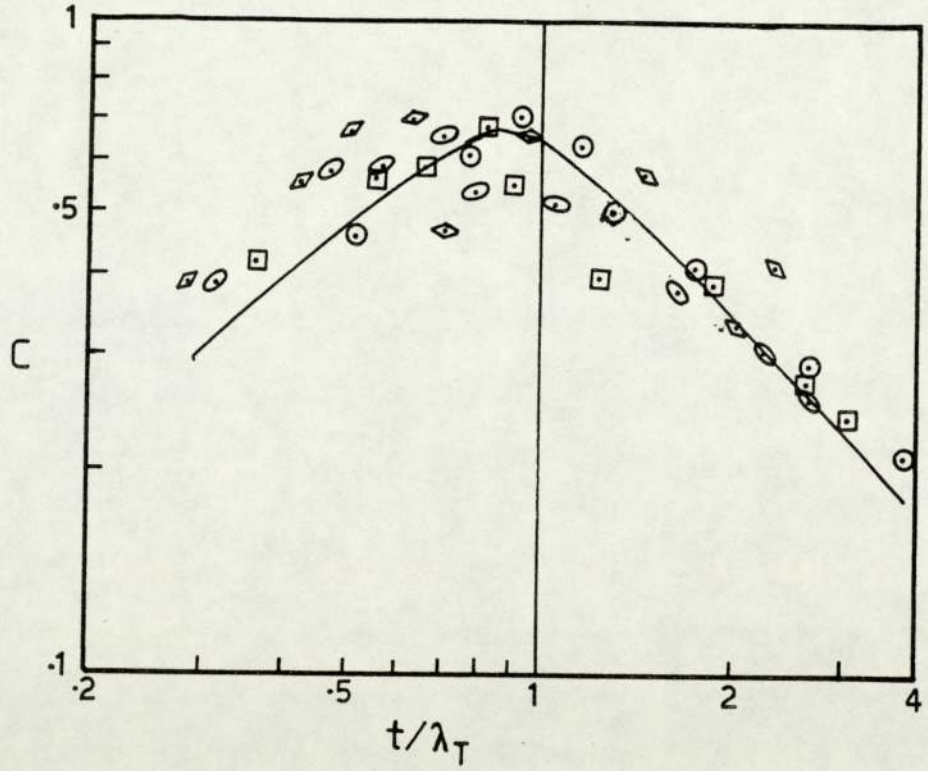

Fig. 5·2 The variation of contrast of the (111) diffraction maxima with the ratio (t/λ_T) for vacuum-evaporated aluminium films.
○,200kV; □ ,400kV; ⬭ ,600kV; ◇ ,1000kV.

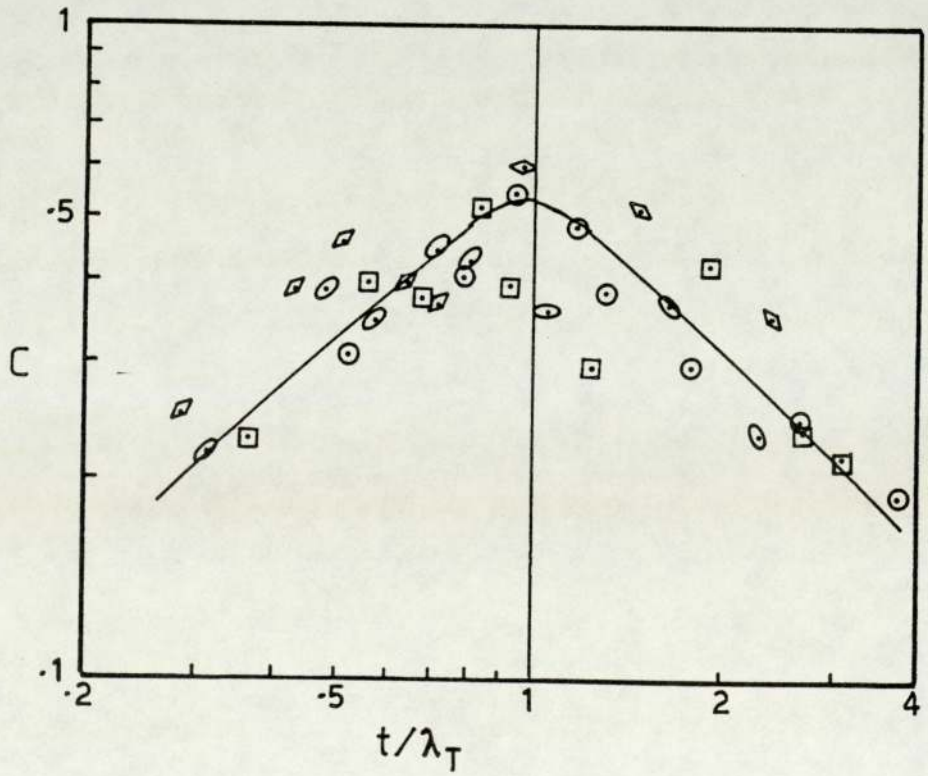

Fig. 5·3 The variation of contrast of the (220) diffraction maxima with the ratio (t/λ_T), for vacuum-evaporated aluminium films.
○,200kV; □ ,400kV; ⬭ ,600kV; ◇ ,1000kV.

support film, in addition to the inelastic scattering by all atoms.

Therefore, the decrease in the contrast under single scattering conditions, as the specimen thickness decreases is probably due to the increase in the proportion of amorphous material k'.

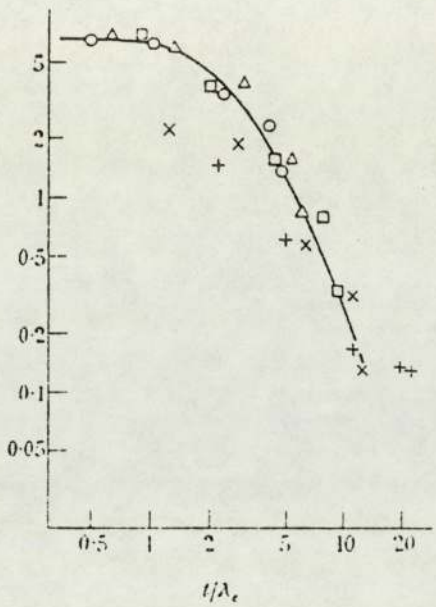

Fig.5.4 Halliday's Figure 6 shows the variation of peak contrast with the ratio (t/λ_e), vacuum evaporated iron, (110) ring.
0,162kV; △,119kV; □,70kV; x,49kV; +,27kV.

Figure 5.5 shows the contrast variation from (110) ∝-iron with the ratio (t/λ_T) for different accelerating voltages. The shape of the curve appeared to be very similar to the shape of the curves found with aluminium

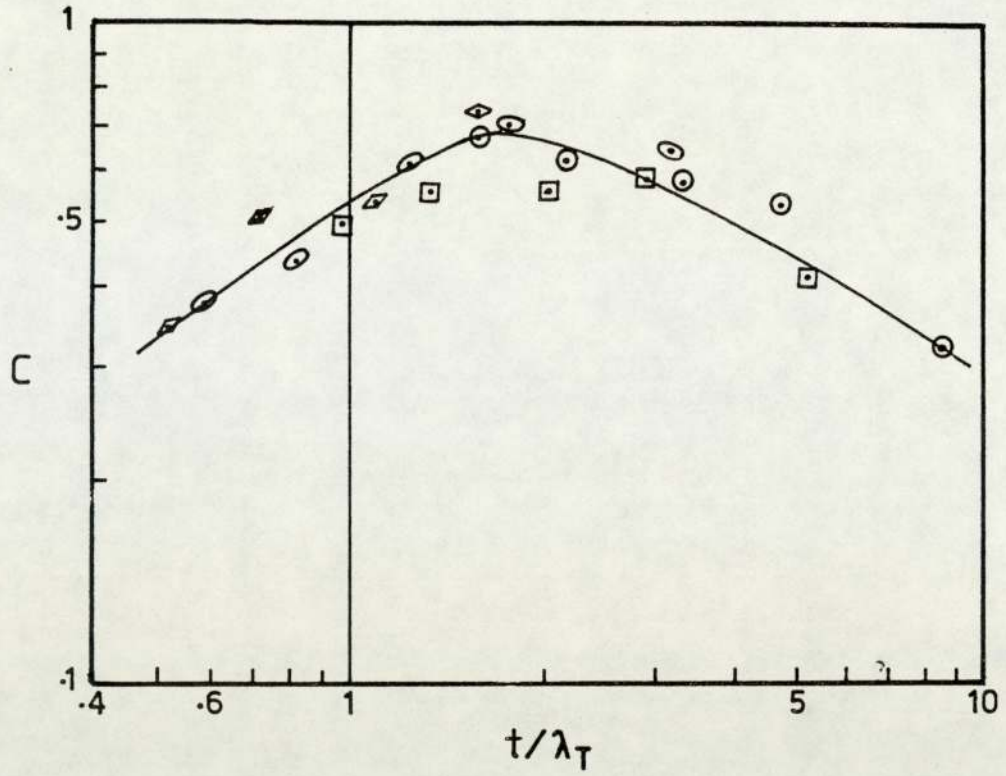

Fig. 5·5 The variation of contrast of the (110) diffraction maxima with the ratio (t/λ_T) for vacuum-evaporated ∝-iron films.
0,100kV; □ ,200kV; ○ ,600kV; ◇ ,1000kV.

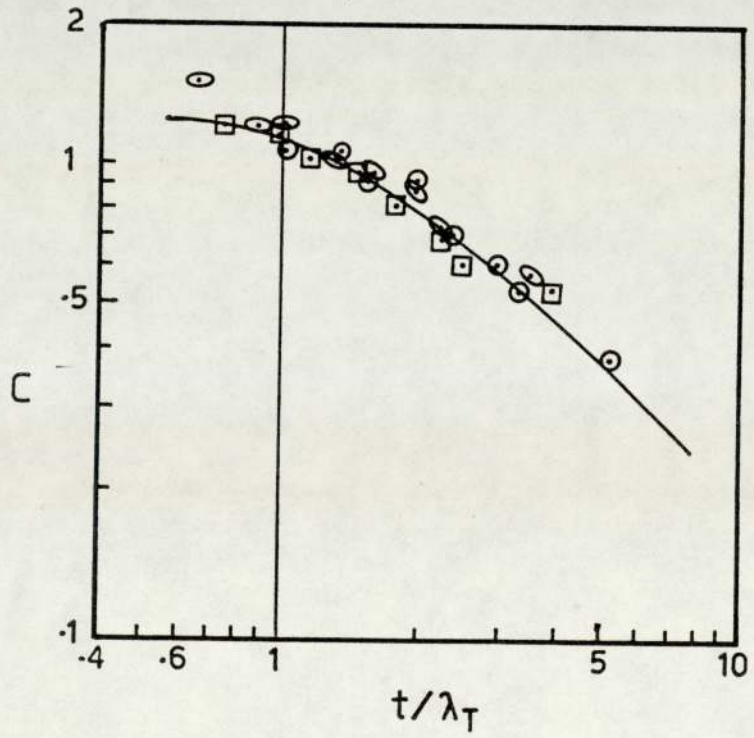

Fig. 5·6 The variation of contrast of the (111) diffraction maxima with the ratio (t/λ_T) for vacuum-evaporated silver films.
0,300kV; □ ,600kV; ○ ,1000kV.

specimens, except for the slight deviation at the maximum contrast. This is probably due to the difference in the mean crystallite sizes, or may be in thickness measurement error. However, the decrease in the contrast under single scattering conditions, as the specimen thickness decreases, confirmed the results found from alumimium specimens.

The values of the contrast from 111 silver diffraction ring for different accelerating voltages, in Table 5.4, were plotted against the ratio of (t/λ_T) in Figure 5.6 . However, it was found that the majority of the points fit very well into a single curve with constant contrast value of about 1.2 when $(t/\lambda_T) \leq 1$.

The contrast variation versus the ratio (t/λ_T) which was obtained from aluminium and α-iron specimens, compared with the results found from silver specimens, indicated that the latter yielded a constant contrast value at all accelerating voltages in the region of single scattering conditions, which was higher than the maximum contrast found from aluminium and α-iron.

The discrepancy in the results shown above, can be understood in relation to Figure 7 of Lenz (22), which shows a graph of the ratio of inelastic to elastic cross sections (σ_i/σ_e) versus the atomic number of the materials as shown in Figure 5.7.

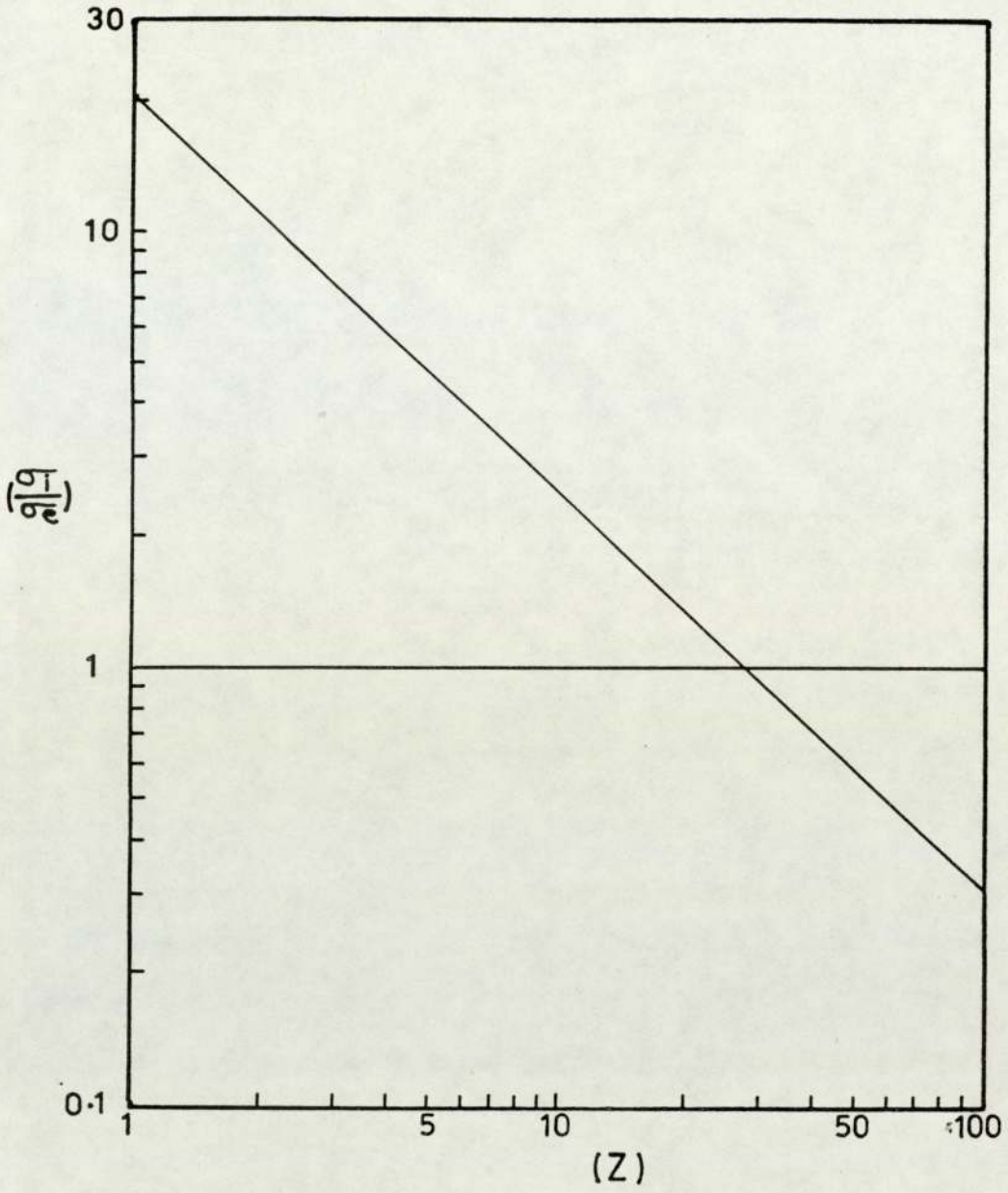

Fig.5.7 Lenz's Figure 7, shows the variation between the ratio of inelastic to elastic cross sections with the atomic number of the materials.

From the above graph, it would appear that the materials which have atomic numbers greater than about 27 will have (σ_i / σ_e) values less than one, or in other words, the elastic atomic scattering will be more than the inelastic scattering. Hence, silver (whose atomic number is 47) will tend to scatter electrons elastically

to a much greater extent than ∝-iron or aluminium, so that the effect of the amorphous material beneath the silver specimens will be less than when using lighter materials.

In order to compare the present results with those based on measuring the peak contrast, measurements were taken and peak contrast C' plotted against (t/λ_T). Very scattered points were obtained for aluminium and ∝-iron, to the degree that curves could not be plotted, whereas smooth curves were obtained for silver as shown in Fig.5.8.

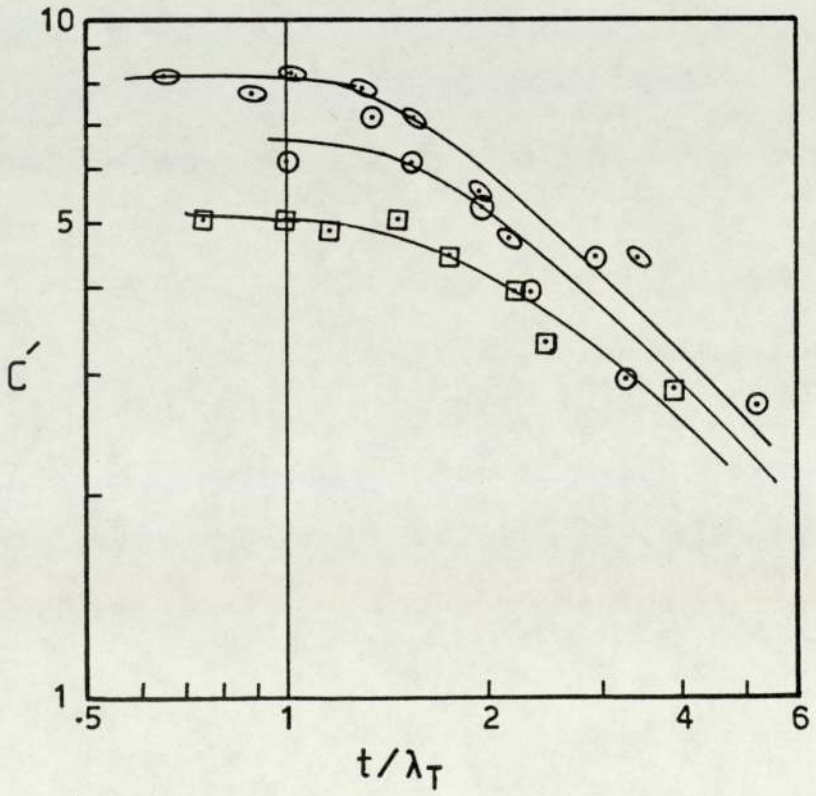

Fig.5.8 The variation of peak contrast of the (111) diffraction maxima with the ratio (t/λ_T) for vacuum-evaporated silver films.
Accelerating voltage (kV): 0,300; □,600; ○,1000.

These curves were not very different from the Halliday (17) curves, apart from the maximum contrast being different for different accelerating voltages. Clearly the peak contrast did not give such a good curve as the integrated contrast mentioned in this work.

5.4 The effect of an amorphous substrate on contrast.

It can be seen from the previous section that the contrast of the diffraction patterns of aluminium and α-iron specimens tended to decrease, under single scattering conditions, as the thickness of the films decreased. This is an important finding which needs more supporting evidence to prove conclusively that the effect of this trend was actually caused by a different proportion k' of amorphous to crystalline material in each specimen. Therefore another experiment was performed to study the effect of the relative proportion of amorphous material on contrast, which involved the preparation of groups of pure aluminium specimens.

The first group consisted of five aluminium specimens 150, 95, 66, 55 and 37 nm thick on electron microscope grids without any supporting substrate. These specimens were prepared by vacuum evaporation onto sheets of mica placed at different distances from the evaporation source, so as to obtain a set of different film thicknesses from the same evaporation. After being scored

into squares, the film was released by gently immersing the mica into water. Some of the floating squares of aluminium film were then transferred to electron microscope grids.

The diffraction patterns were photographed for two different accelerating voltages (300kV and 600kV). The recorded contrast of 111 diffraction ring is shown in the following table:-

Table 5.5 Diffraction contrast results of the unsupported aluminium specimens.

t_{Al} (nm)	Contrast C(111) 300kV	600kV
150	0.29	0.32
95	0.38	0.47
66	0.49	0.57
55	0.48	0.63
37	0.66	0.70

The experimental values of C(111) in Table 5.5, were plotted against the appropriate values of (t/λ_T) in Figure 5.9. It would be seen that the majority of the points lie on a single curve.

However, the shape of the curve in Figure 5.9, for unsupported aluminium specimens was found to have a constant contrast value under single scattering conditions. Obviously, the specimens prepared in this

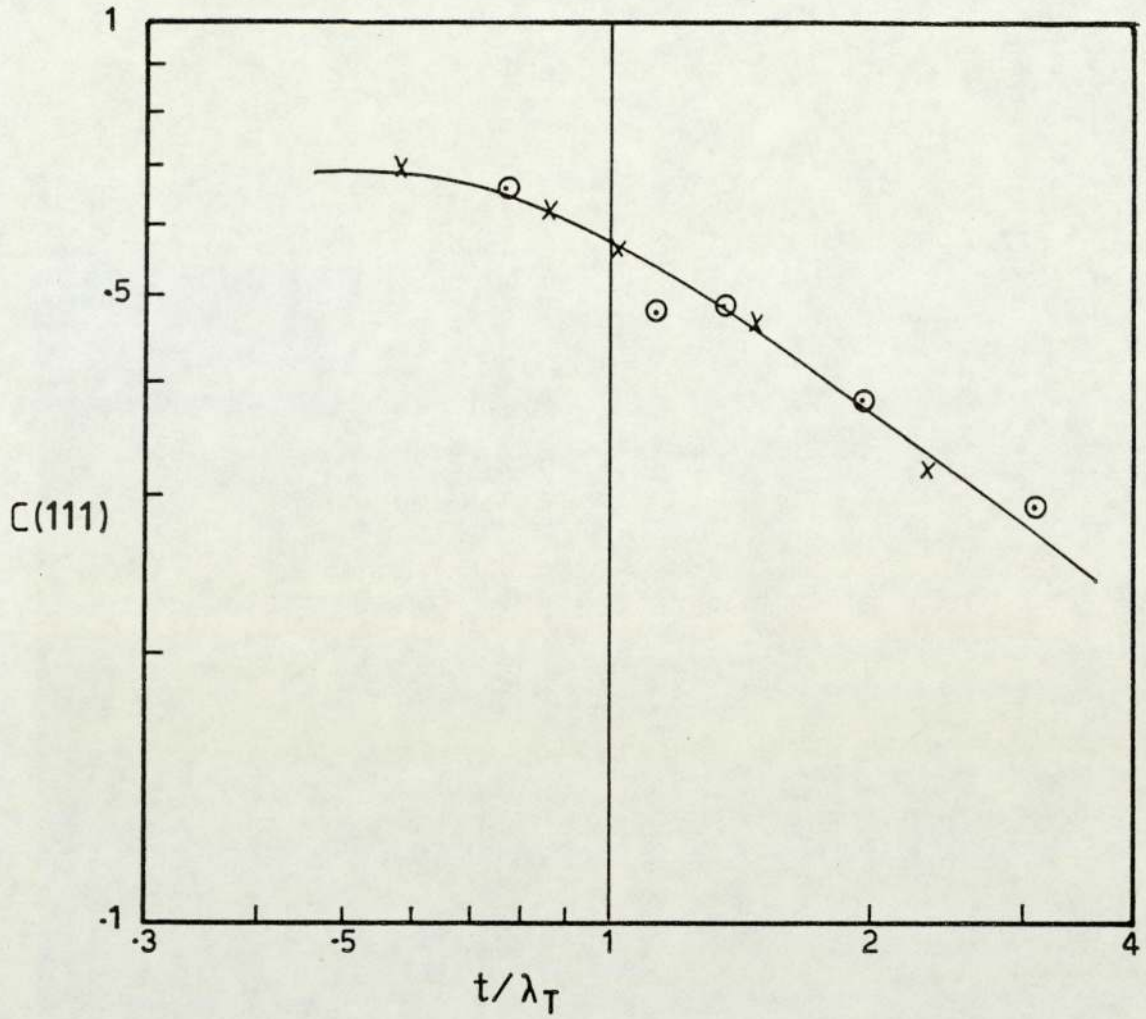

Fig. 5.9 The variation of contrast with the ratio (t/λ_T) for unsupported aluminium films. Accelerating voltage (kV): o,300; x,600.

way should have a constant value k' of the proportion of amorphous material for each reflection.

To compare the above results with those found in the previous section for supported aluminium specimens (see Figure 5.2), at the region of single scattering conditions, it could be explained that the decrease in the contrast as the specimen thickness decreases is due to the increase in the proportion of amorphous material.

This could be further evidence of the effect of the proportion of amorphous material k' on contrast.

The second group of samples consisted of six aluminium specimens of the same film thickness ($\simeq$ 50 nm) supported on different thicknesses of amorphous carbon films. The aim of this experiment was to provide direct evidence concerning the effect of the proportion of amorphous material on the contrast of electron diffraction patterns. In this experiment five electron microscope grids were coated with carbon films of a different thickness (see Section 3.1.1), so that the thickness of the carbon film increased by approximately 5nm in each specimen. Next, an aluminium film was vacuum evaporated directly onto each of the carbon-coated microscope grids. At the same time, a specimen grid without a supporting substrate was coated with an aluminium film from the same evaporation, in the same way as explained in the previous experiment.

Thus the specimens prepared in this way would have an increasing proportion of amorphous material as the thickness of carbon supporter film increases.

The normal procedure for measuring the contrast of the diffraction patterns was followed, and the contrast of the 111 diffraction ring results are shown in Table 5.6.

Table 5.6 Diffraction contrast results of the composite, aluminium and carbon, specimens.

Acc. voltage (kV)	C(111)					
300	0.449	0.4	0.33	0.306	0.28	0.28
600	0.58	0.56	0.48	0.42	0.35	0.32

To examine the effect of the amorphous carbon film on the contrast of the diffraction patterns, a graph of C(111) versus the thickness of carbon film t has been plotted in Figure 5.10.

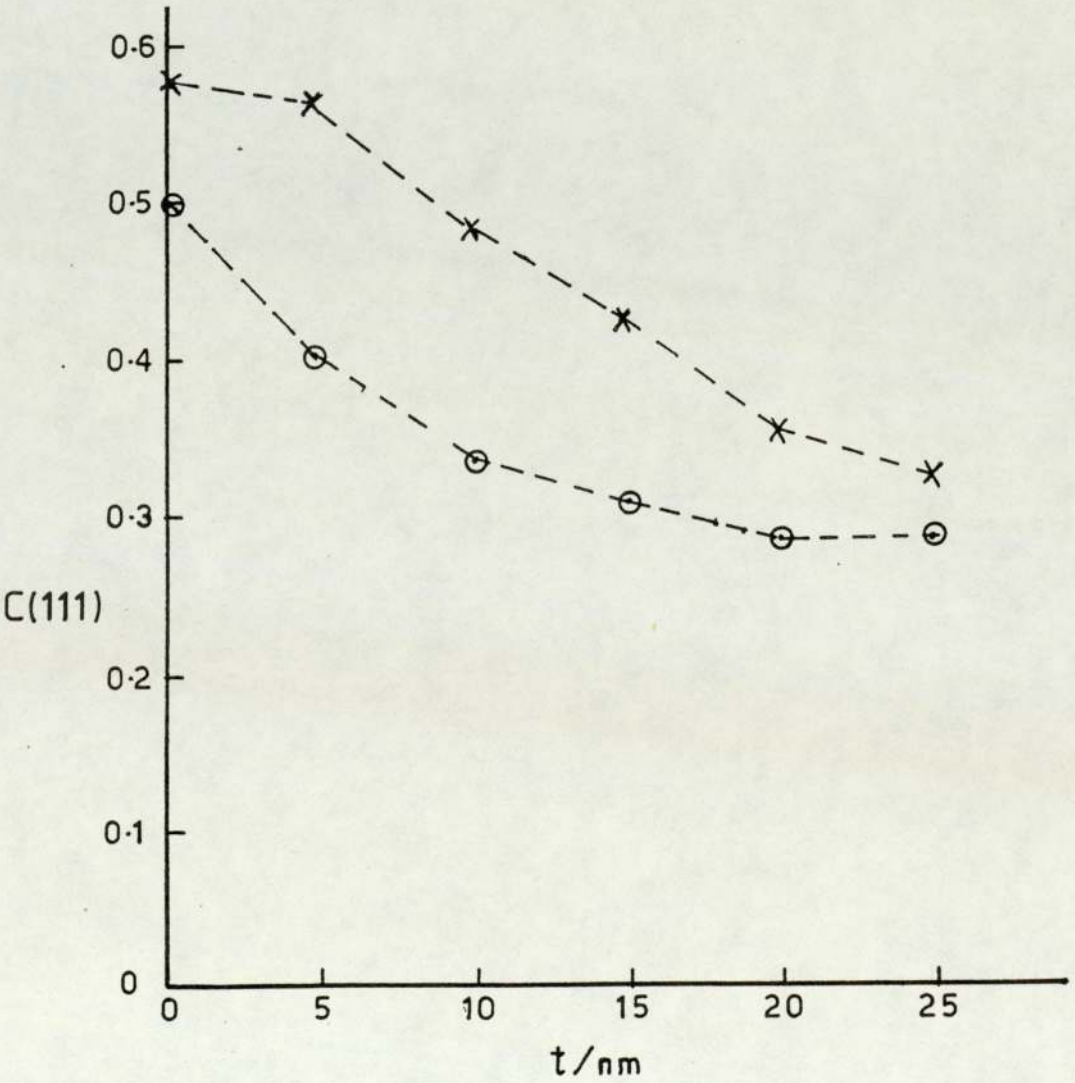

Fig.5.10 The variation of contrast for vacuum-evaporated aluminium film with the thickness of carbon substrate. Accelerating voltage (kV):0,300; x,600.

It was clear that the contrast of the composite specimens tended to decrease as the thickness of carbon film increased.

The contrast of the 111 diffraction ring decreased from 0.5 to 0.28 at 300kV and from 0.58 to 0.32 at 600kV as the thickness of carbon film increased from zero to about 25 nm. This is further confirmatory evidence which shows that the proportion of amorphous material has a strong effect on diffraction contrast.

CHAPTER SIX

DISCUSSION

6.1 Single lamina specimens.

As shown in Chapter Four (Section 4.1) analysis of the results obtained from the diffraction patterns of copper and ∝-iron specimens, aimed to show the validity of the dynamic and kinematic theories of electron diffraction. This is fundamentally important to the proportional analysis of the relative integrated intensities.

Equation 2.22 was used to evaluate the value of n which determines whether the scattering is according to dynamical or kinematical theory.

Figures 4.1 to 4.6 showed the plot of Equation 2.22 for all specimens. From this the n values were measured and listed in Table 4.5. The characteristic feature of these values was explained in terms of the accelerating voltage and specimen thickness only.

Further investigation was carried out to study the scattering process of each pair of rings in order to allow a comparison to be made with the results mentioned above. In this investigation the n value for each pair of rings was calculated by using Equation 2.22. These values were listed in Tables 4.6 and 4.7 for copper and

α-iron respectively.

It was shown from the sample, Figures 4.7 and 4.8, that these n values obtained from the diffraction pairs for most of the specimens increased as their corresponding average Bragg angle $\bar{\theta}$ increased.

This was obviously an indication of the presence of transition from dynamical intensities to kinematical ones throughout the specimen. Such a transition could be illustrated in the following figure (6.1)

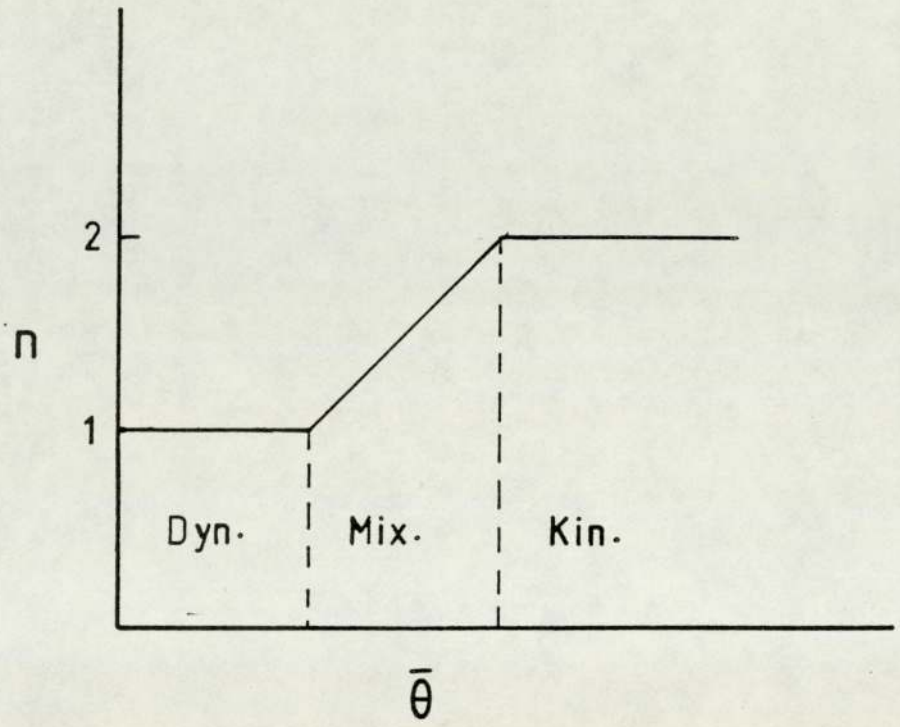

Fig.6.1 Illustration of transition from dynamic to kinematic intensities.

Figure 6.1 shows the possible variation of n values of the diffraction pairs of a particular specimen with their corresponding average Bragg angle $\bar{\theta}$. From these,

three regions could be observed, the dynamical region, the mixed region and the kinematical region. The range of each of these would, of course, depend upon the accelerqting voltage used and the film thickness of the specimen. These are important factors to be considered in addition to the atomic number of the material, crystallite size and the proportion of the amorphous material.

This simple approach shown in the above illustration could be regarded as a guide to compare the present results with the theoretical expectation as we shall see later.

Let us first discuss the shape of the graphs in Figures 4.1 to 4.6. These graphs were the experimental plot of log(J) versus log(Q).

According to the Figure 6.1, the transition from dynamical to kinematical intensites as we move from inner diffraction rings to the outer ones, would reveal significant changes to the shape of the graphs (Figures 4.1 to 4.6). It could then be possible to draw up to three straight lines in each plot. These lines will represent the different scattering processes which might occur between the incident electrons and the atomic structure of the specimen as illustrated in Figure 6.2.

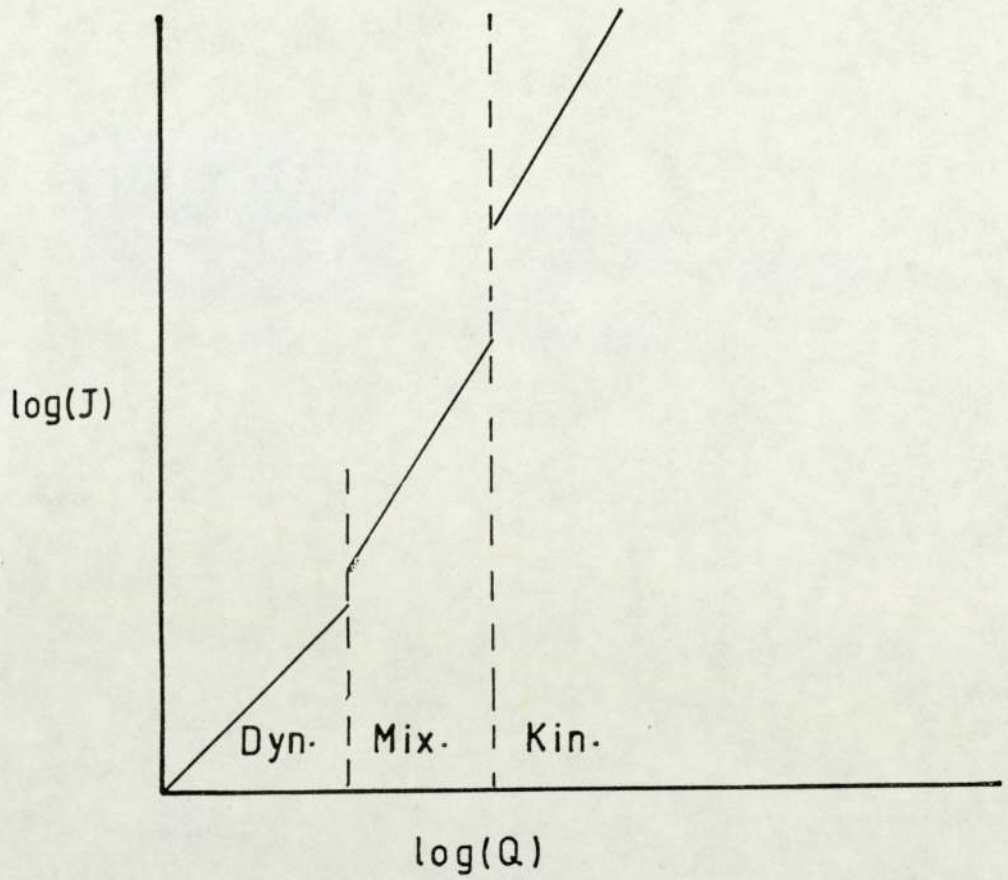

Fig.6.2 An illustration of the possible variation between log(J) versus log(Q).

Figure 6.2 shows an illustration of the possible variation of log(J) versus log(Q) at which three straight lines were drawn to indicate the various scattering processes which might occur between the incident electrons and the atomic material of the metal film. These lines were drawn with slopes of 1, between 1 to 2 and 2 in order to represent the dynamical, mixed and kinematical scattering respectively.

However, Figures 4.1 to 4.6 were the experimental plot of log(J) versus log(Q) at which a best straight line

passing through the experimental points was drawn to give one value of n for each specimen as a whole. This discrepancy could be due to each straight line (see Figures 4.1 to 4.6) being an approximation in comparison with the Figure 6.2. Also most of these lines made intercepts instead of passing through the origin. This may be evidence for the above argument.

All the diffraction pairs of the thinnest specimen of α-iron (Fe_5) showed values of n very close to 2 at 1000kV (see Table 4.7). The plot of log (J) versus log(Q) for this specimen (Fe_5) at 1000kV (see Figure 4.6) showed that a straight line passed nearly through the origin with slope of about 2. This evidence confirms the above argument which showed completely kinematical scattering throughout the specimen.

In practice the number of experimental points were not enough to specify the whole regions which were illustrated in Figure 6.2. Therefore studying the scattering process for each diffraction pair individually is more beneficial than studying the scattering process for each specimen as a whole.

An attempt was made to obtain a numerical estimate of the validity of kinematic and dynamic theories of electron diffraction. This was done by comparing the present results with the theoretical expectation. Equation 2.19 (Chapter 2) was used to calculate the

critical thickness t_c. It is worth remembering that the critical thickness would give equality between kinematical and dynamical intensities and any specimen thicker than t_c might cause the dynamical scattering to dominate.

$$t_c = \frac{v}{2F_e(\theta).\lambda} \qquad 2.19$$

The critical thickness t_c for all diffraction rings of copper and ∝-iron materials at different accelerating voltages were calculated and listed in Table 6.1.

Table 6.1 The calculated critical thickness for copper and ∝-iron material.

Critical thickness t_c/nm							
Copper				∝-iron			
hkl	200kV	600kV	1000kV	hkl	200kV	600kV	1000kV
111	7.8	15.0	22.4	110	8.0	15.3	22.9
200	8.8	17.0	25.5	200	11.0	21.3	31.7
220	12.3	23.7	35.5	211	14.0	27.0	40.2
311	14.5	28.0	41.8	220	16.7	32.1	48.0
400	18.4	35.4	53.0	310	19.5	37.4	55.9
422	23.3	45.0	67.1	321	24.8	47.7	71.2

Referring to the above table, it can be observed that the values of t_c are different for different diffraction rings and at different accelerating voltages. At 200kV for instance the critical thicknesses of copper material vary from 7.8 nm to 23.3 nm as moving from the inner ring 111 towards the outer ring 422 . It can also be

seen from the table that this range of variation is increased as the accelerating voltage increases. Similar variations were observed for ∝-iron material, apart from the slightly higher values of t_c which was obviously due to the slightly lower value of the atomic number of the material.

According to the above table (6.1), any specimen with a thickness which lies between any one of these ranges might scatter the electrons according to both dynamic and kinematic theories. Namely the inner rings might have their intensities given by dynamic theory whilst the outer rings have their intensities given by kinematic theory.

Let us now compare the experimental results obtained from copper and ∝-iron specimens with the theoretical estimation mentioned above.

Table 4.1, Chapter 4, shows the specimen thicknesses of copper and ∝-iron which have been used in this investigation. The thickness range of copper specimens lies between 23.0 nm and 63.7 nm while the range of ∝-iron specimens was between 16.7 nm and 90 nm. The values of n obtained for these specimens were given in Table 4.5. Each value was obtained by plotting Equation 2.22 for each diffraction pattern.

It was noticed from Table 4.5 that for 1000kV, n = 2.04

$\mp$ 0.04, which indicates that, for different thicknesses and materials, both maxima obeyed the kinematical theory. Although, at 200kV, the copper specimens showed a tendency for n to be close to unity, the remainder of n values indicated a mixture of both kinematical and dynamical effects.

However, it was also shown that different values of n for different diffraction pairs were obtained in each specimen (see Tables 4.6 and 4.7). There was a tendency for n, for any particular pair of rings, to increase with increasing voltage. Also, both materials, showed a tendency for n to increase with decreasing specimen thickness (especially when the outer rings related to the strongest one).

The comparison, between the above results and the theoretical estimation mentioned earlier, could be made by the following observations. For example, the thinnest specimen of α-iron showed, at 1000kV, values of n very close to 2 (see Table 4.7) indicating that all maxima in the pattern obey the kinematical theory. The thickness of this specimen is 16.7 nm which is below the range of the critical thicknesses of α-iron at 1000kV (see Table 6.1). The thickest specimen of copper showed, at 200kV, values of n very close to unity (see Table 4.6) indicating that all maxima in the pattern obey the dynamical theory. The thickness of this specimen is above the range of the critical thicknesses at the same

voltage (see Table 6.1).

It was found, from the above examples, that both the experimental results and the theoretical estimation were in agreement.

A similar comparison was made between the experimental results shown in Tables 4.6 and 4.7 with the t_c values shown in Table 6.1. It was found that more than 85% were in agreement.

Therefore, it is possible to consider that the critical thicknesses, shown in Table 6.1 give good approximations for estimating the validity of the dynamic and kinematic theories of electron diffraction for any particular specimen.

6.2 Composite specimens.

Section 4.2 (Chapter Four) shows the analysis of the results, obtained from the diffraction patterns of copper and α-iron composite specimens. The relative integrated intensities produced from the two metal films constituent of the composite specimen were used in this analysis. Only the relative integrated intensity per unit length, from ideal diffraction rings (free from overlap), was measured, so that obtaining smooth diffraction rings was very important in this measurement.

The main object of this investigation was to determine

the thickness ratio of the two films of the composite specimen($\frac{t_1}{t_2}$)from their relative integrated intensity ratio ($\frac{I_1}{I_2}$). It was hoped to achieve this through the use of a theoretical relationship (see Equation 2.9). Equation 2.23 was modified from Equation 2.9 to allow the relative integrated intensity per unit length to be used.

$$\frac{(I_{hkl})_1/(I_{hkl})_2}{t_1/t_2} = \frac{(k_{hkl})_1}{(k_{hkl})_2} \cdot \frac{(d_{hkl})_1}{(d_{hkl})_2} \qquad 2.23$$

The scattering factors $(k_{hkl})_1$ and $(k_{hkl})_2$ of the two films are playing an important part in the above relation.

It was shown theoretically that,under kinematical conditions, the scattering factors ratio (see Equation 2.23) has a constant value for each particular pair of rings. Therefore, a linear relationship between the intensity ratio, of a particular pair of rings, and thickness ratio could only be expected when the diffraction is taking place entirely under kinematical conditions in both layers, or when dynamic theory is operating throughout, (assuming that the crystallite size is constant in both layers).

However, the experimental plots of the intensity ratio against thickness ratio (see Figures 4.9 to 4.11) showed scattered points to the degree that one can not draw a straight line passing through them. But they did show

a tendency for the intensity ratio to increase with an increase in the thickness ratio. These graphs revealed two important facts:- Firstly that the scattering process between the incident electrons and the atomic material was not entirely under kinematical conditions and secondly, that the present form of Equation 2.23 could be used provided that one knows the appropriate value of the scattering factor ratio. This is obviously due to the fact that one does not know whether to use the kinematic or dynamic theory to calculate $(k_{hkl})_1/(k_{hkl})_2$.

The above two cases were given theoretically in Equations 2.26 and 2.27 (Chapter 2) for the kinematic theory and dynamic theory respectively.

In order to examine the applicability of the above two cases, an attempt was made to obtain the n value for each specimen by using Equation 2.28. These values of n were measured for different accelerating voltages (see sample Figures 4.12 to 4.14) and listed in Table 4.16. It was noticed that these values did not show any regular variation with the specimen thicknesses or accelerating voltages and hence not enough information, concerning the scattering processes involved, could be gained. This was partly due to the fact that we considered the two laminae in each composite specimen to have the same crystallite size, which however is not correct (see Table 4.1), but is mainly due to the complex-

ities involved during the scattering processes.

Therefore, it was suggested that in addition to the above two cases (see Equations 2.26 and 2.27), there are some other possible cases regarding $(I_{hkl})_1$ being kinematical and $(I_{hkl})_2$ being dynamical (and vice versa), as shown in the following expressions, and have to be considered.

$$\left[\frac{(I_{hkl})_1/(I_{hkl})_2}{t_1/t_2}\right]_{\frac{Kin}{Dyn}} = \frac{[F_e(\theta)_1]^2.e^{-2D_1}.\lambda.d_1^2P_1}{F_e(\theta)_2.e^{-D}2.d_2^2P_2} \cdot \frac{2v_2\epsilon_2}{v_1^2} \qquad 6.1$$

$$\left[\frac{(I_{hkl})_1/(I_{hkl})_2}{t_1/t_2}\right]_{\frac{Dyn}{Kin}} = \frac{F_e(\theta)_1.e^{-D}1.d_1^2P_1}{[F_e(\theta)_2]^2.e^{-2D}2.\lambda.d_2^2P_2} \cdot \frac{v_2^2}{2v_1\epsilon_1} \qquad 6.2$$

It was shown in Section 6.1 that the critical thicknesses (see Table 6.1) were very good approximations to the limit of the validity of the kinematic and dynamic theory of electron diffraction. Therefore, one could apply this criterion for the composite specimens, and one of the above four cases could be chosen accordingly.

This is only a suggestion. To do so, one would need to prepare a very wide range of thicknesses for each lamina in the composite specimen to allow all cases to be examined several times.

6.3 Electron diffraction contrast.

In Chapter Five the contrast of the diffraction patterns were studied experimentally with the reference to the effect of amorphous substrate on diffraction contrast. The experimental contrast of diffraction rings obtained at several voltages from aluminium, α-iron and silver were measured, as a function of the ratio (t/λ_T). In the present experiments the integrated contrast of diffraction rings, C(hkl), was measured, corresponding to the ratio of the integrated ring intensity divided by the integrated background intensity. According to the values given in Table C.1 (see Appendix) of the total electron mean free paths (λ_T), the specimens' thickness for all materials were prepared in such a way to cover both single and plural scattering conditions.

It was shown in Figures 5.2 and 5.3 the logarithmic plots of contrast C(111) and C(220) of aluminium specimens at different accelerating voltages against the ratio (t/λ_T) respectively. From these figures it was found that the maximum contrast was obtained when $t \simeq \lambda_T$ and in plural scattering conditions or when $t \geqslant \lambda_T$ the contrast rapidly diminished with increasing thickness and decreasing voltage. This result was expected and it was in agreement with the results obtained by previous workers (17). It is well known that if the specimen thickness exceeds the electron mean free path some electrons are scattered more than once on passing through the specimen and in such conditions diffracted electrons are scattered out of the rings into the back-

ground and the contrast deteriorates.

Similar results were obtained from α-iron and silver specimens (see Figures 5.5 and 5.6), apart from the slightly different position of the maximum contrast.

The effect of plural scattering on peak contrast had also been studied theoretically and experimentally by Ellis (18). It was found in his work that the peak contrast decreases rapidly with increasing thickness and decreasing voltage. These findings were very similar to the result obtained in this present work.

However, aluminium and α-iron specimens showed, under single scattering conditions or when ($t/\lambda_T \leqslant 1$), that the contrast decreases with decreasing specimen thickness, whilst the silver specimens showed constant contrast values at the same region. The discrepancy in the above results was explained in terms of the amorphous material constituent. Because the diffraction contrast depends upon the amount of amorphous material in the specimen. The contrast of a diffraction pattern is weak if the specimen contains a high proportion of amorphous material.

It is worth remembering that the specimens prepared for this work, were supported by the same thickness ($\simeq$ 5 nm) of amorphous carbon film. This will tend to increase the proportion of amorphous material as the specimen thickness

decreases. So that it is not surprising to see the contrast, under single scattering conditions, having decreasing values as the specimen thickness decreases.

The silver specimens did not seem to be affected by the relative amount of the proportion of amorphous material, under single scattering conditions (see Figure 5.6). This case was explained in relation to Figure 7 of Lenz (22) (see Figure 5.7), which shows that the silver (atomic number 47) will tend to scatter electrons elastically to a much greater extent than α-iron or aluminium. So that the effect of the proportion of amorphous material on silver is comparatively much lower than on aluminium and α-iron.

The amount of the elastic scattering between the incident electrons and silver specimens were well observed in the diffraction patterns which showed high peak intensity in comparison to the background intensity. This case was demonstrated in Figure 5.6, which shows higher maximum contrast in comparison with the Figures 5.2 and 5.5 of aluminium and α-iron specimens.

Let us compare the present results with those results obtained by previous investigators. Halliday (17) had plotted the peak contrast against (t/λ_e) as shown in Figure 5.4. The shape of the curve seemed to have constant contrast value in the region of single scattering conditions. The specimens used by this investigator were

unsupported iron films. Thus one should expect for unsupported films that the peak contrast should approach the value $\frac{k_1(\theta)}{k_2(\theta)}$ of Equation 5.2. It can be seen that the present results showed similar trends, under plural scattering conditions, and the contradiction under single scattering conditions would most likely be due to the different ways of preparing the specimens.

Also Halliday (17) replotted the peak contrast obtained by Ellis (18) against (t/λ_e) in order to compare his results with other investigators. The plots were very similar to Halliday's curves. The specimen materials prepared by Ellis (18) were thallium chloride and aluminium which had been evaporated onto collodion films as a supporting membrane. Unfortunately the range of voltages and specimen thicknesses used in this work were not enough to explore the region of single scattering conditions. Scattered experimental points were reported by Ellis (18) near this region indicating the effect of the supporting membrane.

The effect of the relative proportion of amorphous material was noticed by other investigators. Mukherjee and Row (23) have suggested that there is an optimum thickness for an evaporated aluminium film which will give a pattern of maximum contrast. It is also believed that with very thin films the diffraction rings may be broadened owing to a decreased crystallite size which would produce a proportionately greater background and hence poorer contrast.

Comparison of the present resuts with those based on measuring the peak contrast C' did not give such good curves (see Figure 5.8) as the integrated contrast mentioned in this work. This is probably due to the effect of the crystallite size, mentioned in the above paragraph.

Further investigations were made to provide more supporting evidence to prove conclusively that, under single scattering conditions, the effect of decreasing contrast, as the specimen thickness decreases, was actually caused by a different proportion of amorphous material k' for different specimens.

In this investigation the specimen material aluminium was chosen because it has a lower atomic number than α-iron or silver and according to Lenz's figure 7 (see Figure 5.7) the diffraction contrast produced from such material will not diminish the effect of the proportion of amorphous material as we have seen previously with silver specimens (see Figure 5.6).

In the first part of this experiment, five pure aluminium specimens were prepared without any supporting substrate. It can be seen from Figure 5.9 that the variation of contrast C(111) obtained from these specimens with the ratio (t/λ_T) showed constant contrast values in the region of single scattering conditions. The experimental points of Figure 5.9 at different accelerating voltages

fit very well onto a single curve which is very similar to Halliday's curves.

A comparison between the contrast results obtained from unsupported aluminium specimens mentioned above with those obtained from supported aluminium specimens on carbon substrate, shown in Figure 5.2, will reveal that the decrease of diffraction contrast under single scattering conditions is actually due to the effect of the proportion of amorphous material.

In the second part of this investigation, six aluminium specimens of the same film thickness ($\simeq$ 50 nm) were supported on different thicknesses of amorphous carbon films. In this experiment direct evidence concerning the effect of the proportion of amorphous material on diffraction contrast was provided. A film of aluminium was evaporated in one stage to ensure that the same conditions relating to specimen thickness, crystallite size and amount of amorphous content prevailed. The voltages used and the thickness of aluminium film were chosen in order to ensure single scattering conditions.

It was shown in Figure 5.10 that the diffraction contrast results obtained from the 111 diffraction ring tended to decrease as the thickness of carbon substrate increased.

This was further confirmatory evidence which showed

that the proportion of amorphous material has a strong effect on diffraction contrast under single scattering conditions.

Figure 5.10 also reveals that the diffraction contrast for both supported and unsupported specimens depends upon the accelerating voltage, which confirms the results found by previous investigators (17, 18).

However, the proportion of amorphous carbon substrate might also have an effect on the proportional analysis of the composite specimen, shown in Chapter Four (Section 4.2), since the composite specimen consisted of two laminae of different materials supported on amorphous carbon substrate. It is much better if one uses self-supporting laminae specimens by evaporating the two films separately on sheets of mica and then transferring them onto electron microscope grids. In this way, there will be no need for the carbon substrate and it will also avoid the reheating of the first lamina during the evaporation of the second lamina, as experienced by the usual method.

6.4 Practical implications of the results.

On the limit of validity of kinematic and dynamic theories for single lamina specimens, the present criterion given in Equation 2.19 was confirmed by the experimental results. Figure 6.3 shows the variation of t_c with accelerating voltage for both copper and α-iron

specimens, assuming (2.19) and using $F_e(\theta)$ values in Appendix A, respectively. The latter were obtained from the values of $f(\theta)$ given by Ibers (29). A similar criterion was given by Blackman (8) in terms of Fourier coefficients and has been used by other investigators (17) who show that fully dynamical conditions should arise for the hkl reflection when:-

$$t \geq \frac{\pi V}{4F_e(\theta).\lambda} \qquad 6.3$$

When the thickness of the lamina (t) is reduced or when the accelerating voltage is increased so that Equation 6.3 is no longer satisfied, then n (see Equation 2.22) gradually increases from one to two. It is important to note that the values of n, in the present work, were obtained from the relative integrated intensity ratios of the diffraction pairs. The advantage of this method is to eliminate the effect of the proportion of amorphous material in the specimen or the amorphous substrate, and also the attenuation factor e^{-kt}.

The disadvantage of this method is that one may be comparing two diffraction rings formed as a result of two different scattering processes, especially when a very high voltage is used, since the variation of t_c is very large (see Figure 6.3 at 1000kV).

It can also be noticed, for the same reason as mentioned above, that the use of very high voltages would give uncertainty to the validity of kinematic and dynamic

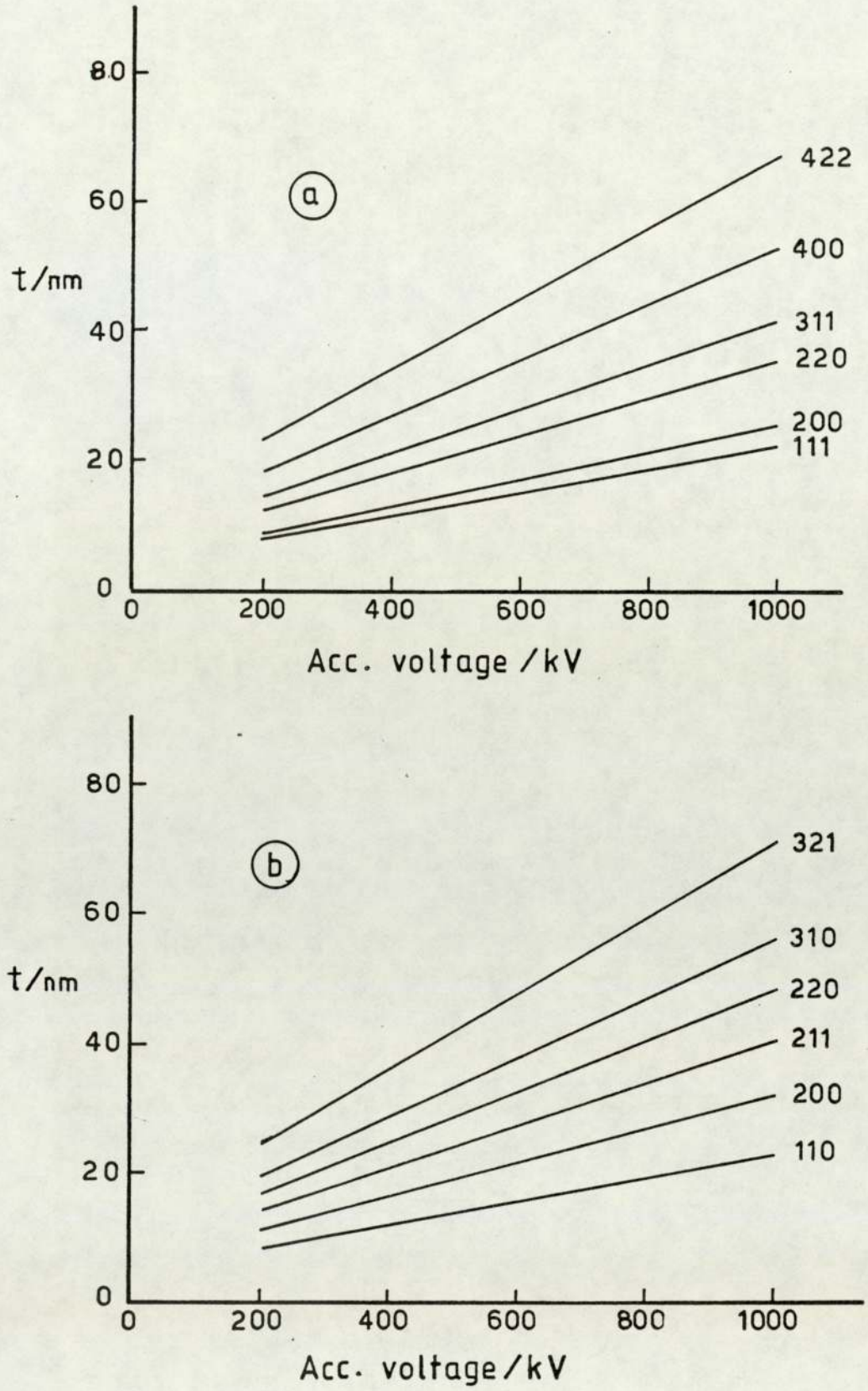

Fig. 6·3 Theoretical variation of the critical thickness (t_c) with accelerating voltage for (a) copper specimens and (b) ∝-iron specimens.

theories for a wide range of specimen thicknesses.

Regarding the relative intensity of the diffraction rings, it was shown that the proportion of amorphous material (k') has an effect, through the term ($1-k'$), on the peak ring intensity as already described. This was consistent with the form of the experimental curves relating the contrast and the ratio (t/λ_T) under single scattering conditions. It is, therefore, difficult to make comparison between these relative intensities and those predicted by kinematical and dynamical theories as used by some of the previous workers. In order to compare the variation of the relative ring intensities, for various operating voltages and crystallite size, with values predicted by the kinematical and dynamical diffraction theories, the specimens must have constant crystalline composition and in this case we should expect constant contrast results under single (kinematic) diffraction conditions as shown in Figure 5.9 (Chapter 5).

The electron diffraction contrast method can also be used to predict, quantitatively, the onset of kinematical or dynamical diffraction conditions. This was done by measuring the appropriate thicknesses of α-iron specimens at the maximum contrast (see Figure 5.5). These values were found to be 21.3 nm, 40.6 nm and 57.8 nm for 200kV, 600kV and 1000kV respectively. Comparison between these thicknesses and those given theoretically by Equation 2.19 (see Figure 6.3b), despite changes in the proportion

of amorphous material and crystallite sizes, were found to be in good agreement.

The variations of the relative integrated intensities of the diffraction rings from composite polycrystalline specimens with the thicknesses of the lamina showed that the qualitative form of Equation 2.23 is correct. But, unfortunately, little success is recorded in obtaining, quantitatively, the thickness ratio of the laminae from their relative integrated intensity ratio (15, 16) in spite of the importance of this technique in many applications, such as in the formation of the oxide layers on steel. From the present results, and from the results obtained by previous workers, one could conclude that the main difficulty in using this technique is to determine the mechanism of the scattering processes involved, especially under dynamical diffraction conditions.

According to the experimental results obtained in this investigation, and to explore the region of dynamical diffraction conditions, one might suggest some essential modifications in the experimental work which might minimise the problems arising from the scattering processes. These are (a) only use specimens of constant crystalline composition as already described (i.e. self-supporting specimens), (b) use low voltages, so as to maintain dynamical diffraction conditions and, on the other hand, to reduce the region of mixed diffraction

conditions, (c) ensure that laminae thicknesses in the composite specimen are greater than the total electron mean free path (λ_T), and finally, (d) the relative integrated intensities should be measured from rings which are completely free from overlap.

Appendix A

The structure factor for electrons $F_e(\theta)$.

The structure factor for electrons is the sum of all the scattered amplitudes from all the atoms in the unit cell, which is obviously related to the atomic scattering factor $f_e(\theta)$. The latter describes the result of the interference effects which take place within the structure of the atom. The atomic scattering factor ($f_e(\theta)$) is similar to that in X-ray scattering ($f_x(\theta)$). But in X-ray, the scattering is produced from interaction with atomic electrons and, therefore, $f_x(\theta)$ depends only on the number of electrons (z) in the atom whilst in electron scattering the interaction with the potential field of the nucleus, so that the atomic scattering factor for electrons depends on $(z-f_x(\theta))$.

However, to calculate the structure factor $F_e(\theta)$ for electrons one must take into account the different phases of electron waves scattered by N atoms in a unit cell and is the same as the structure factor for X-rays (24) except that one writes $f_e(\theta)$ instead of $f_x(\theta)$ in the expression for the structure factor, thus:-

$$F_e(\theta) = \sum_{i=1}^{N} f_e(\theta)_i \, e^{-2\pi i(hx_i+ky_i+lz_i)} \qquad A.1$$

where x_i, y_i and z_i are the fractional co-ordinates of atom i.

If the lattice has a centre of symmetry, we can leave out the sine terms, and if the atoms are the same kind, thus Equation A.1 reduces to

$$F_e(\theta) = f_e(\theta)_i \sum_{i=1}^{N} \text{Cos } 2\pi(hx_i+ky_i+lz_i) \qquad A.2$$

Consider face-centred cubic lattices, the four lattice points per unit cell are located at 000, ½½0, 0½½ and ½0½. Substituting these values in Equation A.2, we get:-

$$F_e(\theta) = f_e(\theta)\,[\,1+\text{Cos}\,\pi(h+k)+\text{Cos}\,\pi(k+l)+\text{Cos}\,\pi(l+h)\,] \qquad A.3$$

Thus in FCC lattices reflections occur only when h, k, and l are either all even or all odd and have the value,

$$F_e(\theta) = 4f_e(\theta) \qquad A.4$$

otherwise $F_e(\theta) = 0$ and the reflections are absent.

For body centred cubic lattices, the lattice points co-ordinates are 000, ½½½. The reflections which do occur only when h+k+l is even and have the value

$$F_e(\theta) = 2f_e(\theta) \qquad A.5$$

otherwise $F_e(\theta) = 0$ and the reflections are absent.

According to the data given in Table II, Appendix E (25), the graphs shown in Figure A.1 were plotted, between the atomic scattering factors and (Sin θ/λ). Knowing the interplanar spacing d, (Sin θ/λ) could be calculated

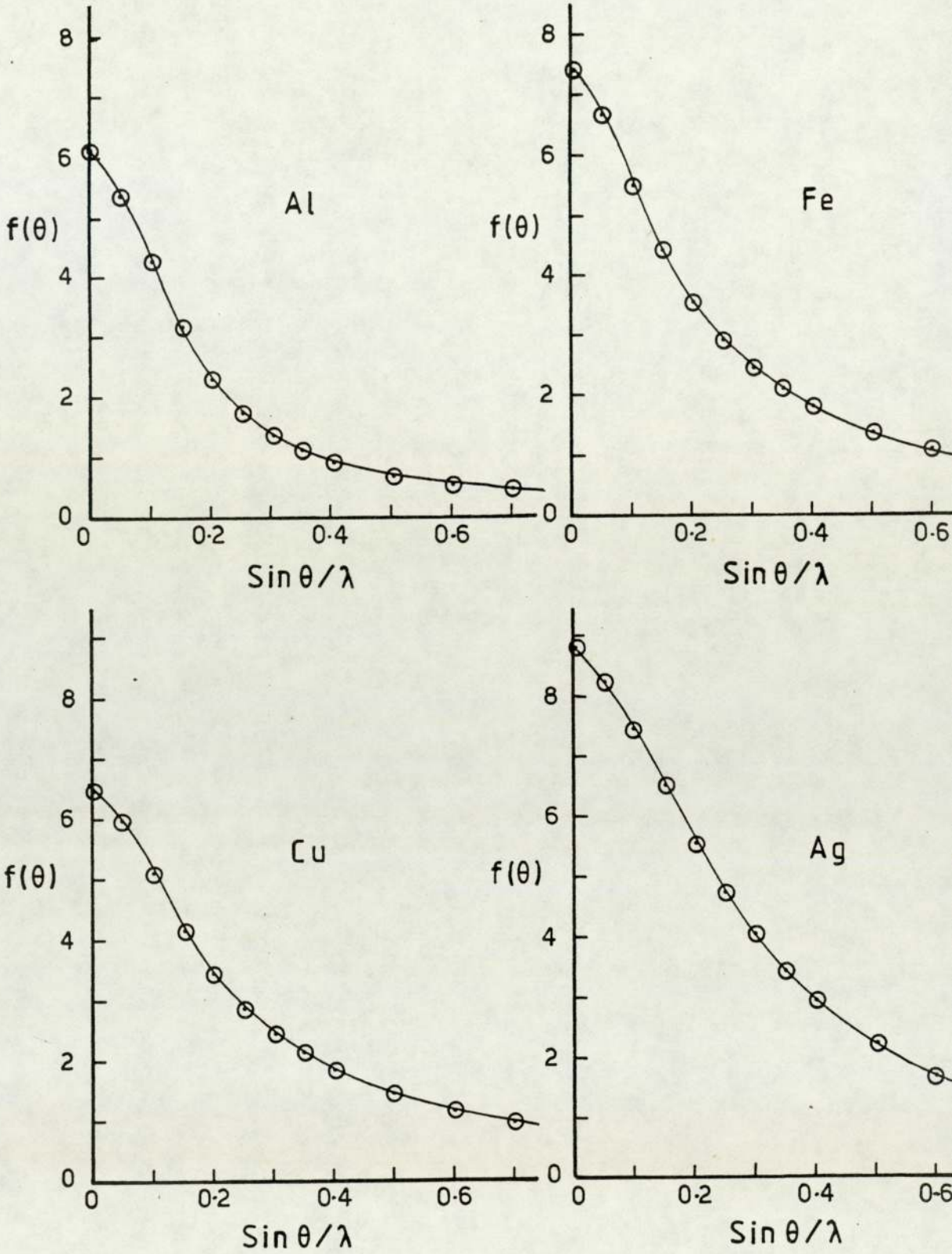

Fig. A.1 The variation of f(θ) with the ratio (Sinθ/λ) for aluminium, ∝-iron, copper and silver.
Data given in Table II, Appendix E (25).

from Bragg's equation for each set of planes in each material. By using the graphs in Figure A.1 in conjunction with the equations A.4 and A.5, one could calculate the structure factor $F_e(\theta)$.

The structure factors for Cu, Ag and ∝-iron materials were calculated and listed in Table A.1

Table A.1 The calculated values of structure factors $F_e(\theta)$ in Å units.

hkl	$F_e(\theta)$		hkl	$F_e(\theta)$
	Cu	Ag		∝-Fe
111	12.08	21.60	110	5.9
200	10.64	19.40	200	4.26
220	7.64	14.00	211	3.36
311	6.48	11.28	220	2.82
222	6.20	11.08	310	2.42
400	5.12	9.20	321	1.9
331	4.80	8.08		
420	4.52	7.80		
422	4.04	6.80		

Appendix B

The Debye-Waller factor e^{-D}.

The atoms in crystalline materials are not in practice fixed at their lattice points, but they are vibrating about their sites with certain amplitudes. Usually the amplitude of these thermal vibrations increase as the temperature of the crystalline material increases. Therefore, the diffracted wave intensities are reduced by the so-called Debye-Waller factor.

The Debye-Waller temperature factor can be calculated from the following relation (26)

$$e^{-D} = e^{-B(\frac{\sin\theta}{\lambda})^2} \qquad \text{B.1}$$

and

$$B = \frac{1.14 \times 10^4}{Ma\ \Theta}\left[\Phi\left(\frac{\Theta}{T}\right).\ \frac{T}{\Theta} + \frac{1}{4}\right] \qquad \text{B.2}$$

where Θ is the characteristic temperature (27),

Ma is the atomic mass,

T is the absolute room temperature and

$\Phi\left(\frac{\Theta}{T}\right)$ is the Debye function.

From the data given in Table 5.2.2B (26), a graph was drawn between $\Phi\left(\frac{\Theta}{T}\right)$ versus $\left(\frac{\Theta}{T}\right)$ as shown in Figure B.1. Using this figure, the value of $\Phi\left(\frac{\Theta}{T}\right)$ could be found for any particular value of $\left(\frac{\Theta}{T}\right)$. Substituting these values together with the other parameters in Equation B.2, the B value, for each material, could be found. The

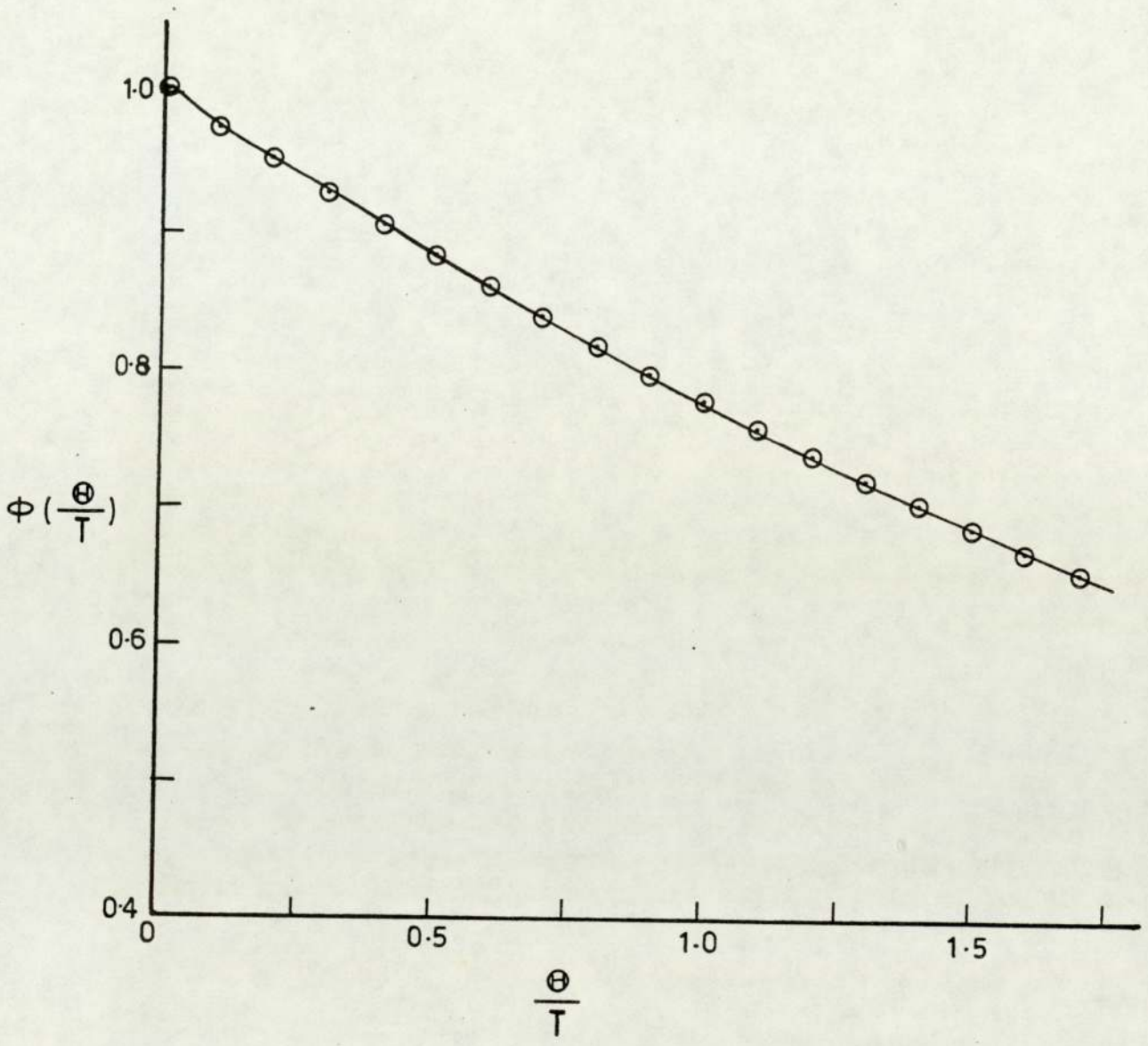

Fig. B.1 The variation of the Debye function $\Phi(\frac{\Theta}{T})$ with the ratio $(\frac{\Theta}{T})$.

Data given in Table 5.2.2B (26).

Debye-Waller temperature factor (e^{-D}) could then be calculated, for each reflection, by knowing the d value and substituting the value of B in Equation B.1.

The Debye-Waller factors for Cu, Ag and ∝-iron were calculated and listed in Table B.1.

Table B.1 The calculated values of Debye-Waller temperature factors.

hkl	e^{-D}		hkl	e^{-D}
	Cu	Ag		∝-Fe
111	0.970	0.970	110	0.981
200	0.960	0.960	200	0.962
220	0.920	0.921	211	0.944
311	0.890	0.893	220	0.926
222	0.884	0.890	310	0.909
400	0.844	0.859	321	0.874
331	0.822	0.822		
420	0.813	0.813		
422	0.775	0.781		

Appendix C.

Calculation of the electron mean free paths.

The electron mean free paths for elastic, λ_e, and inelastic, λ_i, scattering were calculated by using Figures 2 and 7 from Lenz (22), as shown in Figures C.1 and C.2. Figure C.1 shows the variation of the transparency thickness ($\rho\lambda_e$) with the accelerating voltage for both light and heavy materials, where ρ is the density of the material. Figure C.2 shows the variation between the ratio of inelastic to elastic cross sections (σ_i/σ_e) with the atomic number of the materials.

For a given material, (σ_i/σ_e) could be found by using the graph in Figure C.2 and, hence, the value of λ_e can be determined. From the inverse relationship between cross sections and mean free paths, one can calculate λ_i. Total electron mean free path λ_T can then be calculated using the following equation:-

$$\frac{1}{\lambda_T} = \frac{1}{\lambda_e} + \frac{1}{\lambda_i} \qquad \text{C.1}$$

For example, the elastic mean free paths for copper at 100kV. From Figure C.1, the transparency thickness for copper at 100kV is equal to

$$\rho\lambda_e = 1.73 \times 10^{-5} \text{ gm/cm}^2$$

$$\therefore \lambda_e = \frac{1.73 \times 10^{-5}}{\rho} \text{ cm}$$

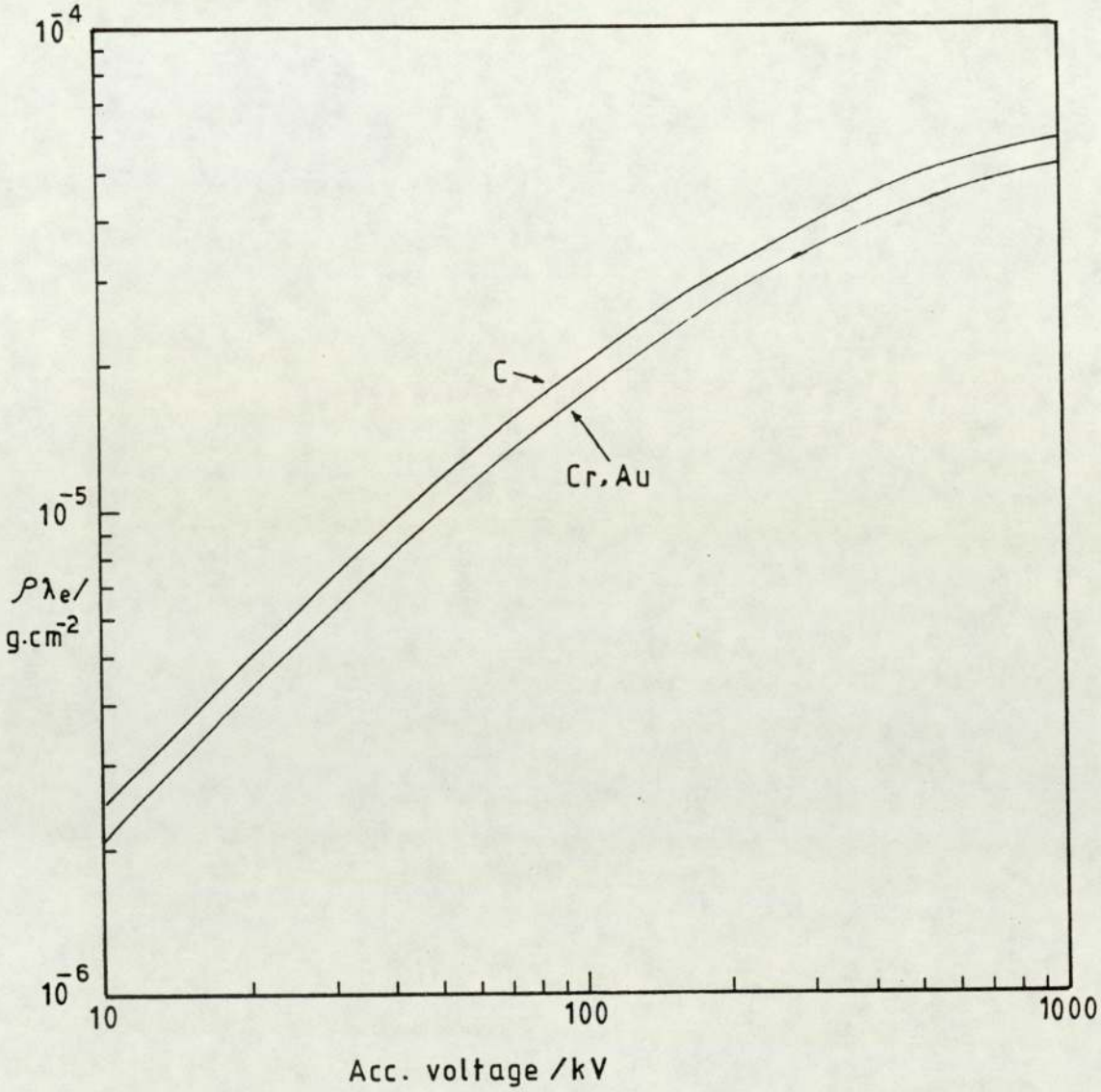

Fig.C.1 The variation of the transparency thickness ($\rho\lambda_e$) with the accelerating voltage (22).

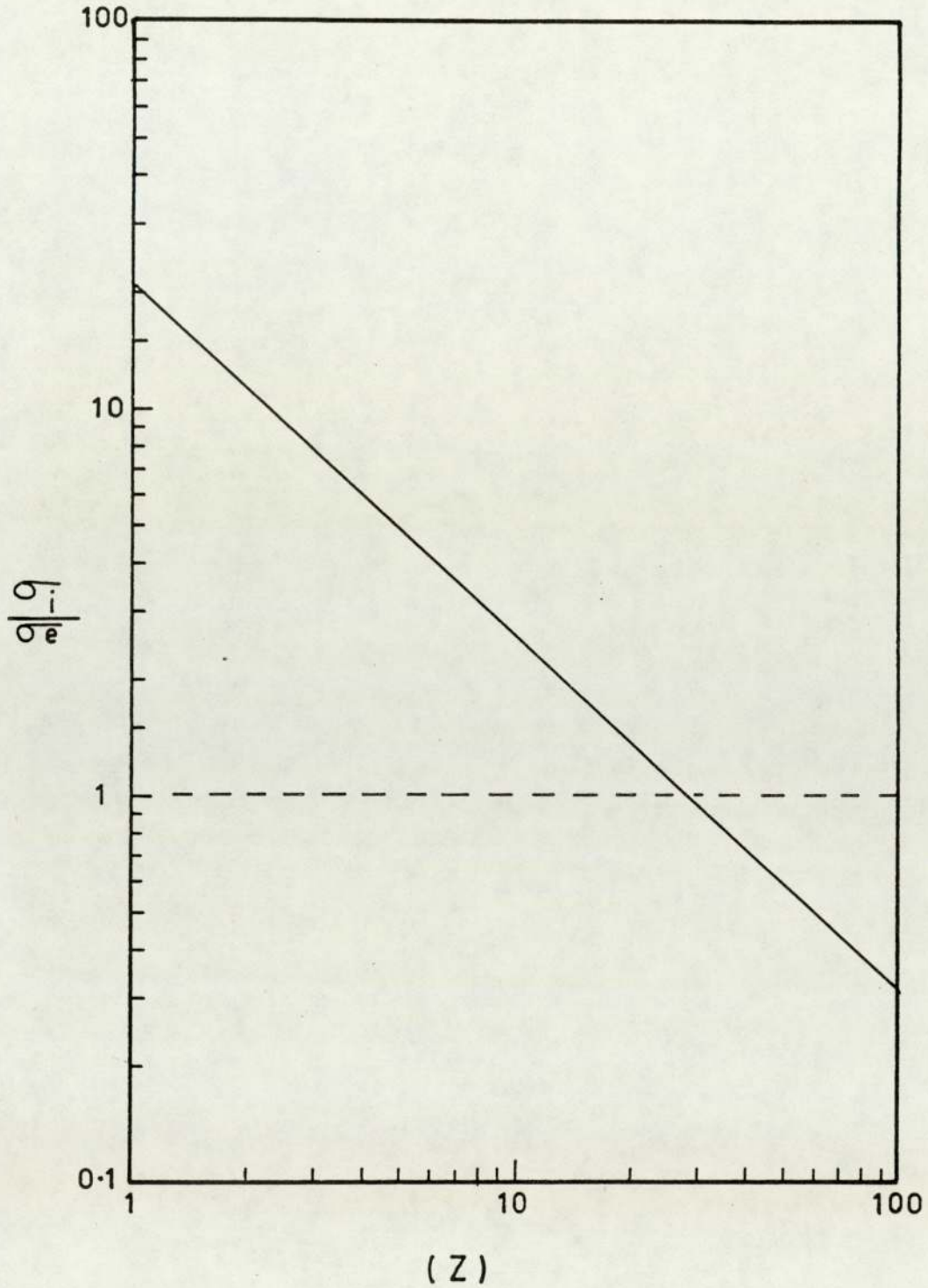

Fig.C.2 The variation between the ratio of inelastic to elastic cross sections with the atomic number of the material (22).

Using Figure C.2, the ratio of (σ_i/σ_e) for copper (At.No.29) is equal to 0.95 and from the inverse relationship below

$$\frac{\sigma_i}{\sigma_e} = \frac{\lambda_e}{\lambda_i} \qquad \text{C.2}$$

we can calculate λ_i, where

$$\lambda_i = \left(\frac{\sigma_e}{\sigma_i}\right) \lambda_e \qquad \text{C.3}$$

And finally from Equation C.1, one can calculate the total electron mean free path λ_T for any particular voltage.

Table C.1 shows the calculated values of λ_T for aluminium, α-iron and silver at different accelerating voltages.

Table C.1 The calculated values of total electron mean free path, λ_T, at different accelerating voltages.

λ_T (nm)			Acc. voltage (kV)
Al	α-Fe	Ag	
247	10.7	10.2	100
389	17.3	16.6	200
487	21.6	20.4	300
549	24.7	23.0	400
642	28.1	26.9	600
716	32.1	30.7	1000

Appendix D

A paper published by Journal of Physics on the effect of amorphous material on the contrast of electron diffraction patterns.
J.Phys. vol.15,(1982), P: 267-274.

The effect of amorphous material on the contrast of electron diffraction patterns

R A A Al-Mausawe and T F J Quinn
Department of Physics, The University of Aston in Birmingham, Birmingham B4 7ET, UK

Received 7 August 1981

Abstract. Experiments have been performed to study the contrast of transmission electron diffraction patterns. The effect of film thickness, accelerating voltage and amorphous content are discussed. Diffraction patterns, from vacuum-evaporated thin films of aluminium, α-iron and silver, on carbon-coated grids were obtained by using an electron microscope with high accelerating voltages (100 to 1000 kV). Experimental measurement of the contrast from all materials showed that: (i) in plural scattering conditions, the contrast diminished with increasing thickness and decreasing voltage; and (ii) the highest contrast is obtained when the thickness equals the mean free path. This is in agreement with the results of previous workers. However, in the region where the mean free path is greater than the film thickness, aluminium and α-iron showed that the contrast decreased as the film thickness decreased, whilst silver remained at its maximum contrast. It seems probable that, with very thin films, the lines may be broadened owing to a decreased crystallite size, and furthermore, the increase in the proportion of the amorphous material will produce greater background, which reduces the contrast.

1. Introduction

When an electron beam passes through a thin polycrystalline material, an electron diffraction pattern is obtained, which consists of a number of rings from the elastic scattering of electrons in the crystalline region. Electrons which are inelastically scattered in non-crystalline regions form a diffuse background.

The contrast of the electron diffraction pattern may be defined as the ratio of the integrated intensity of the ring to the integrated intensity of the background. Ellis (1952) and Halliday (1960) have used the concept of peak contrast, which is defined as the ratio of the peak intensity of the ring to the background intensity at the peak point of the ring. It is convenient in practice to measure the peak contrast but probably not accurate, because of the possible variation in the crystallite size from specimen to specimen.

Ellis (1952) used films of thallium chloride and aluminium supported by collodion films on copper meshes. The results showed a decrease in peak contrast with the specimen thickness for different voltages, the effect of increasing voltage being to increase the contrast at any given film thickness. Halliday (1960) suggested the idea of combining thickness and voltage through the use of the electron mean free path and developed a universal empirical formula relating the peak contrast in plural scattering conditions C_p

0022-3727/82/020267 + 08 $02.00

to that in single scattering conditions C_s by

$$C_p = C_s/[1 + 0.06(t/\lambda_p)^2 + 0.016(t/\lambda_p)^3] \quad (1)$$

where λ_p is the electron mean free path (which is almost equal to the mean free paths for elastic, λ_e, and inelastic, λ_i, electrons in the case of iron). If they are unequal, λ_p should be replaced by the smaller mean free path. Clearly, $C_p \simeq C_s$ for $(t/\lambda_p) \leqslant 1$ (according to equation (1)), where t is the thickness. The contrast of a diffraction pattern is weak when the specimen contains a high proportion (k') of amorphous material, so that one should expect, in very thin specimens or in single scattering conditions, that the contrast would decrease as k' increases.

The objectives of this paper are: (i) to repeat Halliday's work for iron and extend it to higher voltages (to explore the region of $(t/\lambda_T \leqslant 1)$, where λ_T is the total electron mean free path and is given by

$$\frac{1}{\lambda_T} = \frac{1}{\lambda_e} + \frac{1}{\lambda_i} \quad (2)$$

(ii) to extend Halliday's work for other materials, e.g. aluminium and silver, which are low and high atomic numbers in comparison with iron; and finally, (iii) to investigate the effect of the amorphous carbon film on the contrast.

2. Experimental details

Sets of different film thicknesses from pure α-iron, aluminium and silver have been prepared by vacuum evaporation directly on to carbon-coated microscope grids. Different thicknesses were made from the same amount of each material by placing the grids on a ladder which had movable steps to provide a variable distance from the evaporating source. Facilities were provided for making a sharp step on a clean microscope slide, for measuring the evaporated film thickness. The film thicknesses were measured using the conventional techniques for multiple beam interferometry.

Diffraction patterns were obtained using an electron microscope in the selected area electron diffraction mode of operation at different accelerating voltages up to 1000 kV, the size of the diffraction aperture being chosen to give rings of uniform intensity. Four photographs for different exposure times were taken of the diffraction patterns from a selected specimen to enable a calibration curve of 'exposure versus density of blackening' to be deduced for each batch of photographic films used.

The density variations were measured with an automatic recording microdensitometer, in which the intensity of light passing through the micrograph was compared with that passing through a standard glass wedge (along which the density of blackening varied from minimum to maximum with known gradient).

Finally, dark-field techniques were used to measure the crystallite size, in which an electron microscope was used with accelerating voltage of 100 kV in 'a selected area diffraction mode of operation' to produce a diffraction pattern for each specimen. Then the beam was tilted until a part of the 111 diffraction ring came into view through the small objective aperture. The microscope was then operated in the normal manner and an image of bright crystals in a dark field being formed. A photograph of this image was then taken. Many of the images of the crystallite in each photograph have been measured

with the aid of a graph paper and viewer, and the average value of the crystallite size could be found after allowance for the magnification which has been used (table 6).

3. Experimental results

Table 1 shows the film thicknesses of aluminium, α-iron and silver specimens prepared by vacuum evaporation on to glass microscope slides. These thicknesses had been measured by using a multiple-beam inferometer.

Table 1. Specimen thicknesses.

Material	Film thickness (Å)								
Aluminium	1680	1450	1040	680	500	450	360	300	200
α-Iron	900	500	350	230	167				
Silver	1050	670	600	475	400	310	270	200	

The electron mean free paths for elastic (λ_e) and inelastic (λ_i) scattering have been calculated by using figures 2 and 7 from Lenz (1954). Lenz's figure 2 shows the variation of the transparency thickness ($\rho\lambda_e$) with the accelerating voltage, where ρ is the density of the material, and Lenz's figure 7 shows the variation between the ratio of inelastic to elastic cross-sections (σ_i/σ_e) with the atomic number of the materials and from the inverse relationship between cross-sections and mean free paths one can calculate λ_i. The total electron mean free path λ_T can then be calculated using equation (2). The appropriate values of λ_T are given in table 2.

Table 2. Total electron mean free path λ_T(Å) in aluminium, α-iron and silver for different accelerating voltages.

	Accelerating voltage (kV)					
Material	100	200	300	400	600	1000
Aluminium	247	389	487	549	642	716
α-Iron	107	173	216	247	281	321
Silver	102	166	204	230	269	307

The electron diffraction contrast C for the strongest rings from the diffraction patterns of aluminium, α-iron and silver have been measured by using their micro-densitometer traces, calibration graphs and the definition of the contrast in equation (3)

$$C(hkl) = \Sigma pw/\Sigma BW \tag{3}$$

where Σp is the 'exposure' (intensity multiplied by the exposure time) of the peak, w is the width of the peak at the half peak point, ΣB is the 'exposure' of the background, and

Table 3. Diffraction contrast results of the aluminium specimens.

Accelerating voltage (kV)							
200		400		600		1000	
$C(111)$	$C(220)$	$C(111)$	$C(220)$	$C(111)$	$C(220)$	$C(111)$	$C(220)$
—	—	0.246	0.22	0.262	0.25	0.42	0.36
0.214	0.195	0.278	0.245	0.309	0.24	0.34	0.34
0.295	0.248	0.388	0.43	0.385	0.37	0.58	0.53
0.418	0.3	0.395	0.3	0.519	0.36	0.667	0.61
0.502	0.39	0.55	0.4	0.54	0.42	0.467	0.37
0.642	0.49	0.69	0.52	0.66	0.45	0.71	0.4
0.71	0.55	0.59	0.38	0.59	0.35	0.67	0.46
0.62	0.41	0.57	0.4	0.58	0.39	0.56	0.39
0.46	0.31	0.42	0.23	0.39	0.22	0.39	0.25

Table 4. Diffraction contrast results of the α-iron specimens.

Accelerating voltage (kV)							
100		200		600		1000	
$C(110)$	$C(211)$	$C(110)$	$C(211)$	$C(110)$	$C(211)$	$C(110)$	$C(211)$
0.32	0.27	0.41	0.34	0.64	0.51	—	—
0.53	0.37	0.58	0.46	0.7	0.55	0.74	0.52
0.57	0.4	0.56	0.45	0.61	0.45	0.54	0.37
0.62	0.44	0.56	0.38	0.44	0.29	0.51	0.36
0.67	0.35	0.5	0.3	0.38	0.26	0.35	0.18

Table 5. Diffraction contrast results of the silver specimens for $C(111)$.

Accelerating voltage (kV)		
300	600	1000
0.39	0.54	0.58
0.54	0.61	0.74
0.62	0.69	0.88
0.72	0.82	0.97
0.92	0.95	1.03
0.93	1.03	1.2
1.07	1.17	1.21
1.07	1.2	1.50

Table 6. Crystallite sizes of the specimens measured by dark-field techniques.

Material	Crystallite size ε(Å)								
Aluminium	340	230	200	154	166	138	180	156	122
α-Iron	107	93	94	79	67				
Silver	$\simeq$ 200 for all specimens								

W is the width of the background. Tables 3, 4 and 5 show the contrast results of aluminium, α-iron and silver specimens for different accelerating voltages.

4. Discussion and analysis

All the experimental values of the contrast for the (111) diffraction ring of aluminium for each particular accelerating voltage in table 3 are plotted against the appropriate values of (t/λ_T) in figure 1. The variation at 200, 400, 600 and 1000 kV follows a similar 'universal' curve with maximum contrast of about 0.68 at the point where $(t/\lambda_T) \simeq 0.9$.

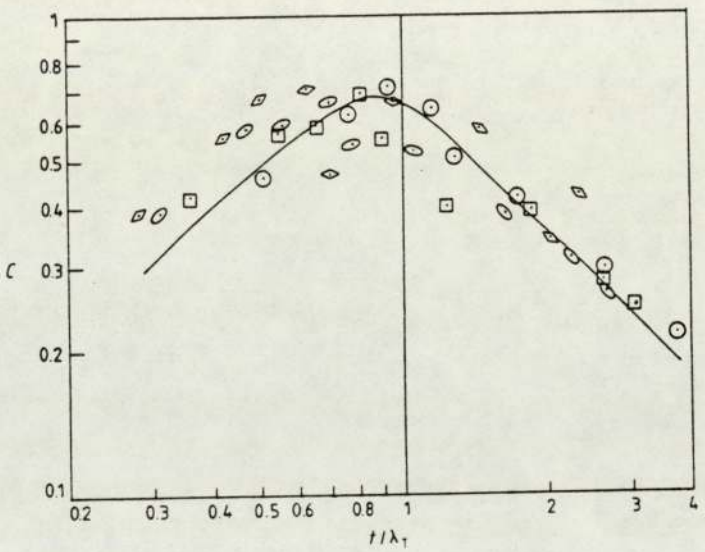

Figure 1. The variation of contrast of the (111) diffraction maxima with the ratio (t/λ_T) for vacuum-evaporated aluminium films. Accelerating voltage (kV): ○, 200; □, 400; ⬭, 600; ◇, 1000.

Similar variation of the contrast of the (220) ring with the ratio (t/λ_T) can be seen in figure 2, with a maximum contrast of about 0.51. The results found by Halliday (1960) (in which the variation of contrast with the ratio of (t/λ_p) showed constant maximum in the region where $(t/\lambda_p) \leqslant 1$) seem completely different in the region of single scattering conditions, or, $(t/\lambda_T) \leqslant 1$, where λ_T is always less than λ_p. The decrease in the contrast, in single scattering conditions, as the specimen thickness decreases, is probably due to the increase in the proportion of amorphous material, k'.

In single scattering conditions, Halliday (1960) maintains that the contrast, $C_s(hkl)$ is given by

$$C_s(hkl) = k_1(\theta)/k_2(\theta) \tag{4}$$

where $k_1(\theta)$ is the fraction of electrons diffracted per unit specimen thickness per unit solid angle into the peak of the diffraction ring, and $k_2(\theta)$ is a similar fraction for the inelastically scattered electrons. It is relevant to note that the specimens prepared for this experiment were supported by the same thickness of carbon film, so that one should

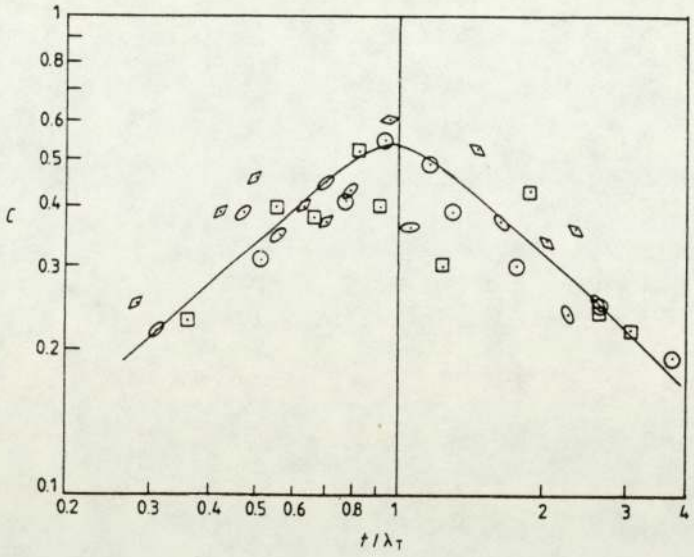

Figure 2. The variation of contrast of the (220) diffraction maxima with the ratio (t/λ_T) for vacuum-evaporated aluminium films. Accelerating voltage (kV): ○, 200; □, 400; ⬭, 600; ◇, 1000.

expect $k_1(\theta)$ in equation (4) to decrease as the specimen thickness decreases because the diffracted intensity depends upon the amount of pure crystalline material. However, $k_2(\theta)$ will apparently increase because of the extra elastic scattering of the electrons by the amorphous material in the carbon support film, in addition to the inelastic scattering by all atoms.

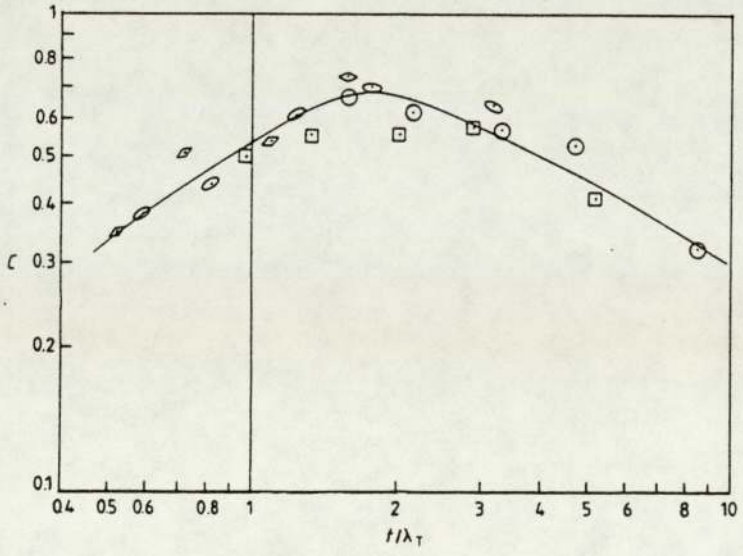

Figure 3. The variation of contrast of the (110) diffraction maxima with the ratio (t/λ_T) for vacuum-evaporated α-iron films. Accelerating voltage (kV): ○, 100; □, 200; ⬭, 600; ◇, 1000.

Therefore, the contrast under single scattering conditions will decrease from its maximum as the proportion of the amorphous material, k', increases.

Figure 3 shows the variation of the contrast from (110) α-iron with the ratio (t/λ_T) for different accelerating voltages. However, the variation appeared very similar to the results found in aluminium, except for the slightly different position at the maximum contrast. This is probably due to the difference in mean crystallite sizes or to the different amounts of amorphous material. Hence, the contrast results of α-iron films confirm the results found for aluminium.

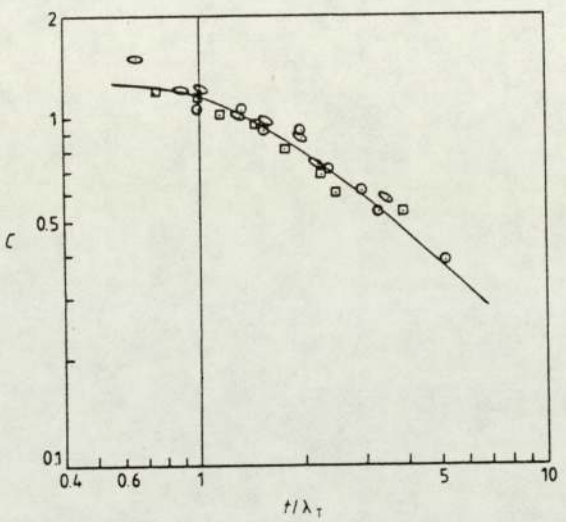

Figure 4. The variation of contrast of the (111) diffraction maxima with the ratio (t/λ_T) for vacuum-evaporated silver films. Accelerating voltage (kV): ○, 300; □, 600; ⬭, 1000.

The contrast results values from the (111) silver diffraction ring for different accelerating voltages are plotted against the ratio of (t/λ_T) in figure 4. The contrast variation shows that the majority of the points fit on to a single curve with constant maximum of about 1.2 when $(t/\lambda_T) \leqslant 1$.

Comparison of the contrast variation versus the ratio (t/λ_T) obtained from aluminium and α-iron specimens with the results obtained from silver specimens (see figure 4) indicates that the latter seem to be constant for all accelerating voltages in the region of single scattering conditions. That constant contrast was higher than the maximum contrast found for aluminium and α-iron.

The discrepancy in the results shown above can be understood in relation to figure 7 of Lenz (1954), which shows a graph of the ratio of inelastic to elastic cross-sections (σ_i/σ_e) versus the atomic number of the materials. From the graph it would appear that the materials which have high atomic number (i.e. more than about 27) will have values of (σ_i/σ_e) less than one or, in other words, the elastic scattering with the atoms will be more than the inelastic scattering. Hence, silver (which has atomic number 47) will tend to scatter electrons elastically to a much greater extend than iron or aluminium, so that the effect of the amorphous material in the silver specimens will be less than in the lighter materials.

To compare with Halliday (1960), measurements have been made and peak contrasts (C') plotted against (t/λ_T). Very scattered points were obtained for aluminium and α-iron, whereas smooth curves were obtained for silver. These were not very different from the Halliday curves, apart from the maximum contrast being different for different accelerating voltages as shown in figure 5. Clearly, the peak contrast does not give such a good curve as the integrated contrast mentioned in this paper.

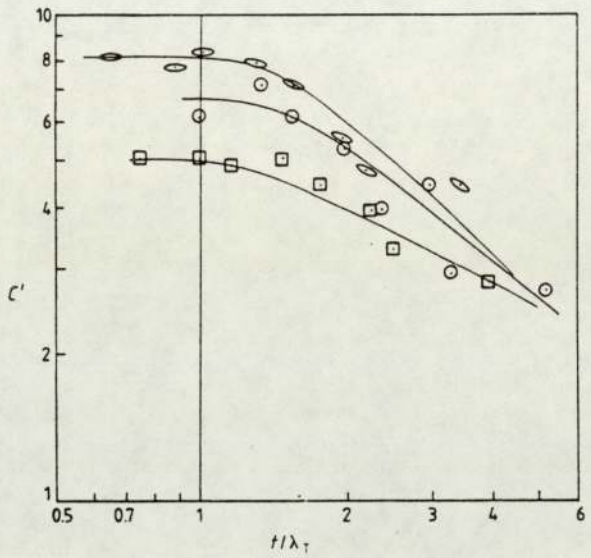

Figure 5. The variation of peak contrast of the (111) diffraction maxima with the ratio (t/λ_T) for vacuum-evaporated silver films. Accelerating voltage (kV): ○, 300; □, 600; ⬭, 1000.

However, it is important to mention that there are some improvements when one plots (C'_{Al}/ε) and (C'_{Fe}/ε) versus (t/λ_T). These plots were not very different from the integrated contrast measurements reported in this paper, apart from the maximum contrast being different for different accelerating voltages.

Acknowledgments

The authors wish to acknowledge the assistance of Mr R Keen in much of the experimental work. Thanks are also due to Birmingham University for permission to use the High Voltage Electron Microscope. One of us (R Al-Mausawe) would also like to thank the Iraqi Embassy for the financial support.

References

Ellis S G 1952 *Phys. Rev.* **87** 970
Halliday J S 1960 *Proc. R. Soc.* A **254** 30
Lenz F 1954 *Z. Naturf.* **9a** 185

REFERENCES.

1. L. de Broglie, A tentative theory of light quanta. Phil.Mag., vol.47(1924), P: 446-458

2. G.P.Thomson, Diffraction of cathode rays. Proc. Roy. Soc., vol.A125(1929), P: 352-370.

3. S.Shirai, Intensity of cathode rays scattered by KCl. Proc. Phys. Math. Soc. Japan, Vol.15(1933), P: 420-427.

4. T.Tol and L.S.Ornstein, Measurements of the relative intensity of electron diffraction patterns of copper, silver and gold. Physica, vol.7(1940), P: 685-696.

5. S.Lennander, Measurements of electron diffraction intensities by means of Geiger counter. Experimental determination of relative values of the atomic factor for gold, silver and aluminium Ark. Fys., vol.8(1954), P: 551-613.

6. S.Kuwabara, Intensity variations of electron diffraction patterns from metal films of various thicknesses. J.Phys. Soc. Japan, vol.10(1955), P: 416 .

7. S.Kuwabara, Variation of electron diffraction intensity with crystal size. J.Phys. Soc. Japan, vol.12(1957), P: 637-643.

8. M.Blackman, On the intensities of electron diffraction rings. Proc. Roy. Soc. vol.173(1939), P: 68-82.

9. Z.G.Pinsker, Chapter 8 of "Electron Diffraction". Butterworths Scientific Publications, London 1953.

10. I.I.Yamzin, The scattering of electrons by atoms. Verification of the laws of atomic scattering of electrons by the intensities of electronograms. Trudy Inst. Krist. Akad. Nauk., vol.5(1949), P: 69-112.

11. K.Kimoto, Study on the intensity anomaly of electron diffraction powder patterns from minute silver crystallites. J.Phys. Soc. Japan, vol.8(1953), P: 762-768.

12. N.H.Dawe, Proportional analysis of composite polycrystalline specimens of copper and aluminium by electron diffraction. M.Sc. Project (1974), Aston University.

13. G.Boxley Proportional analysis of composite polycrystalline specimens of copper and aluminium by electron diffraction. M.Sc. Project (1976), Aston University.

14. T.J.Liddicoat, Proportional analysis of composite polycrystalline specimens of copper and aluminium by electron diffraction. B.Sc. Project, Aston University.

15. T.F.J.Quinn and N.H.Hayes, Proportional analysis of composite polycrystalline specimens of copper and aluminium by electron diffraction.
Vacuum,vol.26(1976), P: 433-436.

16. W.A.A.Al-Bermani, Proportional analysis of composite polycrystalline specimens by electron diffraction.
Ph.D. Thesis (1980), Aston University.

17. J.S.Halliday, The contrast, breadths and relative intensities of electron diffraction rings.
Proc. Roy. Soc., vol.A254(1960), P: 30-47.

18. S.G.Ellis, Plural electron scattering and its influence on electron diffraction patterns.
Phys. Rev., vol.87(1952), P: 970-976.

19. T.B.Rymer, Electron Diffraction.
Methuen and Co., London, 1970.

20. J.Karle and I.L.Karle, Internal motion and molecular structure studies by electron diffraction.
Jour. Chem. Phys., vol.18(1950), P: 957-962.

21. S.Tolansky, Multiple Beam Interferometry of Surface and Films.
Clarendon Press, Oxford 1948.

22. F.Lenz, Zur streuung mittelschneller elektronen in kleinste winkel. Z.Naturf., vol.9a(1954), P: 185-204.

23. N.R.Mukherjee and O.Row, Studies of thin films by electron diffraction. J.Appl. Phys., vol.22(1951), P: 681-682.

24. P.B.Hirsch Electron Microscopy of Thin Crystals. Butterworths, London 1965.

25. G.Thomas, Transmission Electron Microscopy of Metals. John Wiley and Sons, London 1962.

26. International Tables for x-ray Crystallography, Table 5.2.2B. The Kynoch Press, Birmingham 1974.

27. A.Guinier, X-ray Diffraction. W.H.Freeman and Company, San Francisco and London, 1963.

28. R.Al-Mausawe and T.F.J.Quinn, The effect of amorphous material on the contrast of electron diffraction patterns. J.Phys. D. : Appl. Phys., vol.15(1982) P: 267-274.

29. J.A.Ibers, Atomic scattering amplitudes for electrons. Acta. Cryst., vol.11(1958), P: 178-183.